Jochen Matthias Rau

# Dual Frequency Band Ultrasound for Suppression of Multiple Scattering

Thesis for the degree of Philosophiae Doctor

Trondheim, May 2013

Norwegian University of Science and Technology
Faculty of Medicine
Department of Circulation and Medical Imaging

**NTNU – Trondheim**
Norwegian University of
Science and Technology

**NTNU**
Norwegian University of Science and Technology

Thesis for the degree of Philosophiae Doctor

Faculty of Medicine
Department of Circulation and Medical Imaging



ISBN 978-82-471-4313-1 (printed ver.)
ISBN 978-82-471-4314-8 (electronic ver.)
ISSN 1503-8181

Doctoral theses at NTNU, 2013:107

Printed by NTNU-trykk

## Reverberasjonsundertrykkelse med tofrekvens ultralyd

Medisinsk ultralyd er hyppig brukt i alle medisinske fagretninger. Ultralyd har en rekke fordeler: Sanntidsavbildning, høy oppløsning, høy bilderate, lave kostnader, mobilitet og sikkerhet. Til tross for alle fordeler, finnes det pasienter som er vanskelige å avbilde, noe som resulterer i dårlig fremstilte strukturer og artefakter i ultralydbilder. Denne avhandlingen søker å gi en bedre forståelse av en klasse artefakter som kalles reverberasjoner, og hvordan disse kan undertrykkes.

Reverberasjoner er artefakter som oppstår når ultralydpulsen blir reflektert mer enn én gang på dens vei fra lydhodet gjennom vevet og tilbake til lydhodet. Reverberasjoner kan bli synlige som forskjøvede kopier av strukturer, eller som mer eller mindre tett tåke som legger seg over bildet og som skjuler underliggende strukturer.

I reverberasjonsunderstrykkelse med tofrekvens ultralyd blir det utnyttet at lydhastigheten er trykkavhengig. For å gjøre dette blir lydhastigheten til avbildningspulsen påvirket av en annen lydpuls, manipulasjonspulsen. Manipulasjonspulsen og avbildningspulsen beveger seg sammen gjennom vevet som et såkalt pulskompleks. For hver linje av bildet må to slike pulskomplekser sendes etter hverandre. Først en hvor avbildningspulsen ligger på et trykkmaksimum av en manipulasjonsbølge og så en på et trykkminimum. Lydhastighetsforskjellen mellom de to pulsene gjør at en tidsdifferanse bygges opp. Etter den første refleksjonen i vevet faller manipulasjonstrykket ganske drastisk slik at den ikke lenger manipulerer avbildningspulsen og tidsdifferansen forandres ikke lenger. Slik bærer avbildningspulsen informasjon om den dybden den ble først reflektert i. Dette kan brukes i signalbehandlingen.

Simuleringer og eksperimenter ble gjennomført for å forstå reverberasjoner bedre. Signalmodeller og metoder for reverberasjonsundertrykkelse ble utviklet. To forskjellige fremgangsmåter blir presentert. Den første opphever reverberasjoner men krever at signalene ikke er særlig forvrengte. I den andre regner man ut hvor det er støy og hvor det ikke er støy i bildet. Bildet vektes med dette estimatet slik at områdene med støy blir dempet. Den andre metoden er ikke like nøyaktig, men gir høyere reverberasjonsundertrykkelse. Det finnes ikke kommersielle ultralydapparater som støtter tofrekvens ultralyd. Det ble derfor bygget utstyr og laget programvare slik at man kunne sette sammen en slik ultralydskanner. Denne skanneren ble brukt både i laboratorieforsøk og i en klinisk studie for å sammenligne tofrekvens støyundertrykkelse med dagens metodikk. Kontrast i bildene blir brukt som mål for bildekvaliteten og ytelsen til metoden. Kontrasten økte markant i både simulerte data og pasientdata.

Jochen Matthias Rau, Institutt for sirkulasjon og bildediagnostikk (ISB), NTNU
Hovedveileder: Prof. Bjørn A.J. Angelsen, (ISB, NTNU)
Biveileder: Rune Hansen, PhD (SINTEF, ISB, NTNU)
Finansieringskilde: Norges teknisk-naturvitenskapelige universitet
*Ovennevnte avhandling er funnet verdig til å forsvares offentlig for graden philosophiae doctor (PhD) i medisinsk teknologi. Disputas finner sted i Auditoriet, Medisinsk Teknisk Forskningssenter, tirsdag 14. mai kl 12:15.*

# Abstract

Diagnostic medical ultrasound is a widely used imaging modality in nearly all disciplines of medicine. It combines a lot of valuable features: real-time anatomical images, high resolution, high frame rate, low cost, mobility and safety. Despite all advantages, there are 'difficult' patients, there are poorly visualized structures, and there are artifacts in ultrasound images. The work of this thesis is devoted to understanding and suppression of one class of artifacts – reverberations.

Reverberations occur if the ultrasound pulse is scattered or reflected more than once on its way from the transducer through the tissue and back to the transducer. Reverberation artifacts in an image can appear as discrete replica of tissue structures or as haze of various density which conceals structures.

Dual frequency band imaging (DBI) is a technique where the pressure dependent sound propagation velocity is utilized for reverberation suppression. The propagation velocity of an imaging pulse is modified by a low frequency manipulation pulse. Two transmits are necessary for each line in the image. One with the imaging pulse on a pressure peak and the other with the imaging pulse on a pressure trough of the manipulation pulse. Due to the manipulated propagation velocity a delay between the two imaging pulses accumulates with depth. After the first scattering of the pulse complex, the manipulation pressure decreases to levels which can be considered not to manipulate any further. The imaging pulse thus carries information about the depth of first scattering, which then can be utilized in signal processing.

Simulations and experiments were conducted to better understand reverberations. Signal models and methods for reverberations and their suppression have been developed. Two different approaches are presented in this thesis. The first approach cancels reverberations, but requires low nonlinear pulse form distortion. The other weights the image with an estimate of the spatially local first order signal content in the received signal. This is not as precise as the first approach, but yields stronger suppression. Since no commercial scanner currently features DBI a scanner had to be built. A research scanner was purchased and extended and modified in hardware and software. With this scanner it was possible to acquire data both in laboratory settings and in a clinical study.

Image contrast is utilized as a measure for image quality. A marked increase in image contrast through reverberation suppression could be demonstrated for simulated as well as *in vivo* data.

# Preface

This thesis has been submitted in partial fulfillment of the requirements for the degree Philosophiae Doctor (PhD) at the Faculty of Medicine of the Norwegian University of Science and Technology (NTNU). The research was funded by the NTNU. It was carried out under the supervision of Professor Bjørn Angelsen at the Department of Circulation and Medical Imaging, NTNU and co-supervised by Rune Hansen, PhD, at SINTEF and at the Department of Circulation and Medical Imaging, NTNU.

**Acknowledgements**

The way towards this thesis was a winding road, and I am grateful for all guidance, company and support. First, I want to express my gratitude to my supervisor Prof. Bjørn Angelsen for his guidance. In these years, I got to know him as a brilliant and highly motivated researcher with countless ideas. Second, my gratitude goes to my second supervisor, Dr. Rune Hansen, for his support and deliberate directions.

The SURF research group was important to my work – various backgrounds, different levels of experience and many perspectives made a really good team. Just to mention some aspects: Thank you, Svein-Erik for your openness, endless enthusiasm and motivation, Tonni for knowing and sharing everything I wondered about acoustics and the lab, Thor Andreas for brilliant programming and staying focused on the essential, Øyvind for thoroughness and several chats about tools, Halvard for the simulation code and Norwegian lectures-of-the-day and Peter for good explanations, discussions and patience. It was a pleasure to work with you all!

Furthermore, I want to thank the rest of my current and former colleagues at the department including our helpful administration for a positive working atmosphere. A special thanks to the other PhD candidates for sharing experience, entertaining breaks and a smoothie from time to time. Thank you to Martijn, Ingvild and my co-authors for proof reading the different parts of my thesis. During my work, I enjoyed excellent collaboration with Magnus Andersen and the other engineers at Norbit AS and Kris Dickie and Chris Cheung at Ultrasonix. I also want to express my gratitude to the GE VingMed engineers for sharing their scanners and knowledge.

Finally, I am deeply grateful for my friends' and family's support, encouragement and interest in my work. Thank you, Jonas, for giving me the best motivation to complete the thesis, and my dear Berit, for all your love, patience, understanding and believing in me, especially when times were tough.

# Contents

# Introduction

Jochen Matthias Rau
Department of Circulation and Medical Imaging, NTNU

ultra-sonorous
*ultra-, prefix* [ʌltrə]
*With adjs., signifying "going beyond, surpassing, or transcending the limits of" (the specified concept)*
*sonorous, adj.* [səˈnɔərəs]
*Giving out, or capable of giving out, a sound, esp. of a deep or ringing character* *(Oxford English Dictionary)*

"Ultra-sonorous mechanical oscillations" was the term Chilowsky and Langevin used to describe what today is termed "ultrasound" in their patent application in 1917 on the production of submarine signals and the location of submarine objects [1]. Both terms describe longitudinal compression waves with frequencies beyond the human audible range. Chilowsky's and Langevin's efforts are considered the first successful (human) application of ultrasound which utilized the known speed of sound in the propagation medium to estimate the distance to a reflecting object. Key to the success was their introduction of piezo-electric materials in their transmitter and receiver – a technology which still today is very common for exciting and receiving ultrasonic waves.

In the decades following the first invention, ultrasound was utilized in a growing number of applications, *f.ex.,* flaw detection in materials or heating and ablating of tissue. The diagnostic use of ultrasound in medicine started in the 1940s and has steadily grown since. First using metal flaw detectors, later applying machines exclusively built for the medical purpose. The imaging technique also developed from first displaying single lines to later combining the lines to form two dimensional images, visualizing blood flow and presenting detailed images in grayscale in real time [2].

Currently, 3D imaging is available as well as hand-held ultrasound scanners, and increasing computing power allows for more sophisticated signal processing methods. Ultrasound is widely used in medical diagnosis: Ultrasound screening of pregnant women and their unborn children is common practice in many countries and may

be the most prominent application. Nevertheless, ultrasound is present in nearly all disciplines of medicine, amongst others cardiology, radiology, anaesthesiology, gastroenterology, emergency medicine and urology.

Ultrasound has been successful within all those disciplines since it is non-invasive, yields real-time images, can be used to monitor movement, does not utilize ionizing radiation (as X-ray imaging) and is, as long as safety limits are respected, safe. Furthermore, it is considered inexpensive compared to modalities such as X-ray computed tomography or magnetic resonance imaging, and transportable, as most of the ultrasound scanners feature wheels or can even be carried around.

Inevitably, medical ultrasound also has challenges and disadvantages. First of all, ultrasound works well only on soft tissues. Imaging (through) bone, or penetrating gas filled cavities is hardly possible. The penetration depth is limited and frequency dependent and there is a trade-off between frame rate, imaging depth and spatial resolution. Finally, image quality is also dependent on the imaging system, the subject, and the geometry being imaged, and may further be impaired by artifacts and noise which occur if the fundamental approximations and assumptions, which ultrasound imaging is built on, are violated [3].

## 1.1 Motivation and aims of study

The overall aim of this thesis is to improve image quality of ultrasound images to enable more reliable and faster diagnosis or even enable diagnosis where it has not been possible yet. Image quality is one of the most important factors, independent of what ultrasound is utilized for, as *f.ex.,* anatomical inspection, guiding, measuring distances or monitoring structures in motion. Very important aspects of image quality is spatial resolution and contrast resolution. Spatial resolution defines the distance two objects need to have to still be discerned as two objects. Contrast resolution defines the brightness (in ultrasound the echogenicity) difference two objects need to have to still be discerned from each other after being imaged. In this thesis improvement of the contrast resolution is addressed.

Stroke is a major cause of death in the world [4] and, if not deadly, also can lead to disabilities and make long-lasting treatment and assistance necessary. Atherosclerosis, a risk factor for stroke, is a disease which is slowly developing over time. Through the years, plaques form at artery walls. These plaques may rupture and parts of them are washed away with the blood. The fragments may then occlude smaller blood vessels along their way. Stroke is caused if the occluded vessel is located in the brain. The composition of these plaques (lipidic, fibrotic or calcified), the stage of development and its shape are factors to determine the risk of rupture [5, 6].

Atherosclerosis in the carotid artery is today mainly assessed with ultrasound. The carotid artery Intima-Media-thickness (C-IMT), the thickness between the intima and the media layer of the artery wall, is a marker of early atherosclerosis and amongst others associated with the risk of new or recurrent stroke [7]. C-IMT is commonly measured on fundamental B-mode images. In these images, the media is most prominent with a strong echo while the intima results in a weaker echo. Image quality is

strongly patient dependent and varying. C-IMT is often measured on the distal wall of the carotid artery – the region behind the front wall is often concealed in a dense haze of multiple reflection artifacts, also called reverberations.

The main goal of this work is to improve image quality by reducing such artifacts utilizing a dual frequency band imaging technique. This technique is and has been developed at the Department of Circulation and Medical Imaging, NTNU, under the name SURF Imaging. Sub-goals are: 1. The acoustic analysis of and development of signal models for reverberations in medical ultrasound. 2. Development of reverberation suppression algorithms for DBI. 3. Hard- and software development to enable *in vivo* testing of these methods. 4. *In vivo* evaluation of the methods.

Before the thesis is summed up with an overview of the contributed articles and an overall discussion, in the following sections, some of the theory behind conventional ultrasound imaging, the applied approximations and occurring artifacts will be introduced. In addition, nonlinear propagation and dual frequency band imaging (DBI) will be presented.

## 1.2 Conventional ultrasound imaging

In medical ultrasound imaging short imaging pulses are transmitted into the tissue. In acoustics, transmission and reception of sound waves is usually carried out using separate devices, *i.e.,* a microphone and a loudspeaker. In contrast to that, it is most common in ultrasound imaging that transmission and reception is carried out with the same device, the transducer. Nowadays, most of the transducers consist of an array of small elements made of piezo-ceramics arranged in regular patterns, *f.ex.,* a line. If an electric field is applied to one of the elements, the piezo-ceramic will deform, and in turn result in an increase or decrease in height depending on the direction of the field. This converts electrical energy into vibration and a compression wave is generated. With an array transducer it is also possible to electronically steer and focus the sound wave if the transmit signal is delayed accordingly.

Typical imaging pulse frequencies range between 2 and 12 MHz with a pulse length between 1.5 and 2.5 periods. When the travelling pulse hits interfaces between different tissue types (*f.ex.,* fat, muscle, connective tissue) or heterogeneities within these tissues it is (partially) reflected or scattered, and thus an echo is created. The echo propagating back to the transducer and excites the elements, which in turn generates a voltage. The voltage is then amplified, digitized, and processed.

The time $t$ between the transmission and the reception is measured. Together with the sound velocity in the tissue $c$ the depth $z$ can be computed:

$$z = \frac{ct}{2}\,. \tag{1.1}$$

For each element and transmit a vector of samples is recorded. By applying suitable delays as on transmit and sum the element signals the receive sound field can be focused and steered (see *f.ex.,* [8]), a process called beamforming.

To form a two dimensional image, a number of lines is subsequently recorded, usually with a small lateral translation or rotation of the different lines relative to the

transducer footprint. The amplitude of the envelope of the received and beamformed signal is converted to a grayscale value and the lines are displayed on a screen according to their orientation.

So far, several assumptions were implicitly made. Four of them will further be discussed: First, sound waves are reflected or scattered only one time before they are received at the transducer. Second, Eq. (1.1) assumes a constant sound propagation velocity. Third, the information gathered and extracted from the three dimensional sound field is represented as one straight thin line. Fourth, the sound wave is not attenuated on its propagation path.

In more detail, starting with the assumption of propagation without attenuation: Propagation of sound is nearly free from attenuation in water. However, in tissue, acoustic pulses experience frequency dependent attenuation in the order of 0.5 dB/ MHz per centimetre propagation length. As a consequence, the longer (and thus deeper) an ultrasound pulse has propagated the weaker it gets. In addition, its center frequency is lowered as attenuation is stronger for higher frequencies in the frequency band than for lower ones. While constant attenuation can partly be compensated for, attenuation is also tissue dependent, and will vary within the insonified region of interest if it is heterogeneous. This leads to tail artefacts – dark tails if the attenuation is stronger than expected or bright tails if it is less.

Beamforming combines the recorded channel data to an image line. Since the image pulse has a spatial extent which is wider than the line which is displayed in the image, reflections from objects off the beam axis will be incorporated in the final signal. This will be especially pronounced if the objects are located in the side lobes, areas within the beam outside of the main lobe, which occur if a limited transducer aperture is used. This effect can be reduced if the transmit amplitude or receive amplification is reduced ('apodized') towards the edges of the aperture [9]. Side lobe artifacts become visible if a hypoechoic region, *f.ex.,* the bladder, is imaged and echogenic objects are located off axis. In this case, there will be noise in the hypoechoic region, mostly haze like, impairing the contrast. Even though it will be hard to spot in a normal imaging situation, the noise still is there and will reduce contrast resolution.

The validity of the assumption of constant speed of sound is also dependent on the homogeneity of the medium. The speed of sound for a longitudinal wave is for small amplitudes given as:

$$c_0 = \frac{1}{\sqrt{\kappa \rho_0}} \tag{1.2}$$

With $\kappa$ being the adiabatic compressibility, $\rho$ mass density, and the subscript 0 indicating quasi-equilibrium conditions [8]. The requirement on small amplitudes is important as it excludes nonlinear propagation which would introduce a pressure dependency on the speed of sound. This will be discussed in further detail in Sec. 1.3. For most tissue types $c_0$ ranges from 1350 to 1700 m/s [10]. Different tissue types in a heterogeneous medium cause a deformation of the lateral spatial wave form and thus destroy the focusing of the beam. This kind of artifact is called aberration and affects the spatial resolution.

Echoes are caused by heterogeneities in the medium, more precisely, by differences in the characteristic acoustic impedance at borders between two objects. The

characteristic acoustic impedance is defined as:

$$Z_0 = \rho_0 c_0 = \sqrt{\frac{\rho_0}{\kappa}} \tag{1.3}$$

The commonly named Born Approximation says that scattering is weak. This means that the wave propagates nearly unchanged through the scattering medium and that multiple scattering can be neglected [8]. However, a number of interfaces within a medical ultrasound imaging situation may violate this assumption, with the tissue-transducer interface being a stronger reflector than most of the other interfaces such as fat-muscle or muscle-blood. As a consequence in many cases, multiple scattering and multiple reflections cannot be neglected and occur as reverberation artifacts. Reverberations overlap with the first order signal with the same propagation path length. Depending on the mediums' geometry they may occur as clear replica of structures or as haze like noise. In any case, reverberations impair the contrast resolution of the ultrasound image and potentially cover hypoechoic structures. This thesis focuses on reverberations and how they may be suppressed with DBI.

## 1.3 Nonlinear propagation and nonlinear ultrasound imaging

The definition of the speed of sound in Eq. (1.2) was made under the assumption of a small signal amplitude. For higher amplitudes the sound propagation velocity is also pressure dependent. The nonlinear speed of sound can be approximated as [11]:

$$c \approx c_0(1 + \beta_n \kappa p) \tag{1.4}$$

In this equation, $\beta_n$ is a nonlinearity material parameter and $p$ the pressure.

As a consequence, pressure crests will propagate faster than pressure troughs. An ultrasound pulse will thus increasingly be distorted during propagation in a nonlinear material, *i.e.,* tissue. In the frequency domain, this distortion can be observed as harmonics to the fundamental frequency band which rise with propagation depth. Attenuation will work against this accumulation as higher frequencies experience stronger attenuation.

Nonlinear propagation is utilized in medical ultrasound in tissue harmonic imaging (THI). Utilizing a single transmit pulse, THI is implemented as follows: A pulse is transmitted with a certain center frequency $f_c$. On receive, the signal is filtered in the second harmonic band around $2f_c$ [12–14]. The two-pulse approach is called "pulse inversion" (PI). In PI, the first pulse and then its inverse are transmitted. The two acquired signals are then summed. In the summation the linear component is cancelled and the even harmonic components remain [15, 16].

THI is used as a technique to suppress reverberation noise. For focused transmit beams, the pressure close to the transducer is low. In addition, nonlinear distortion is an accumulative effect which needs some propagation distance to build up. Reverberations with the first reverberator close to the transducer will thus have a limited content

of harmonics. Also here, weak scattering is assumed, resulting in an amplitude after reflection which is too low to generate further nonlinear effects. As a consequence, if the fundamental component is filtered out, also these reverberations are be attenuated. Reverberations with a deep first reverberator will not be attenuated as strongly.

## 1.4 Dual Frequency Band Imaging

Dual frequency band imaging utilizes two separated frequency bands. The application which is investigated in this thesis is developed at the Department of Circulation and Medical Imaging, NTNU, and also termed SURF imaging. If not mentioned otherwise, DBI and SURF imaging will be used as synonyms.

DBI utilizes pulse complexes consisting of a low frequency (LF) manipulation pulse and a high frequency (HF) imaging pulse. While the pulses are clearly separated in the frequency domain with a center frequency ratio of 1:7 to 1:10, they are transmitted overlapping both in space and time. The LF pulse manipulates the propagation and scattering of the HF pulse. The manipulation is strongly dependent on the position of the imaging pulse relative to the manipulation pulse. DBI pulse complexes are illustrated in Fig. 1.1a which is taken from Paper C.

Placed on a crest (or in a trough), the propagation velocity is altered as described by Eq. (1.4) and a propagation delay is accumulated with depth (see Fig. 1.1b). However, the HF pulse has an extent in time and with a center frequency $f_{c_{HF}} = 10 f_{c_{LF}}$ it will cover a tenth to a fifth of a LF wavelength. As a consequence, the head and tail of the imaging pulse will travel somewhat slower (in a trough: faster) than the center. This leads to nonlinear pulse form distortion.

Placed on a gradient, the imaging pulse will be shortened or elongated, since the tail is travelling slower than the head, or vice versa. This yields a frequency shift.

The relative position of the two pulses is also not constant. In a focused beam, the pulse will experience a 90 degree phase shift towards focus. This might be of minor importance for the imaging pulse, but if the LF pulse is focused, the imaging pulse will slide from the gradient to the crest or vice versa on its way towards the focus. In addition, diffraction is different for the two pulses forming the pulse complex.

In this thesis, if not specified otherwise, an unfocused manipulation pulse and a focused imaging pulse is used. This configuration introduces nonlinear aberration as the center part of the imaging pulse travels on a different manipulation phase compared to the outer parts.

As shown in the previous paragraphs, the manipulation pulse introduces also a number of new sources of pulse form distortion and manipulation which might or might not be desired. A thorough discussion of these effects can be found in [17].

At the beginning, DBI was investigated as technique for enhanced imaging of ultrasound contrast agents, which are gas filled microbubbles [18–20]. The bubbles will respond in a different way on the manipulation pressure than tissue. Using two different manipulations and evaluating the differences between these two transmits will enhance the contrast agent signal and attenuate the tissue signal.

Like propagation, also scattering has nonlinear dependencies. This has been as-

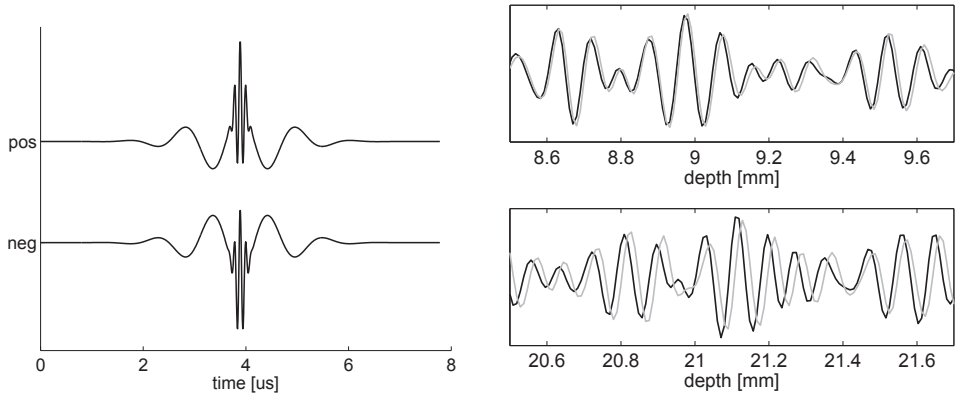


(a) DBI pulse complexes. Upper pulse positive manipulation, lower pulse negative manipulation.

(b) Positively (black) and negatively (gray) manipulated imaging signal around 9 and 21 mm depth. Note the delay increase.

Figure 1.1: From paper C:(a) DBI pulse complexes consisting of a low frequency manipulation pulse and a high frequency imaging pulse. In this example $f_{HF} : f_{LF} = 10 : 1$ (b) DBI RF signals for a shallow and a deep location.

sessed utilizing DBI for imaging of micro calcium particles in simulations and *in vitro* experiments [17].

In this thesis, DBI reverberation suppression is investigated. This is a continuation of the work of Näsholm *et al.* who proposed subtraction of inversly manipulated imaging signals [21] and a post-processing method with delay corrected subtraction with a fixed correction delay [22].

## 1.5 Summary of thesis

As an introduction to the summaries of the four papers which make up this thesis, they are put into the context of work being carried out at the Department of Circulation and Medical Imaging during that time.

At the beginning of this work, a small scale prototype dual frequency array transducer had been built and the manufacturing of two full scale probes, one targeted to carotid artery imaging, one targeted for shallow abdominal use, was in progress. In the mean time, the research group gathered experience on dual frequency acoustics with a newly built dual frequency annular array where the manipulation and the imaging array share the same acoustic radiation surface [23].

At that time, imaging was restricted to annular arrays which were operated by a modified GE System V scanner with offline postprocessing of the acquired data. An Ultrasonix SonixRP research scanner was purchased in 2008. It was extended with hard and software to operate the dual frequency arrays and yield images in real-time. It was tested together with the full scale linear arrays. It was discovered that the scanner

transfer function had to be improved and that the carotid prototype probe had to be redesigned due to malfunctioning elements and advances on DBI beamforming. All work on the scanner is documented in Paper A.

Early 2010 the scanner reached a working stable state. The most reliable probe available was the first abdominal prototype. A planned and already postponed clinical trial assessing the performance of DBI for carotid artery imaging was started with this setup. Parallel to the trial, work on algorithms came into focus. While the trial was ongoing, a new linear array probe arrived with 8 and 0.9 MHz on the high and low frequency array, respectively. It was more suited to the purpose and performed better, and it was decided to include it into the study. The study was completed at the end of the same year and is described in Paper D.

While algorithm development continued, Halvard Høilund-Kaupang concluded on his thesis, which resulted both in a presentation on the utilized reverberation model and in a simulation tool [24]. This simulation tool is able to simulate not only transmission and forward propagation but also reflections and multiple reflections. Reverberation simulation and experimental validation was conducted and is documented in Paper B.

Finally, the developed reverberation suppression methods were documented with simulations and experimental examples in Paper C.

The following subsections present a short summary for each contributed paper.

## Paper A: An Ultrasound Research Scanner for Dual Frequency Band Imaging

The first paper describes the necessary modifications to turn an Ultrasonix SonixRP research scanner into an ultrasound scanner for dual frequency band imaging on array transducers. It supports real-time operation, storage of beamformed radio-frequency (RF) data and script-based operation for laboratory experiments. DBI requires that the scanner features at least two independent power supplies, two transmitters, synchronization electronics and additional software. An additional improvement of the receive electronics of the SonixRP system resulted in a sensitivity increase of up to 10 dB.

Besides the modifications, experiments are presented which document the performance and functionality of the system. Strengths and limitations of the scanner are discussed.

*The work was a joint effort with the research group, in particular Thor Andreas Tangen, who implemented most of the real-time software. The scripting interface was implemented by the candidate. The hardware extension was designed and built together with Norbit AS, a local electronics company. The scanner modifications were investigated by the candidate and carried out by a university electrical workshop and the candidate. The experiments and all writing were conducted by the candidate.*

## Paper B: 2D Reverberation Simulation and Experimental Validation

In the second paper reverberations are investigated. Together with the candidate, second author of this paper, Halvard Høilund Kaupang, proposed in his thesis a reverberation classification scheme for third order reverberations with the transducer as second reverberator. This scheme states that reverberations always act in pairs which, after beamforming, will deviate if they propagated nonlinearily. This could be validated in an *in vitro* model consisting of a planar reflector and a point scatterer, both in simulation and water tank experiment. In addition, it could be shown that with a change in aperture or utilizing channel data, the components of the pairs can be separately detected. For precise reverberation simulation, the inner structure of the transducer is not neglegible as it has influence on the timing of the reverberations.

*The work was a joint effort with Halvard Høilund-Kaupang, who implemented the simulation code used in the paper. The candidate set up and carried out simulations, experiments and most of the writing.*

*This paper is being prepared for submission to the Journal of the Acoustical Society of America*

## Paper C: Reverberation Suppression Utilizing Dual Frequency Band Imaging

The third paper presents two methods for reverberation suppression with DBI: The Delay Corrected Subtraction (DCS) method and the First Order Content Weighting (FOCW) method. The subtraction method (SUB), which was published earlier [21], is included in the evaluation for comparison. The SUB method suppresses one component of the reverberation pair well. However, attenuation of the component with the first reverberator close to the target is low as for THI.

The DCS method is a generalization and evolution of an earlier presented post-processing method to the SUB method [22]. The imaging signals are corrected for a certain delay before subtraction. New in the DCS approach is to apply a delay correction which varies with depth. From theory, DCS cancels both components of the reverberation pair, but requires low pulse form distortion and equal transmit and receive beams.

FOCW is a novel method which utilizes the delay information to compute a local estimate of the first order echo content in the total received signal. The image is then weighted with this estimate.

The methods are applied to both, two *in vivo* images, and three simulated lines with two different receive beam settings (dynamic vs. fixed focus). Both methods show both visual and measurable improvement. DCS maintains more details than FOCW, while FOCW yields higher contrast increase. The quantitative measurements on the simulation data show a contrast increase from 4 to 80 dB dependent on the situation and the method.

*DCS was an effort of the whole research group. The initial formulation of the*

*FOCW method is attributed to Thor Andreas Tangen. The candidates contribution comprise the recognition of FOCW as a weighting method, FOCW development, its relation to SNR, first order estimation techniques for* in vivo *data, conducting simulations, applying methods to the example data and writing.*

*This paper is being prepared for submission to the Journal of the Acoustical Society of America*

### Paper D: Image Contrast in Carotid Artery Images for Fundamental, Harmonic and Dual Band Imaging

The last paper compares the performance of an early version of the DBI FOCW with state of the art THI in a clinical setting. In 22 patients recruited from the vascular day clinic, carotid artery images were acquired with both modalities after conventional diagnosis. An image contrast analysis is conducted comparing the mean signal in the artery lumen with the signal in its distal wall. The contrast increase compared to fundamental imaging at the same position is used as a measure for the reverberation suppression performance.

The DBI scanner was utilized for data acquisition of the FOCW data. For THI, GE Vivid systems were utilized. Even though the GE systems clearly outperform the DBI scanner, the baseline fundamental image contrast is not significantly different.

Both methods show statistically significant contrast increase, THI 3.5 dB and DBI 15 dB.

*The study was an effort of all authors. The candidates contribution comprises scanner operation, analysis software development, statistical analysis and parts of writing.*

*This paper is being prepared for submission to Ultrasonics*

## Discussion

The extension of a commercial research scanner with additional hardware and software is challenging and a lot of engineering work had to be invested to make the platform work and stable enough to fulfil its purpose in the lab and in the clinics. At the same time, DBI is a challenging technology for a scanner. On the one hand it complicates the software since one has to control two transmit front ends, ensure synchronous operation and rewrite routines which no longer fit the new signal processing scheme. On the other hand, DBI is challenging for the hardware as well. Especially the reflected low frequency manipulation wave has to be dealt with. Preferred here is an analog filter before A/D conversion, otherwise precious dynamic range is wasted. However, implementing that requires hardware modifications behind the transmit-receive switch. In addition, the filter should probably be programmable if a variety of imaging frequencies is considered. Another aspect of the approach of an external hardware extension is that cables connecting the different parts might be sensitive for electromagnetic noise.

Paper B validates both the reverberation model and the simulation tool which was used for simulation. While the existence of reverberation pairs is quite straight

forward, it is interesting to study their different properties with respect to being imaged with an array. To assume the transducer is a reflecting plane proved to be an assumption which is not true for reverberation simulations. This might not be of great importance for simulations of complex geometry but is a reminder to always consider the whole system and choose approximations with care.

Two novel reverberation suppression methods are presented and their approach to reduce reverberation impact is fundamentally different. While one method removes reverberations, the other estimates the signal content and uses this local estimate to weight the original image. Both methods build on the same theoretical base, but they still depend on several approximations and assumptions. From theory, both methods maintain all first order signal or at least the first order signal level. For the FOCW method, the length of the estimation window limits the spatial resolution of the delay estimate which might lead to undesired suppression of details. The initial evaluation yields a marked contrast increase for both methods.

On 22 patients, a statistically significant reverberation suppression with DBI was demonstrated. The image contrast increase on a mediocre imaging system with a prototype probe was well above the contrast increase on a high-end system with THI. The clinical study might be challenged for its use of different equipment. However, few hardware vendors open their system that modifications of this dimension are possible. Besides that, even with one system, it would not have been possible to use one transducer due to the limited bandwidth of the imaging array of the dual frequency transducers. In all cases, the change of equipment was carefully considered not to invalidate the significance of the study. Independent of that, the study is a first approach to quantify contrast increase *in vivo* which has not been published earlier.

## Conclusion

This work shows feasibility and initial evaluation of reverberation suppression with dual frequency band imaging in simulations, *in vitro* and *in vivo*. Two methods are presented, thereof one clinically evaluated. The methods were developed on a basis of a theoretical signal and reverberation model which could be confirmed in simulation and experiment. The clinical evaluation yields promising image contrast and thus image quality improvement which is superior to current methods in the application of carotid artery imaging.

## Suggestion for further work

Independent benchmarks for image quality improvement are lacking in ultrasound imaging. A set of simulation scenarios, *in vitro* phantoms or a database with acquired RF data with known outcome for fundamental imaging which could be processed also by other research groups should be considered to make comparison and research more objective.

Implementation of DBI on a high-end scanner with suited probes is a natural step. Alternatively, also deeper integration of the system will lead to improvement. For method development, the resulting delay in different imaging situations, the necessary

strength of a scatterer to alter a delay estimate, and delay estimation itself are topics for further research. Delay estimation from channel data prior to beamforming could be a promising approach considering the results in Paper B.

Regarding clinical validation, the increase in clinical value should be evaluated: How is DBI reverberation suppression perceived and does it enable or improve diagnosis? Entering other disciplines and evaluating other applications should be considered, as well.

## 1.6 Further contributions

What follows is a list of contributions of the candidate which are not part of this thesis.

**Peer reviewed papers**

1. S.-E. Måsøy, T.A. Tangen, Ø. Standal, **J.M. Deibele**, S.P. Näsholm, R. Hansen, B.A.J. Angelsen, and T.F. Johansen, "Nonlinear propagation acoustics of dual-frequency wide-band excitation pulses in a focused ultrasound system", *J Acoust Soc Am*, vol. 128, no. 5, 2010

**Conference proceedings**

1. T. Rommetveit, T.F. Johansen, **J.M. Deibele**, H. Kaupang, B.A.J. Angelsen: "Two-Way Nonlinear Manipulation in Plane Materials using Dual Frequency Pulse Complexes", Proc IEEE Ultrason Symp, pp. 2380-2383.

2. T.F. Johansen, **J.M. Deibele**, S.-E. Måsøy, *et al.*: "Design and Test of a Dual-Layer, Dual-Frequency SURF Array", Proc. of 31st Scandinavian Symposium on Physical Acoustics, 2008-01

**Talks and Presentations**

1. **J.M. Deibele**, S.-E. Måsøy, T. Dahl, T.A. Tangen, R. Hansen, T.F. Johansen, Ø. Standal, B.A.J. Angelsen: "Clutter reduction — a quantitative in vivo image contrast analysis", BMT, 2011-09

2. **J.M. Deibele**, S.-E. Måsøy, T. Dahl, T.A. Tangen, R. Hansen, T.F. Johansen, Ø. Standal, B.A.J. Angelsen: "Bedret avbildning av carotis med SURF imaging", NFUD Symposium, 2011-03

3. **J.M. Deibele**, T.A. Tangen, S.-E. Måsøy, R. Hansen, T.F. Johansen, B.A.J. Angelsen: "Undertrykkelse av reverberasjoner med SURF-imaging", NFUD Symposium 2010-04

4. S.-E. Måsøy, **J.M. Deibele**, T.A. Tangen, H. Kaupang, R. Hansen, T.F. Johansen, B.A.J. Angelsen, A. Angelsen, T. Dahl, P. Østhus, K. Helset: "SURF imaging – kliniske eksempler", NFUD Symposium, 2010-04

5. **J.M. Deibele**, T.A. Tangen, S.-E. Måsøy, R. Hansen, Ø. Standal, T.F. Johansen, B.A.J. Angelsen: "Hvordan få en scanner til å SURFe", NFUD Symposium, 2009-04

6. **J.M. Deibele**, J. Kocbach, P. Lunde, *et al.*: "Transdusere for SURF avbildning", NFUD Symposium, 2008-04

### Awards

1. GE Best Presentation Award at Symposium of the Norwegian Society of Ultrasound Diagnostics (04/2010)

2. Ultrasonix Student Award for contribution to Ultrasonix research community (12/2010)

## Bibliography

[1] C. Chilowsky and P. Langevin, "Production of submarine signals and the location of submarine objects," U.S. Patent 1 471 547, Oct., 1923.

[2] M. McNay and J. Fleming, "Forty years of obstetric ultrasound 1957-1997: From a-scope to three dimensions," *Ultrasound Med Biol*, vol. 25, no. 1, pp. 3–56, Jan. 1999.

[3] M. K. Feldman, S. Katyal, and M. S. Blackwood, "US artifacts," *Radiographics*, vol. 29, no. 4, pp. 1179–1189, Jul. 2009.

[4] WHO, "Fact sheet 310, the top ten causes of death 2008," May 2011.

[5] E. Falk, "Why do plaques rupture?" *Circulation*, vol. 86, no. 6 Suppl, pp. III30–42, Dec. 1992, PMID: 1424049.

[6] E. Falk, P. K. Shah, and V. Fuster, "Coronary plaque disruption," *Circulation*, vol. 92, no. 3, pp. 657 –671, 1995.

[7] P. Prati, A. Tosetto, D. Vanuzzo, G. Bader, M. Casaroli, L. Canciani, S. Castellani, and P.-J. Touboul, "Carotid intima media thickness and plaques can predict the occurrence of ischemic cerebrovascular events," *Stroke*, vol. 39, no. 9, pp. 2470–2476, Sep. 2008.

[8] R. S. C. Cobbold, *Foundations of Biomedical Ultrasound*. Oxford University Press, Sep. 2006.

[9] B. A. Angelsen, *Ultrasound imaging. Waves, signals and signal processing*. Emantec, 2000, vol. 1. [Online]. Available: http://www.ultrasoundbook.com/

[10] J. Bamber, Bamber, "Speed of sound, ch. 5," in *Physical Principles of Medical Ultrasonics*, 2nd ed., C. R. Hill, J. C. Bamber, and G. R. t. Haar, Eds. Wiley, Jun. 2002.

[11] R. Hansen, S. Måsøy, T. A. Tangen, and B. A. Angelsen, "Nonlinear propagation delay and pulse distortion resulting from dual frequency band transmit pulse complexes," *J Acoust Soc Am*, vol. 129, no. 2, p. 1117, 2011.

[12] M. Averkiou, D. Roundhill, and J. Powers, "A new imaging technique based on the nonlinear properties of tissues," in *Proc IEEE Ultrason Symp*, vol. 2, Oct. 1997, pp. 1561 –1566 vol.2.

[13] B. Ward, A. C. Baker, and V. F. Humphrey, "Nonlinear propagation applied to the improvement of resolution in diagnostic medical ultrasound," *J Acoust Soc Am*, vol. 101, no. 1, pp. 143–154, 1997.

[14] S. Choudhry, B. Gorman, J. W. Charboneau, D. J. Tradup, R. J. Beck, J. M. Kofler, and D. S. Groth, "Comparison of tissue harmonic imaging with conventional US in abdominal disease," *Radiographics*, vol. 20, no. 4, pp. 1127–1135, Jul. 2000.

[15] P. Jiang, Z. Mao, and J. Lazenby, "A new tissue harmonic imaging scheme with better fundamental frequency cancellation and higher signal-to-noise ratio," in *Proc IEEE Ultrason Symp*, vol. 2, 1998, pp. 1589 –1594 vol.2.

[16] D. Simpson, C. T. Chin, and P. Burns, "Pulse inversion doppler: a new method for detecting nonlinear echoes from microbubble contrast agents," *IEEE Trans Ultrason Ferroelectr Freq Control*, vol. 46, no. 2, pp. 372 –382, Mar. 1999.

[17] T. A. Tangen, "Imaging of nonlinear scattering using dual-frequency band ultrasound," Ph.D. dissertation, Norges teknisk-naturvitenskapelige universitet, Trondheim, 2010. [Online]. Available: http://ntnu.diva-portal.org/smash/get/diva2:372555/FULLTEXT02

[18] A. Bouakaz, M. Versluis, J. Borsboom, and N. de Jong, "Radial modulation of microbubbles for ultrasound contrast imaging," *IEEE Trans Ultrason Ferroelectr Freq Control*, vol. 54, no. 11, pp. 2283 –2290, Nov. 2007.

[19] R. Hansen, "New Techniques for Detection of Ultrasound Contrast Agents," Ph.D. dissertation, Department of Engineering Cybernetics, Norwegian University of Science and Technology, Trondheim, Norway, 2004, ISBN 82-471-6209-1.

[20] S. E. Måsøy, Ø. Standal, P. Näsholm, T. F. Johansen, B. Angelsen, and R. Hansen, "SURF imaging: In vivo demonstration of an ultrasound contrast agent detection technique," *IEEE Trans Ultrason Ferroelectr Freq Control*, vol. 55, no. 5, pp. 1112–1121, May 2008.

[21] S. P. Näsholm, R. Hansen, S. Måsøy, T. Johansen, and B. A. Angelsen, "Transmit beams adapted to reverberation noise suppression using dual-frequency SURF imaging," *IEEE Trans Ultrason Ferroelectr Freq Control*, vol. 56, no. 10, pp. 2124–2133, Oct. 2009.

[22] S. P. Näsholm, R. Hansen, and B. A. Angelsen, "Post-processing enhancement of reverberation-noise suppression in dual-frequency SURF imaging," *IEEE Trans Ultrason Ferroelectr Freq Control*, vol. 58, no. 2, pp. 338–348, Feb. 2011.

[23] S. Måsøy, Ø. Standal, J. M. Deibele, S. P. Näsholm, B. Angelsen, T. F. Johansen, T. A. Tangen, and R. Hansen, "Nonlinear propagation acoustics of dual-frequency wide-band excitation pulses in a focused ultrasound system," *J Acoust Soc Am*, vol. 128, no. 5, p. 2695, 2010.

[24] H. Høilund-Kaupang, "Models and methods for investigation of reverberations in nonlinear ultrasound imaging," Ph.D. dissertation, Norges teknisk-naturvitenskapelige universitet, 2011. [Online]. Available: http://ntnu.diva-portal.org/smash/record.jsf?pid=diva2:479070

Paper A

# An Ultrasound Research Scanner for Dual Frequency Band Imaging

Jochen M. Rau[1], Thor Andreas Tangen[2], Svein-Erik Måsøy[1], Tonni F. Johansen[1] and Bjørn Angelsen[1]
[1]Department of Circulation and Medical Imaging, NTNU, Trondheim, Norway,
[2]Department of Engineering Cybernetics, NTNU, Trondheim, Norway

**Abstract**

Dual frequency band imaging utilizes a sound pulse to manipulate the propagation and scattering of an imaging pulse. The bandwidth of conventional transducers is too limited to be able to transmit these pulses with a frequency ratio between 1:7 and 1:10. Dual frequency transducers have been built, but they require a different ultrasound system to operate them.

In this work a dual frequency system is presented. It is based on a commercially available research scanner which is modified and extended with a custom second transmitter and software to enable real-time operation.

The system is based on an Ultrasonix SonixRP scanner, which is a 128 transmit, 32 receive channel system for probes with up to 128 elements. It features 40 and 80 MHz sampling frequency on receive and transmit, respectively. The extension transmitter is a tri-state transmitter, working at 80 MHz sampling frequency with an amplitude of up to 250 V. It is programmable via an USB link and synchronized during operation via the scanners' trigger signals.

The systems' specifications and necessary modifications are documented. Results from water tank, pulse-echo *in vitro* and *in vivo* experiments are presented to demonstrate its capabilities.

## A.1 Introduction

Nonlinear effects are utilized for medical ultrasound imaging in clinical practice with techniques such as second harmonic imaging (SHI). Over the last years there is rising interest in separating the excitation of nonlinear effects from the imaging beam to achieve better control and enable advance imaging methods. This can be achieved by transmitting an additional sound wave which manipulates the propagation of the conventional imaging pulse, as well as the scattering properties of the medium. This is called 'radial modulation imaging', 'dual frequency band imaging' (DBI) or SURF Imaging [1–3].

There are two main application areas for techniques utilizing nonlinear effects. First, reverberation suppression, where usually the accumulation of these effects over time is used to differentiate signals originating from different depths. Second, the imaging of ultrasound contrast agents, consisting of gas filled microbubbles, where the nonlinear response of the bubbles are detected. In addition, nonlinear material parameters can be estimated as *f.ex.,* in B/A estimation. Research on dual-band imaging has been conducted in all areas, exciting nonlinear propagation, scattering and parameter estimation (in *f.ex.,* [2–6]). However there is yet no commercially available research system which provides dual-transmit capabilities and single receive for use in DBI. Such a system could also be used in other contexts as in tissue heating, drug release and inducing sonoporation to increase the permeability of tissue for drug delivery while imaging for guidance or monitoring.

In this chapter it is presented how a commercially available scanner is modified and extended into a fully operable dual frequency band system which is able to transmit on two frequency bands and receiving on one of them. Also transducers for this systems are discussed briefly, since conventional piezo-electric transducers are unable to transmit dual frequency band pulses with the required frequency ratio (1:7 .. 1:10).

## A.2 System description

From a general point of view, a dual frequency band ultrasound imaging system consists of transducers capable of converting the electrical excitation to an acoustic dual-band signal on transmit and vice versa on receive, a scanner operating these transducers and software to integrate the additional beamforming, synchronization and signal processing.

In the following the different parts of the system, transducers, the scanner platform, modifications to it, the hardware extension (which was necessary for transmit of the manipulation signal), and software additions will be detailed.

### A.2.1 Transducers

Most of the conventional ultrasound transducers currently in use in medical imaging are array transducers. They consist of an array of elements which can be excited and read independently from each other. The array is composed of a stack of layers as displayed in Fig. A.1a.

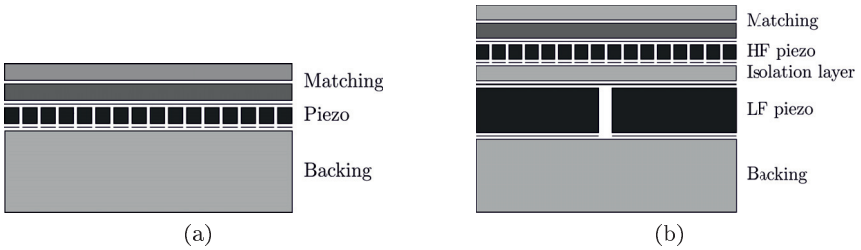


Figure A.1: Layer stack for (a) conventional and (b) longitudinally stacked dual-band transducers. The radiation direction is upwards. Electrodes are placed on both sides of each piezo electric layer with the ground electrode towards the patient.

The active layer is made of piezo-ceramics with electrodes on both sides which define the azimuthal and elevational size of the elements. The desired radial resonance mode, most commonly half-wavelength resonance, defines the thickness of the layer. The ceramics is often diced and filled with epoxy to reduce the influence of lateral oscillation modes. At the same time the average mechanical impedance is lowered and contributes to better coupling to the medium. Matching layers are often used to widen the narrow bandwidth of the thickness resonance of the ceramics layer. A maximum bandwidth of approximately 110% of the center frequency can be currently achieved with this technology [7].

If one requires separate bands with a relative bandwidth of 50% each, SHI touches this technical limit already. If the center frequency ratio is increased further, as needed for some applications, to *e.g.,* 1:10 the bandwidth requirement rises to 177%. This is well beyond the limit of what can be achieved with piezo-ceramic transducers with a single type of active elements.

Other transducer technologies, as capacitive micromachined ultrasonic transducers (CMUT), promise higher bandwidths [8], but are not yet widely applied in clinical practice. A more common way to manufacture multi-band transducers is to combine two piezo-ceramic arrays and transmit or receive each band on the corresponding array. Combining two arrays can be done in different manners:

One approach is to place the elements next to each other either as one or more separate rows [9] (*f.ex.,* in elevation) or interleaved [4] in one row. This approach keeps mostly the original bandwidth of the separate elements but attention must be paid to ensure adequate overlapping of manipulation and imaging pulse in the acoustic field. For interleaved arrays grating lobes may be introduced if the pitch becomes large.

Another approach is depicted in Fig. A.1b where the two arrays are placed on top of each other along the radial direction [10, 11]. The imaging array (high frequency) is placed closest to the radiation surface, the manipulation layer (low frequency) is placed below and both arrays share the same radiation surface. This ensures that the sound fields overlap in space. However, transmitting the manipulation wave through the imaging layer imposes constraints on the bandwidth, and cross-talk between the arrays must be addressed.

Table A.1: Properties of the presented transducer. Bandwidth is -6dB pulse-echo.

| | Manipulation array | Imaging array |
|---|---|---|
| Center frequency | 0.8 MHz | 8 MHz |
| Relative bandwidth | 26% | 50% |
| Number of elements | 52 | 128 |
| Pitch | 900$\mu$m | 300$\mu$m |
| Element size (elevation) | 8 mm | 4 mm |

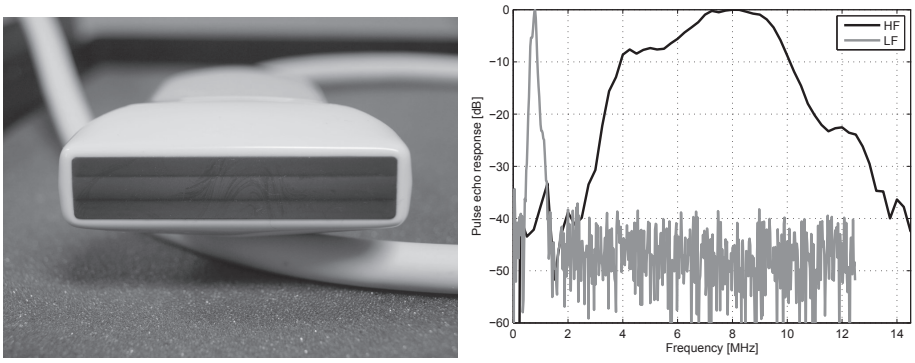


(a) (b)

Figure A.2: Details of the Vora probe: (a) Image of the footprint, (b) spectrum of pulse-echo measurements with impulse excitation (Vermon)

The transducer presented here as an example is a dual-band linear array with 0.8 MHz manipulation frequency and 8 MHz imaging frequency (see Table A.1 for further specifications). It was designed at the Department of Circulation and Medical Imaging[1] and manufactured by Vermon.[2] It consists of two radially stacked arrays. The low frequency elements exceed the high frequency elements in size both in elevation and azimuth. An acoustic lens is placed over the imaging array area. As a consequence the manipulation sound field is focused in the elevation center but unfocused where the manipulation array extends beyond the imaging array in the elevation dimension as shown in Figure A.2a. Figure A.2b displays spectra of a pulse-echo response from a flat target for both arrays. It should be noted that the low frequency elements are electrically tuned with a serial coil which improves separation between the two frequency bands. For the manipulation array the target was placed at 33.9 mm depth, for the imaging array at 14.6 mm depth. The measurements were carried out by Vermon using a negative impulse as excitation.

In the following sections, the chosen scanner platform will be presented and the

[1] Norwegian University of Science and Technology, Trondheim, Norway
[2] Tours, France, `http://www.vermon.com`

Table A.2: Overview of scanner and hardware extension properties

| | SonixRP | SonixMDP | Extension |
|---|---|---|---|
| Independent transmit channels | 128 | 128 | 64 |
| Type of transmit channels | +/-/off | +/-/off | +/-/off |
| Transmit sampling frequency | 80 MHz | 80 MHz | 80 MHz |
| Receive channels | 32 | 64 | – |
| Receive sampling frequency | 40 MHz | 40 MHz | – |
| Dynamic range A/D converter | 10 Bit | 14 Bit | – |

requirements of driving the dual-band transducers evaluated.

### A.2.2 Scanner platform

The presented system was designed to facilitate dual-band imaging on dual-band array transducers with a center frequency ratio between 1:7 and 1:10. Target imaging frequencies in the range of 3 to 10 MHz result in manipulation center frequencies between 0.3 and 1.5 MHz. As the manipulation band is supposed to be transmit only, the signal should only be received for the imaging band. The imaging band is well within what commercially available ultrasound scanners provide. This was utilized to modify and extend a conventional scanner instead of building a whole scanner from scratch.

The scanner used as a basis for the DBI scanner is a SonixRP research scanner (Ultrasonix Medical Corporation[3]) [12]. It comes with an extensive programming interface and documentation which gives access to a lot of system parameters. At the same time the system is clinically approved and can be used as a conventional scanner with access to beamformed radio-frequency (RF) data and even channel data if an additional data-acquisition unit is used. There is no other system on the market that is clinically approved and open enough for modification, assuming a close collaboration with a scanner manufacturer is not established or desired.

The front-end of the scanner consists of 128 tri-state (positive/negative/off[4]) transmitters and 32 receive channels with 10 Bit analog-digital converters (ADC). The sampling frequency on transmit is 80 MHz and on receive 40MHz (see also Table A.2). The front-end features easy access to trigger signals sent at the start of each frame and/or pulse. It has three probe ports suitable for probes with up to 128 elements. The front-end uses low-voltage multiplexers behind the transmit-receive (T/R) switch to multiplex the receive signals of the elements to the receive channels. The signals are then amplified, optionally filtered through an analog third order low-pass filter, anti-aliasing filtered and finally fed into the ADC. The signal is beamformed in the front-end electronics and the beamformed radio-frequency (RF) signal can be stored by the PC which is controlling the front-end and the graphical user interface.

[3] Richmond, BC, Canada, `http://www.ultrasonix.com`

[4] 'off' in this context expresses that there are no active components forcing the signal to 'zero' or 'ground'. However, there is most probably a bleeding resistor with a rather high value.

In addition with the Digital Acquisition Box (DAQ, Ultrasonix) [13] up to 16 GByte channel RF data can be stored when the DAQ is attached in addition to a transducer on the system.

Driving a dual-band transducer is a challenge to the scanner hardware. As the dual-band transducers consist of two arrays the channel count is higher than for single-band ones. The transducer described above has 180 elements while the scanner is offering only 128 transmit channels. For dual-band imaging the number of receive channels is not that important as the manipulation signal is transmit-only.

At the same time also the type of transmitter is limiting the system. The SonixRP features a tri-state transmitter which switches between a negative voltage, a positive voltage and the off state. Its voltage levels are equal for all channels. This would imply that the manipulation pulse always would be excited with the same voltage amplitude as the imaging pulse – which is a severe limitation of flexibility and for example not desirable in contrast imaging where the imaging pulse due to its higher frequency can and should be sent with a higher pressure than the manipulation pulse without destroying the bubbles.

In general, the implementation should be easier on a system with multi-level or arbitrary wave transmitters if enough channels are available to drive both the manipulation and imaging array. Furthermore one should also consider if the transmit beamformer is flexible enough and has enough memory to store signals for two arrays.

This was not evaluated here as already the first two aspects, the limited number of channels and the limited number of transmit voltages, made it necessary to add a hardware extension to the scanner. The extension contains an independent, 64 channel transmitter for the manipulation array with the necessary power supplies, and an adapter board to join the signals of the SonixRP and the extension transmitter in one probe connector. The extension is described in depth in the next section.

In addition to the hardware extension the scanner itself was modified. In total six modifications were made. Two of them rather basic modifications which were planned: a memory upgrade and a new front cover. Four of them altering components in the receive chain of all channels, which were necessary after observing a very limited transfer function in the imaging frequency range with -20 dB attenuation at 10 MHz compared to signal amplitude at 5 MHz, (depicted in Fig. A.5a, dashed gray line).

To assess the transfer functions, a chirp signal from a signal generator was inserted into one of the pins in the scanner probe connector. The signal amplitude was 20 mVpp and the chirp frequency range covered 0.5 to 15 MHz. The scanner was configured to record without time-depth-compensation. The first type of measurement conducted was to record the analog signal with an oscilloscope between the different components along the receive chain (*analog* measurements). Dividing the spectra of the signal before and after a component then yields the transfer function. The other type of measurement was to record the *digital* RF signal with the scanner. Since the signal was just inserted into one channel at a time beamforming does not affect the measurement as long as the corresponding channel is within the receive aperture. The digital transfer function is then found if the recorded signal is divided by the (analog) spectrum of the chirp. The analog measurements were used for the data depicted in Fig. A.5b and the black dashed line in Fig. A.5a. The other transfer functions were recorded digitally.

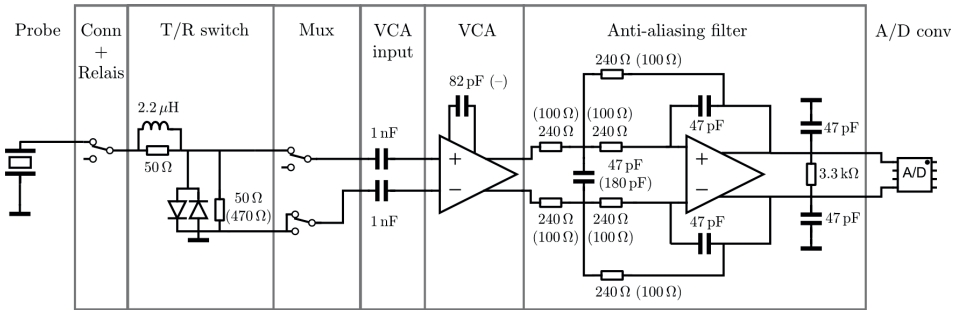


Figure A.3: Receive chain of one channel of the SonixRP. Values of the components after modification given in parentheses.

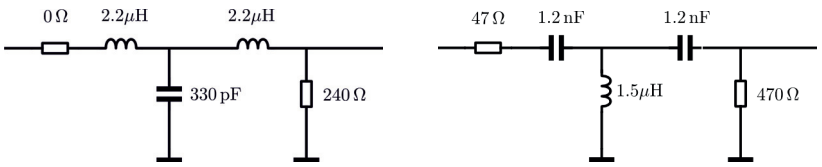


(a) prior to modification (b) after modification

Figure A.4: VCA filter configuration as a Butterworth third order low pass filter prior (a) and high pass filter after (b) modification.

**Memory upgrade** The Random Access Memory (RAM) of the integrated PC in the scanner was upgraded to 4GB to increase the cine buffer and allow to store more data per recording.

**Front cover replacement** To prevent users touching the PCB of the hardware extension in front of the scanner a new front cover was built. It provides room for the new connector and the PCB. The cover is made from rigid plastics utilizing a rapid prototype 3D-printer.

**T/R circuit modification** The T/R switch in its original form contains a serial voltage divider with a resistor ratio of 1:1. Changing the parallel resistor from 47 to 470 Ω the ratio was decreased to 1:10. As a consequence signal loss is reduced from -6 dB to -1 dB (cf. Fig. A.3).

**Adjusting the anti-aliasing filter** The anti-aliasing filter was was originally implemented as a active second order low pass filter. As Fig. A.5b (black dash-dotted line) shows, the original filter attenuated the signal with about 8 dB at 10MHz. With a 40 MHz sampling rate, the cutoff frequency is considered unnecessarily low. Adjusting the component values according to Fig. A.3 yields a second order low pass filter with a -3 dB at 13 MHz. As a consequence there is now less attenuation at the Nyquist frequency (-10 dB) than before.

**Low-pass filter in amplifier circuit removed** A first order low pass filter in the voltage controlled amplifier (VCA) circuit which attenuated parts of the HF band was removed by removing the corresponding capacitor on the board (cf. Fig. A.3, A.5b, data sheet: [14])

**Analog filter reconfiguration** Parts of the manipulation signal is scattered and returns as a low frequency echo to the transducer. For contrast imaging the manipulation pressure is low but for reverberation suppression the pressure, and in turn the echo, is substantial. Due to the large separation between imaging and manipulation band, filtering out the low frequency component is feasible. However, the ADC has a limited dynamic range and the low frequency echo will reduce the dynamic range available for the imaging signal. Thus, if possible, the manipulation signal should be filtered before the receive signal is digitized.

The SonixRP features an optional third order Butterworth low pass filter. This was reconfigured to a third order high pass filter which can be used for dual-band imaging while it can be switched off for conventional imaging. The filters' transfer function is shown in Fig. A.4. Its low frequency -3 dB cutoff is at 2.5 MHz.

#### A.2.2.1 Next generation

While the dual-band scanner was fully operable in early 2010, Ultrasonix has since presented a new model of their research scanner called SonixMDP. The front-end

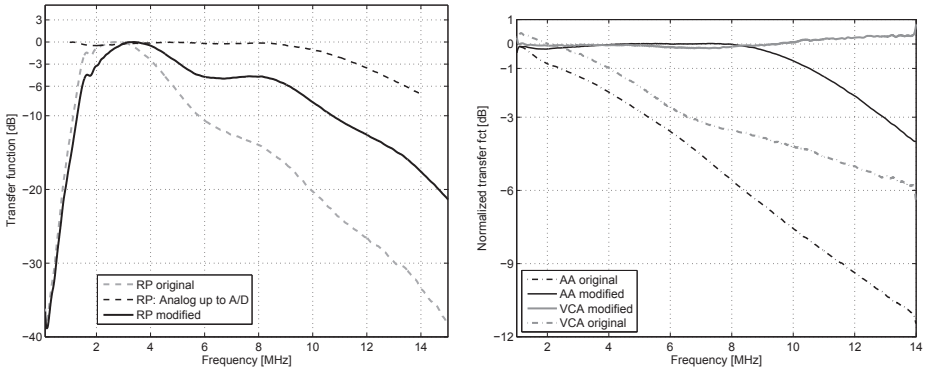


(a) (b)

Figure A.5: (a)Measured transfer functions for the SonixRP scanner, prior and after modification. Additionally the analog transfer function up to the input of the ADC is given. (b) Transferfunctions of the anti-aliasing and the low pass filter in the VCA filter prior and after modification.

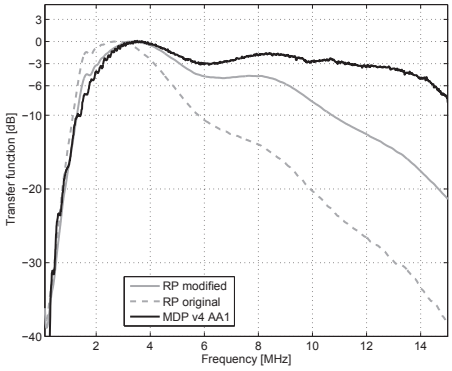


Figure A.6: Comparison of the measured transfer functions for both the SonixRP and the SonixMDP scanner. (SonixRP prior and after modification)

electronics is improved compared to the SonixRP and now features 64 receive channels with 14 Bit AD converters. The analog filters were removed as well as the low-pass in the amplifier. The anti-aliasing filter is now configurable in software and the T/R switch chip was changed and does no longer show low-pass characteristics.

The transfer function of the SonixMDP system is displayed in Fig. A.6. Analog assessment of single components, like it was done for the SonixRP, is not feasible in the SonixMDP system since the only components present in the receive chain is the T/R switch and the front-end chip which includes the ADC.

Our department purchased a SonixMDP scanner in 2010 which, as of 2012, replaced the SonixRP for nearly all applications. Due to the hardware improvements and changes mentioned above the hardware modifications were either not necessary (T/R switch, AA filter) or feasible (additional high pass filter) on the SonixMDP.

As the hardware extension is mounted on the scanner as a conventional probe, and Ultrasonix did not alter the probe connector or the trigger signals it is possible to use it together with the SonixMDP system. However, a tight integration with front cover and mounting the extension unit on the scanner is still pending.

### A.2.3 Hardware extension

The hardware extension consists of the low frequency (LF) transmitter for the manipulation pulse, the high frequency (HF) imaging signal multiplexer assembly, a digital signal processor (DSP) based logic unit and five power supplies (see fig. A.7). It was designed in collaboration with and manufactured by Norbit AS[5].

Figure A.7 shows schematically the configuration and interaction of the system consisting of the scanner, the hardware extension and a transducer. One probe port of the conventional scanner is used to transmit and receive the imaging signals. The hardware extension is coupled in-between the probe port and the probe. The imaging signals may be multiplexed with high voltage multiplexers if the dual-band probe features more imaging elements than the scanner has transmitters. This feature is currently not used, so its documentation is here kept to a minimum. The manipulation signals are provided by the low frequency transmitter and led to the probe connector. The scanner configures the hardware extension via a USB link. The scanner's pulse and frame trigger signals are the only way of synchronization and real-time interaction between the scanner and the hardware extension.

**LF pulser** The LF transmitter emits rectangular pulses with sampling frequencies up to 80 MHz and even fractions of it given by:

$$f_s = \frac{80\text{MHz}}{2^n}, \qquad n = 0..5 \tag{A.1}$$

The LF transmitter is a tri-state pulser with $V_+$, $V_-$ and 'off' as valid states. The two voltages can be controlled independently of each other within the range of 0 to 250 V. The upper limit of the voltage is given by the output stage transistors (TC1550,

[5] Trondheim, Norway, `http://www.norbit.no`

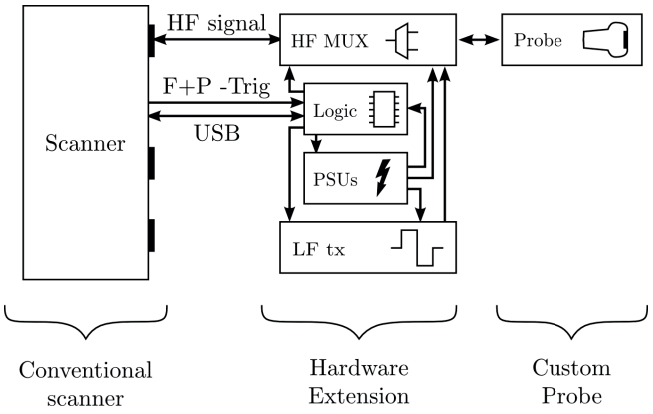


Figure A.7: Block diagram showing the conventional ultrasound scanner which is extended with a front-end consisting of a high voltage MUX assembly ('HF MUX') aggregating the high-frequency imaging signals and the low frequency manipulation signals, power supply units ('PSUs'), a tri-state transmitter for the low frequency manipulation ('LF tx') signals and a digital signal processor ('logic') to control the operation.

Supertex[6]). For each channel two transistors in parallel are employed to reduce the serial resistance and enable higher current. The transmitter is able to drive 64 master channels independently of each other. Additionally every master channel has one slave channel which, if enabled, transmits the same signal as the master channels. Thus a three elevation row 1.25D array can be driven.

**Logic unit** The transmit of one beamformed pulse is defined in a pulse pattern and stored in 512 MByte RAM which is managed by the DSP (ADSO BF-561 500MHz, Analog Devices Inc[7]). Several pulse patterns can be stored to support *e.g.,* dual-pulse dual-band operation, pulse inversion, and multiple focus setups. The number of patterns which can be stored is limited by the available memory and dependent on the size of the patterns. Each sample in time for each of the 64 master channels is stored as a 2-Bit value. As an example: A setup for 2.5 periods of 1 MHz transmit frequency, sampled at 80 MHz, 192 different beams, 2 pulses in each direction, 3 foci consumes:

$$0.25\,\text{Byte} \cdot 2.5 \cdot \frac{1/1\,\text{MHz}}{1/80\,\text{MHz}} \cdot 64 \cdot 192 \cdot 2 \cdot 3 = 3.5\,\text{MByte} \tag{A.2}$$

To communicate with the ultrasound scanner, *e.g.,* to download the pulse patterns, a USB 2.0 link is used. However, during operation there is no communication necessary: As soon as the pulse pattern is defined and the transmitter activated it will act upon the frame and pulse trigger signals emitted by the scanner.

[6]Sunnyvale, CA, USA, `http://www.supertex.com`
[7]Norwood, MA, USA, `http://www.analog.com`

**Multiplexer assembly** The MUX assembly has two basic functions. First, the channels for imaging and manipulation signals are gathered into one probe connector. Second, it contains an array of 1:2 high voltage multiplexers which allow multiplexing the 128 channels for the imaging signal to a 192 element probe.

Additionally probe identification is routed through the PCB board of the MUX assembly.

The multiplexer board features four connectors: One 156 pin plug (DL1-156, ITT Cannon[8]) towards the Ultrasonix scanner and a 360 pin receptable (DLP408-R-1, ITT Cannon[8]) towards the dual-band probe. In addition there are connections to the logic unit and the power supplies.

**Power supply units** The extension needs several different supply voltages. The output voltage of the LF transmitter is provided by two ES0300-0.45 lab power supplies (Delta Elektronika BV[9]). These power supply units (PSUs) can be controlled via analog voltages to define the output voltage within the range of 0 to 300 V and a maximum average current from 0 to 0.45 A. They are extended with an additional isolation on the secondary side increasing the isolation to 1000V and an option to sense the output voltage for monitoring purposes.

The high voltage multiplexers demand a supply voltage at least as high as the transmit voltage. A supply voltage of +-100 V was chosen and is delivered by two 32150A power supplies (Calex Electronics Ltd[10]).

The supply for the logic and low voltage components is delivered by a 12 V GSM28 Medical (SL Power Electronics Corp[11]) which then is converted via DC/DC converters to 3.3 V and 5 V respectively.

**Package and assembly** Figure A.8 shows the assembly of the scanner. The hardware extension is divided into two parts. One part is the printed circuit board (PCB) board for multiplexing and integrating the HF and LF signal lines into one connector. This board is mounted in the same way as a common probe would be to the scanner using one of the probe connectors.

The remaining components, including the PSUs and the PCB for the LF transmitter, are placed in a "backpack" on the rear part of the scanner. In that way the scanner can still be moved to clinical tests as a conventional scanner in one piece on its own wheels. A custom front cover hides the electronics and gives place for the bigger dual-band probe connector.

### A.2.4 Software

The SonixRP system is a system aimed for use in research. One of its features is full access to all imaging parameters. The parameters can be changed in real-time either through the graphical user interface of the imaging software or programatically using

[8] Santa Ana, CA, USA, `http://www.ittcannon.com`
[9] Zierikzee, The Netherlands, `http://www.delta-elektronika.nl`
[10] Bedfordshire, UK, `http://www.calex.co.uk`
[11] Ventura, CA, USA, `http://www.slpower.com`

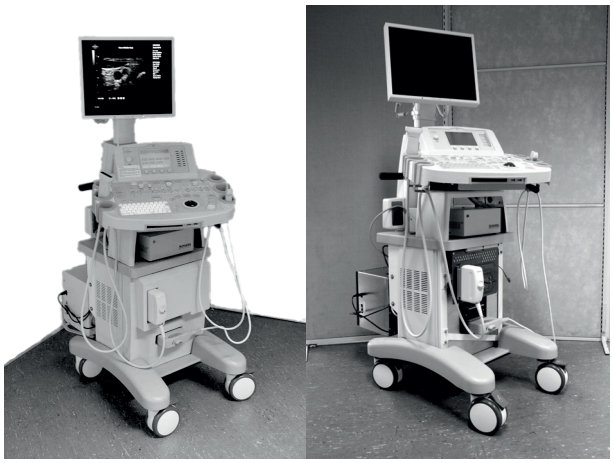

(a) (b)

Figure A.8: Dual-band scanner, (a) ready for use, (b) with front cover removed so the placement of the components with a printed circuit board (PCB) combining the LF and HF signals into one connector and the HF multiplexers in the front and a "backpack" with the rest of the extension hardware mounted on the back of the scanner can be seen.

the "Ulterius" application programming interface (API). This gives the researcher full flexibility in setting up the transmit/receive beams and receive processing.

The API also offers the possibility to retrieve RF data at full frame rate from the system, process it and send the image back to the imaging software for display. This way new processing algorithms can be tested in real-time in the lab or the clinic. However, care has to be taken to ensure stable operation.

For the dual-band frequency system presented here, Ultrasonix implemented a plugin feature to the system in order to integrate novel processing schemes into the system. RF data and additional imaging parameters are passed to the plugin and envelope detected data is returned from the plugin to the SonixRP imaging software, see Figure A.9. Three processing steps are performed in the plugin: IQ demodulation, application specific processsing and envelope detection.

IQ demodulation is implemented by down mixing the RF signal with a specified demodulation frequency and then low pass filtering

$$x_{IQ}(t) = \mathrm{LP}\left\{x_{RF}(t)\,\mathrm{e}^{-\mathrm{i}2\pi f_d t}\right\} \tag{A.3}$$

where $f_d$ is the demodulation frequency and $\mathrm{LP}\{\cdot\}$ denotes low-pass filtering.

The application specific processing can be any signal processing method, *e.g.*, the subtraction of the first and second pulse transmitted in each direction to remove clutter [15] or delay estimation and correction before subtraction in order to image ultrasound contrast agents [3].

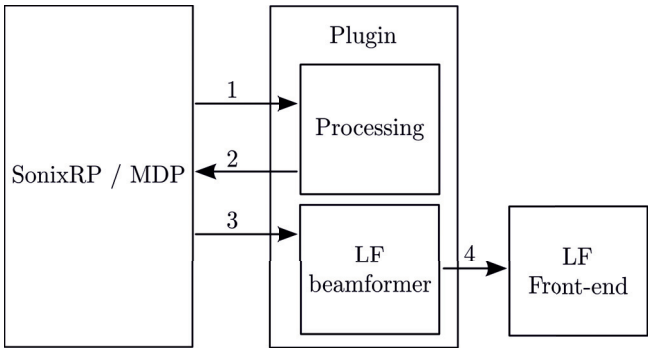


Figure A.9: 1: RF signals at 40 MHz sampling rate and processing parameters is passed from SonixRP to the plugin for processing. 2: Envelope detected image data is passed back to SonixRP for display. 3: LF transmit beamforming parameters are passed from SonixRP to the plugin. 4: Beamformed LF pulses are downloaded to the LF frontend memory.

Envelope detection is the operation of computing the magnitude of the IQ signal.

The signal processing in the plugin is implemented using the Intel Integrated Performance Primitives library (Intel Corporation[12]) which offers optimized signal processing functions which utilizes instruction set extensions found in most desktop CPU's.

Furthermore the plugin deals with setting up the LF manipulation beamforms according to the given parameters and controls the LF front-end. Additional global parameters to control the LF beamforming and the application specific processing were added by Ultrasonix to their parameter set for the system.

As in conventional scanner operation, the raw beamformed RF-data, which is input to the plugin, can be saved for later offline processing and inspection.

Besides the real-time capabilities, a MATLAB (Mathworks[13]) interface to control the hardware extension and setup a LF transmit was developed. It was mainly used in the development phase of the software plugin. For laboratory experiments also the Ultrasonix scanners can be controlled via a in-house developed MATLAB or recently Python[14] tools.

## A.3 Experiments

In the following section, some of the capabilities of the system are demonstrated in a number of experiments. First the operation of the LF pulser is documented, followed by the transmit performance of the scanner together with the LF pulser in hydrophone measurements and finally pulse-echo measurements with the system, both *in vitro* and *in vivo*.

[12]Santa Clara, CA, USA, `http://www.intel.com`
[13]Natick, MA, USA, `http://www.mathworks.com`
[14]`http://www.python.org`

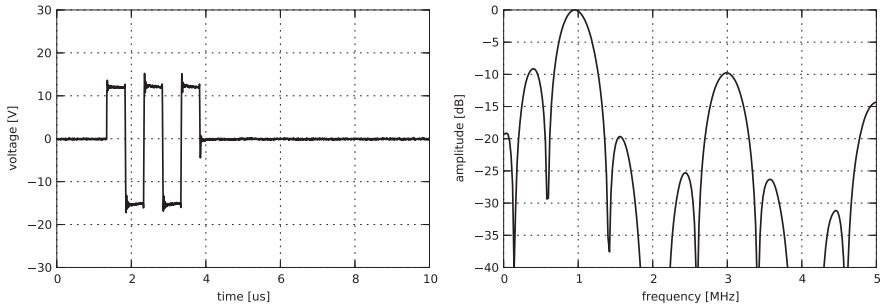


(a)

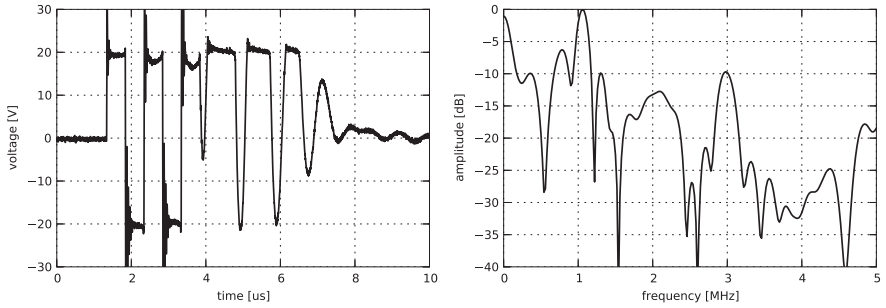


(b)

Figure A.10: Voltage trace of the LF pulser (a) into 50 Ω and (b) into a LF element of the Vora probe and their respective spectra for a target amplitude of 20 $V$

### A.3.1 LF pulser

The signal of one channel of the LF pulser was recorded with an oscilloscope for different loading conditions. Figure A.10 shows the voltage traces and fourier transforms of the signals. The target amplitude was configured to 20 V and the transmit frequency is 800 kHz with five half-cycles pulse length. In panel (a) the transmitter is loaded with a 50 Ω resistor while it is loaded with the Vora probe (120 Ω at 800 kHz) in panel (b). The pulse exhibits a long tale which is attributed to energy stored in the capacity of the cable and the transducer element.

### A.3.2 System – water tank

With the Vora probe attached to the DBI scanner, the transmitted signal was recorded with a hydrophone (200 $\mu$m HGL-0200, Onda Corporation[15]) in a water tank on the beam axis. The excitation consisted of a plane wave (5 half-cycles at 0.8 MHz) on the

[15]Sunnyvale, CA, USA, `http://www.ondacorp.com`

manipulation array and a focused wave (2 half-cycles at 8 MHz) on the imaging array.

Figure A.11a depicts two dual frequency band pulse complexes, one with the imaging pulse in a compression phase, another one in an expansion phase. The frequency spectrum is given in panel (b). Panel (c) shows the remaining signal when the pulse complexes with positive and negative manipulation are filtered with a band pass filter around their imaging frequency. Note the accumulated propagation delay between the two imaging pulses.

### A.3.3 System – pulse-echo *in vitro*

To demonstrate the pulse-echo capabilities of the developed system the Vora probe was placed on a homogeneous scattering phantom (Model 049, Elasticity QA phantom, CIRS Inc[16]). Two SURF pulse complexes were transmitted for each line. One with the imaging pulse in a compression phase of the manipulation pulse (*plus* pulse) and another one in an expansion phase (*minus* pulse).

Figure A.12a displays a small section of the rf signal recorded for both the *plus* and the *minus* pulse for one line. The phase shift due to the manipulated propagation velocity is clearly visible.

Estimation of the delay between the postive and negativ manipulated imaging pulse from echo data is central in most types of dual band imaging processing. In panel (b) the delay vs. depth is estimated as described in [16] and depicted for all lines in the image. The delay is quite homogeneous across the image despite two regions with reduced delays, one at the outer left side and one at 8mm azimuth length, which are attributed to transducer defects. The delay is increasing with depth for all lines. Panel (c) shows delay from one representative line vs. depth. In addition, the mean across the lines and the standard deviation is depicted to visualize homogeneity. The statistical properties are computed across all lateral lines in the image. In the near field the estimate is rough. With increasing depth it is nearly linear until the end of the line where the estimate again shows strong variations. For panel (d) the mean and standard deviation were only computed for all lines with a lateral position $15\,mm \leq x \leq 30\,mm$, where the transducer is reliable.

### A.3.4 System – pulse-echo *in vivo*

With the same imaging settings as in the previous section, the brachialis artery of a healthy volunteer was imaged. Figure A.13a shows the conventional B-Mode image. The lower arrow marks the artery while the upper one was placed in a vein. The artery is visualized better than the vein which is filled with clutter in large parts across the image. The delay estimated along the dashed line is presented in panel (b) in the same figure. For comparison the delay line which was acquired with the phantom in the section above is also plotted (gray line). The arrows highlight the position of the two vessels, where the delay is considerably lower. Panel (c) shows the estimated delay over the whole image.

[16] Norfolk, Virginia, USA, `http://www.cirsinc.com`

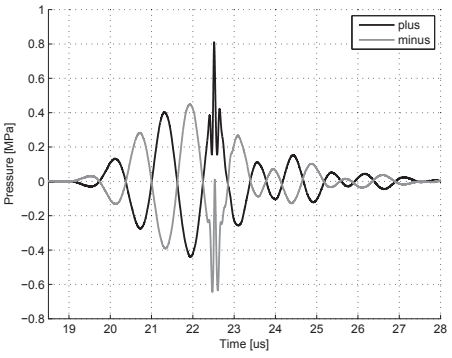


(a) Pulse complexes with an imaging pulse experiencing positive (black) and negative (gray) manipulation

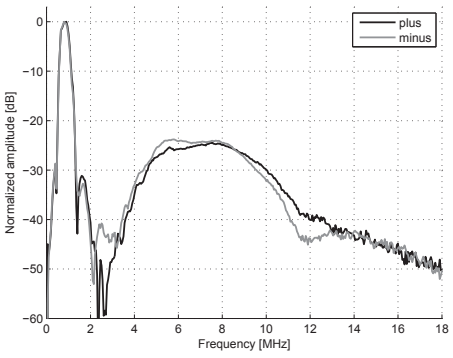


(b) Frequency spectra

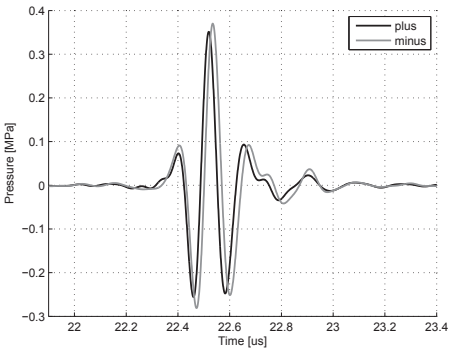


(c) Filtered complexes to preserve the imaging band signal. Note the propagation delay.

Figure A.11: Hydrophone measurements of dual frequency band pulse complexes. Transmitted with the Vora probe attached to the SonixMDP scanner. Signal recorded at focus on the beam axis.

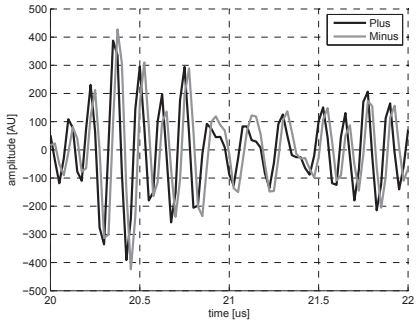


(a) RF line 66 (19.5 mm), *plus* and *minus* pulse at approx. 16 mm depth

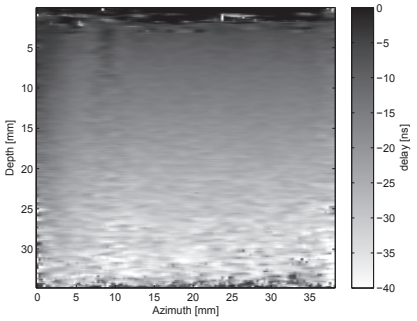


(b) Estimated delay between *plus* and *minus* imaging pulse

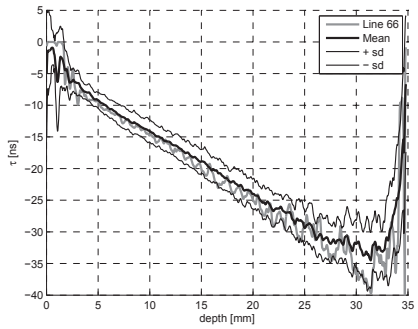


(c) Estimated delay of line 66 (19.5 mm) together with mean +/-standard deviation across whole aperture

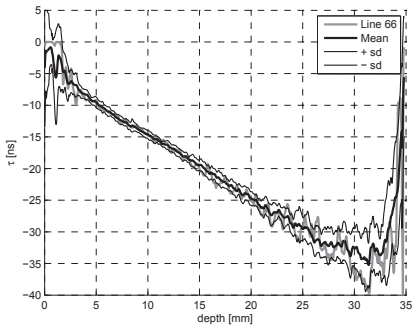


(d) Same plot as (c) with the mean and standard deviation computed for all lines with lateral position $15\,mm \leq x \leq 30\,mm$

Figure A.12: Examples from imaging a tissue mimicking phantom

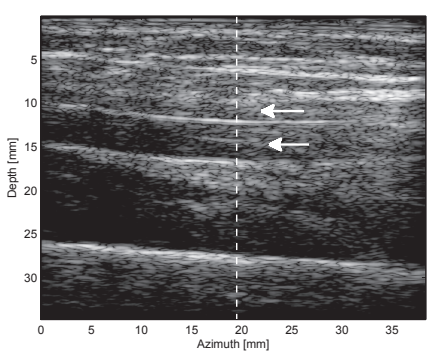


(a) Conventional BMode image

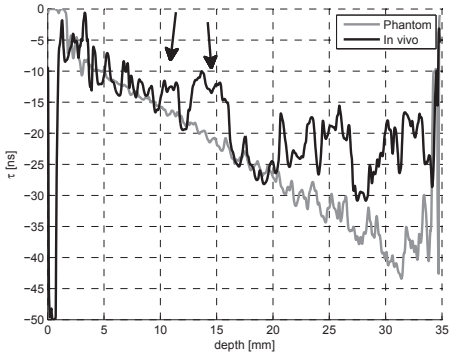


(b) Estimated delay one line for both the *in vivo* and (gray) *in vitro* setting

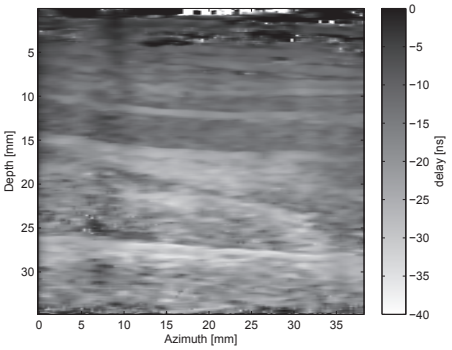


(c) Estimated delay between *plus* and *minus* imaging pulse for all lines in image

Figure A.13: Examples from imaging the brachialis artery in the upper arm. The dashed line in (a) indicates the position of the line displayed in (b); The arrows in these two pictures are placed at the same positions for better orientation.

## A.4 Discussion

An ultrasound scanner supporting single array receive and independent dual-array transmit was described. It was built as a modification of an existing system. This is a feasible way for academic research groups, as it avoids building a new scanner from scratch and keeps time and money spent on creating infrastructure at an affordable level. The system's limitations are commented in the following subsection. Subsequently the given results and examples are discussed.

### A.4.1 The DBI scanner and its limitations

The scanner which the system was built upon, the Ultrasonix SonixRP, is a low- to mid-range scanner. Its specifications (see Table A.2) are all limited compared to other commercial scanners. Several of these issues were improved in the successor as the SonixMDP scanner which features 64 receive channels and 14 Bit ADCs. Nevertheless a higher sampling frequency and a multiple of receive channels would clearly improve the performance of the system. The system's major advantage is the openness, the programming interface and that Ultrasonix actively supports the use of the scanner as a research platform.

After initial operation of the hardware extension, it was discovered that the transfer function of the receive front-end was not sufficient in the upper part of the imaging band, which led to the modifications described in Section A.2.2. Replacing components and adjusting filters as described in section A.2.2 leveled out the transfer function. The black dashed line in A.5a illustrates that up to the ADC there was only the anti-aliasing filter active as intended, but otherwise the transfer function is flat. The responses up to now were recorded with an oscilloscope between the different receive chain components. If the system is used for recording, thus also the digital signal chain is applied, the spectrum differs from the analog signal at the ADC as the gray line shows. The authors assume that there is a (misconfigured) digital filter applied prior to or right after beamforming. This was also communicated to Ultrasonix who has not found the error yet. Also the new platform shows ripple up to 3 dB in the passband which is not indicated in the datasheet of the current receive front end chip (*cf.* Fig. A.6).

The SonixRP features an optional 3-pole analog filter behind the T/R switch but before the received signal is fed into the ADC. This filter was reconfigured from being a low- to being a high-pass as described earlier. The SonixMDP lacks this feature. The imaging array of the transducer is to some degree also sensitive in the manipulation frequency band and the amplitude of the manipulation signal can be as strong as the imaging signal or even exceed it (*cf.* Fig. A.11b). Therefore the received signal contains a significant amount of backscattered manipulation signal. This is undesirable and limits the usable dynamic range of the imaging signal. Implementing an analog filter behind the T/R switch would force a replacement of the whole receive front-end of the scanner and was thus for the SonixMDP considered not feasible.

Dual-band imaging demands good synchronization in order to transmit the manipulation and imaging pulse in a defined phase relation to each other. As the hardware

extension and the scanner run on two different clock signals, jitter could occur when the extension triggers on the scanner signals. Therefore the extension features a clock synchronization circuit to keep the trigger jitter below 2 ns. In operation this seemed to work sufficiently well, as no adverse effects due to jitter were observed. In the SonixMDP, Ultrasonix added the possibility to make the internal clock signal accessible on one of the two trigger outputs which could be used for improved synchronization. But as the scanner still only features two trigger output signals, clock, pulse and frame trigger cannot be accessed at the same time, so it is not considered a real option here.

The hardware extension features 64 master channels with the possibility to duplicate their signals on 64 slave channels. This limits the flexibility in operation as *e.g.,* focusing in elevation on a 1.5 D array with 64x3 elements is not possible. An implementation of totally independent channels would improve the performance but also cause a major rework of the hardware.

In addition, the extension front-end drivers are not able to switch from one voltage to the other without one sample in "off" state. This reduces the effective sampling rate to 40 MHz.

If the multiplexers of the hardware extension are used, the reprogramming is done with an 8 MHz clock. The reprogramming, if done while imaging, caused visible artefacts in the image. These could be removed by postponing the reprogramming between each line in the image with a cost of lower pulse repetition frequency.

The duration of downloading a new beam setup to the hardware extension is limited by the USB connection to the PC. If many beam setups are needed to form a frame this could lead to a short break in imaging after a parameter (*f.ex.,* the focus depth) is changed. The large internal memory opens for downloading a series of setups and then choosing one of them, avoiding the repeated download. This is not implemented as of 2012, but may become interesting to realize a responsive user experience at a later stage.

The only means for communication between the scanner and the hardware extension are the trigger signals and the USB link. The implemented USB protocol features only communication initiated by the scanner. In case of an error on the extension, the error messages have to be polled.

Pulse width modulation (PWM) could be applied to realize apodized and non rectangular excitation, or to transmit compensation pulses after transmit to reduce transducer ringing. However, the current transmit sampling frequency on both the scanners and the extension is too low to make this work properly.

### A.4.2 Experiments

The electric pulses displayed in Fig. A.10 show that the pulser is capable of appropriately driving the transducer. The waveform with the transducer as load in Fig. A.10b indicates that it should be possible to achieve shorter manipulation pulses if a suitable out of phase damping excitation is applied to attenuate the ringing of the element.

The hydrophone measurements (Fig. A.11) show that both the system and the transducer are able to transmit dual-band pulse complexes. The amplitude of the imaging wave was chosen to be quite low for the purpose of illustration. In a real

imaging situation the manipulation and imaging pressure would be adjusted according to the purpose. For example in reverberation suppression where a delay accumulation is desired, the manipulation pressure would be in the order of the imaging pressure, while for contrast agent imaging the manipulation pressure is reduced to a minimum to avoid destruction of the contrast agent.

The filtered pulses in Fig. A.11c demonstrate the accumulation of nonlinear propagation delay. It also shows slight nonlinear distortion of the pulses deforming the shape of the *minus* pulse different from the *plus* pulse. An in-depth discussion of the propagation acoustics of dual-frequency pulse complexes can be found in [10].

The pulse-echo capabilities are demonstrated *in vitro* in Fig. A.12 and *in vivo* in Fig. A.13. Fig. A.12a shows a RF line close to the center of the transducer's aperture. Here the accumulated propagation delay and also some distortion is visible. The next panel shows the homogeneity of the estimated delay across the aperture. The delay is not homogeneous on the borders and in the left part of the image at around 8 mm. In the middle of the field of view, the low frequency transmit aperture is typically 1.5 to 2 times as wide as the high frequency aperture. This ratio cannot be maintained on the edge of the transducer, resulting in an asymmetric or weaker manipulation field and in turn to less delay towards the edges of the field of view. Additionally, the used transducer is a prototype array and has a dead low frequency element at the left border, and at 8 mm. This weakens the manipulation field and in turn the accumulated delay. There is a difference between the standard deviation in delay across the image if the regions with dead elements are taken into account and if they are disregarded as can be seen in Figs. A.12c and A.12d.

The standard deviation across the image is considerably higher in the beginning and towards the end of the lines. The latter can be attributed to the decreasing signal-to-noise ratio with depth. The former is a result of both near-field inhomogeneities and amplifier saturation due to the high signal amplitude which makes delay estimation challenging.

The *in vivo* image in Fig. A.13a depicts the brachialis artery in the upper arm (lower arrow) together with a vein (upper arrow). While the artery is well visualized the vein is filled with noise. Both vessels can be identified in the delay line along the dashed line (arrows). The accumulated delay of the echogenic areas fits well with the delay acquired on the same line *in vitro*. The delay image in panel (c) is also impaired by the transducer defects as in the phantom.

## A.5 Conclusion and future perspective

A commercially available research scanner was extended in both hard- and software to enable both real-time operation and recording for dual frequency band imaging purposes. *In vitro* and *in vivo* experiments demonstrate the functional capability of the system.

To take the DBI scanner further, deeper integration with the basis system is necessary. Adjusting the connector board of the Ultrasonix scanner to directly feature a dual-band probe connector would be one natural step in order to drop one of the

PCBs and two connections. A set of analog filters in the receive line would be another step helping to increase the usable dynamic range of the scanner. Higher sampling frequencies enabling PWM are desirable.

## Acknowledgement

The discussions and close collaboration with Ultrasonix Medical Corporation and especially Kris Dickie is thankfully acknowledged. The same applies to Norbit AS and Magnus Andersen for their effort and enthusiasm in developing, producing, and testing the hardware extension. Eskild Westby is acknowledged for the design and construction of the front cover. John Olav Horrigmo and the electrical workshop of the Department of Cybernetics is acknowledged for a lot of proper soldering on the receive electronics.

## Bibliography

[1] E. Chérin, J. Brown, S. Måsøy, H. Shariff, R. Karshafian, R. Williams, P. N. Burns, and F. S. Foster, "Radial modulation imaging of microbubble contrast agents at high frequency," *Ultrasound Med Biol*, vol. 34, no. 6, pp. 949–962, Jun. 2008.

[2] T. A. Tangen, "Imaging of nonlinear scattering using dual-frequency band ultrasound," Ph.D. dissertation, Norges teknisk-naturvitenskapelige universitet, Trondheim, 2010. [Online]. Available: http://ntnu.diva-portal.org/smash/get/diva2:372555/FULLTEXT02

[3] R. Hansen and B. A. Angelsen, "SURF imaging for contrast agent detection," *IEEE Trans Ultrason Ferroelectr Freq Control*, vol. 56, no. 2, pp. 280–290, Feb. 2009.

[4] A. Bouakaz, F. t. Cate, and N. d. Jong, "A new ultrasonic transducer for improved contrast nonlinear imaging," *Physics in Medicine and Biology*, vol. 49, no. 16, pp. 3515–3525, Aug. 2004.

[5] R. Hansen, S. Måsøy, T. F. Johansen, and B. A. Angelsen, "Utilizing dual frequency band transmit pulse complexes in medical ultrasound imaging," *J Acoust Soc Am*, vol. 127, no. 1, p. 579, 2010.

[6] H. Fukukita, "Ultrasound pulse reflection mode measurement of nonlinearity parameter B/A and attenuation coefficient," *The Journal of the Acoustical Society of America*, vol. 99, no. 5, p. 2775, 1996.

[7] S. T. Lau, H. Li, K. S. Wong, Q. F. Zhou, D. Zhou, Y. C. Li, H. S. Luo, K. K. Shung, and J. Y. Dai, "Multiple matching scheme for broadband 0.72Pb(Mg1/3Nb2/3)O3?0.28PbTiO3 single crystal phased-array transducer," *Journal of Applied Physics*, vol. 105, no. 9, pp. 094908–094908–5, May 2009.

[8] J. Chen, "Capacitive micromachined ultrasonic transducer arrays for minimally invasive medical ultrasound," *Journal of Micromechanics and Microengineering*, vol. 20, no. 2, p. 023001, Feb. 2010.

[9] G. Ferin, M. Legros, N. Felix, C. Notard, and L. Ratsimandresy, "3F-6 Ultra-Wide bandwidth array for new imaging modalities," in *Proc IEEE Ultrason Symp*, Oct. 2007, pp. 204 –207.

[10] S. Måsøy, Ø. Standal, J. M. Deibele, S. P. Näsholm, B. Angelsen, T. F. Johansen, T. A. Tangen, and R. Hansen, "Nonlinear propagation acoustics of dual-frequency wide-band excitation pulses in a focused ultrasound system," *J Acoust Soc Am*, vol. 128, no. 5, p. 2695, 2010.

[11] T. Johansen, J. Deibele, S.-E. Måsøy, R. Hansen, and B. Angelsen, "Design and Test of a Dual-Layer, Dual Frequency SURF Array," *Proceedings of the 31st Scandinavian Symposium on Physical Acoustics, ISBN 978-82-8123-007-1,*, May 2008.

[12] T. Wilson, J. Zagzebski, T. Varghese, Q. Chen, and M. Rao, "The ultrasonix 500RP: a commercial ultrasound research interface," *IEEE Trans Ultrason Ferroelectr Freq Control*, vol. 53, no. 10, pp. 1772–1782, 2006.

[13] C. C. Cheung, A. C. Yu, N. Salimi, B. Y. Yiu, I. K. Tsang, B. Kerby, R. Z. Azar, and K. Dickie, "Multi-channel pre-beamformed data acquisition system for research on advanced ultrasound imaging methods," *IEEE Trans Ultrason Ferroelectr Freq Control*, vol. 59, no. 2, pp. 243–253, Feb. 2012.

[14] "Dual, VARIABLE GAIN AMPLIFIER with low noise preamp," Apr. 2004. [Online]. Available: http://www.ti.com/product/vca2612

[15] S. P. Näsholm, R. Hansen, S. Måsøy, T. Johansen, and B. A. Angelsen, "Transmit beams adapted to reverberation noise suppression using dual-frequency SURF imaging," *IEEE Trans Ultrason Ferroelectr Freq Control*, vol. 56, no. 10, pp. 2124–2133, Oct. 2009.

[16] Ø. Standal, T. Tangen, and B. Angelsen, "P2D-4 a phase based approach for estimation and tracking of locally variable delays," in *Proc IEEE Ultrason Symp*, 2007, pp. 1583–1585.

Paper B

# 2D Reverberation Simulation and Experimental Validation

Jochen M. Rau[1], Halvard Høilund-Kaupang[1] and Bjørn Angelsen[1]
[1]Department of Circulation and Medical Imaging, NTNU, Trondheim, Norway,

**Abstract**

In medical ultrasound imaging, single reflection or scattering of the transmitted pulse is assumed. Reverberations are multiple reflections and scattering and occur as artifacts in ultrasound images. A recently presented classification scheme predicts that third order reverberations with the transducer as second reverberator always act in reciprocal pairs. Aside from nonlinear propagation differences, in beamformed signals, the components of the reverberation pairs cannot be distinguished.

A two dimensional *in vitro* setup is investigated in simulation with the spectral element method and in water tank experiments. The setup consists of a point and a planar reverberator which is insonified by a focused beam of a linear array. Different combinations of distances between transducer and reverberators are evaluated. Channel data is recorded prior to beamforming.

With the channel data, the existence of reverberation pairs can be confirmed. Simulations and experiments are in good accordance with each other. In reverberation simulations the inner structure of the transducer plays a role. Approximating it as a reflecting plane surface yields differences in reverberation arrival time when compared to experiments.

This paper is being prepared for submission to the Journal of the Acoustical Society of America

## B.1 Introduction

Signal processing in ultrasound imaging is built on several assumptions: The medium is assumed to have a constant speed of sound, multiple scattering and reflection is ignored and beam side lobes are disregarded. Even though these assumptions over time have proven to be useful and robust, they are quite often violated. In this case image quality can be impaired by artifacts which range from being subtle to clearly visible and disturbing depending on their strength.

Multiple scattering and reflection artifacts, called reverberations, occur if sound is reflected[1] several times between interfaces or structures within the (heterogeneous) medium and/or the transducer. Mostly, reverberations are discerned as haze over the image, especially as a tail on strong reflectors. Strong reverberations may become visible as replica of structures in the medium, and may this way be identified as artifact.

A classification scheme for reverberations in medical ultrasound imaging was recently presented [1]. It states that third order reverberations (reverberations which occur if the sound wave has been reflected three times) with the transducer as second reverberator always act in pairs. While the presented theory was general, its simulated examples were performed with plane reflectors only. An experimental validation was not conducted.

The components of these reverberation pairs (see also Fig. B.2) travel the inverse propagation path of each other. If the first and the third reverberators are located at different depths, one of the components has its first reflection in a shallow depth, close to the transducer, while the first reflection of the other component is at greater depth, closer to the imaging target. Assuming linear propagation of the ultrasound pulse and with proper beamforming with the same transmit and receive beam applied, both components are equal.

If the propagation velocity is pressure dependent nonlinear propagation is observed which will accumulatively distort the imaging pulse on its propagation path through the tissue. The distortion leads to a energy transfer from the fundamental frequency band to its harmonics. This is utilized in tissue harmonic imaging (THI) where the received signal is filtered with a band around twice the transmit frequency to create the imaging signal [2–4]. THI is a widely used technology to suppress reverberation noise. For THI it is assumed that the scattered wave will no longer experience nonlinear distortion. Thus the point of first reflection defines the degree of distortion of a reverberation. With regard to the reverberation pair, the shallow component will be attenuated well by THI, while the deep component will not be attenuated to the same degree [1].

This article presents a reverberation simulation study with a simulation phantom in two dimensions consisting of a plane reflector and a point scatterer. In addition, the simulation results are validated with channel data recordings from a corresponding phantom in a water tank. Straight transmit as well as oblique transmit is investigated.

[1] The term "reflected" will be used throughout the article as a collective term for both scattering from a point and specular reflection from a plane. If a distinction is necessary they will be termed "scattering" or "specular reflection"

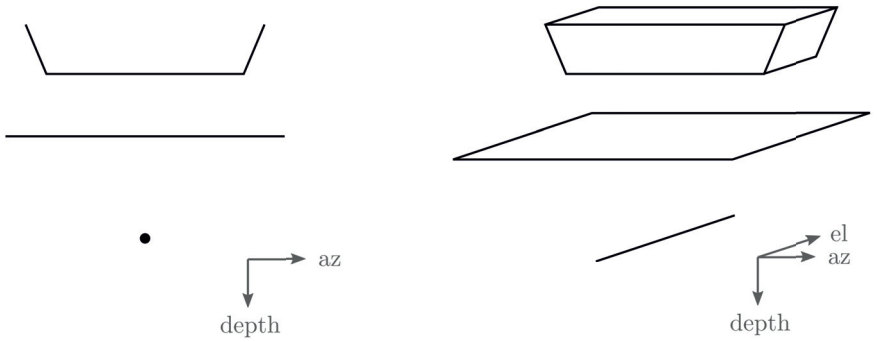


Figure B.1: Phantom setup for (a) simulation and (b) water tank experiment. Transducer on top, a planar reflector in the middle, and a scatterer at the bottom. Radial position of the reflectors variable and interchangable.

## B.2 Method

This section will detail the phantom setup, expected reverberations and their detection, simulation parameters, and experimental methods.

### B.2.1 Phantom setup

Both simulation and experiment are carried out as *in vitro* setups. The simulation tool is constrained to operation in 2D space due to technical limitations. Therefore, a semi-infinite setup containing two reverberators in addition to the transducer was chosen to achieve comparable results from simulation and experiment. In the experiments, a line scatterer is utilized as a point scatterer in the radial-lateral plane and a plane is utilized as planar reflector (see Fig. B.1b). In the simulations, a line reflector in the radial-lateral plane represents the planar reflector, and a point scatterer is utilized as second reverberator (see Fig. B.1a). For clarity, in the following, the terms *plane* is used for the planar reflectors and *point* is used for the point scatterer in the simulation as well as the line scatterer in the experiment. The plane reflector is always parallel to the transducer surface, ignoring the curvature of the elevation lens. Using a line scatterer in the experimental setup also eases the setups' assembly since the line can be easily mounted outside the field of view of the transducer.

A sketch of the setup is given in Fig. B.1. For both setups, the diameter of the point is $200\,\mu$m (corresponding to $0.7\,\lambda_{water}$ at 5 MHz) and its material is chosen to be nylon. The plane is a polypropylen film with thickness of $50\,\mu$m ($0.16\,\lambda_{water}$ at 5 MHz).

The plane and the point can be positioned independently from each other and the transducer. Simulations and experiments are carried out for different combinations

Table B.1: Positions for the reverberators for the simulations and experiments. Given in millimeter distance from the transducer surface.

| Position plane [mm] | 8 | 13 | 6 | 15 | 4 | 17 |
|---|---|---|---|---|---|---|
| Position point [mm] | 13 | 8 | 15 | 6 | 17 | 4 |

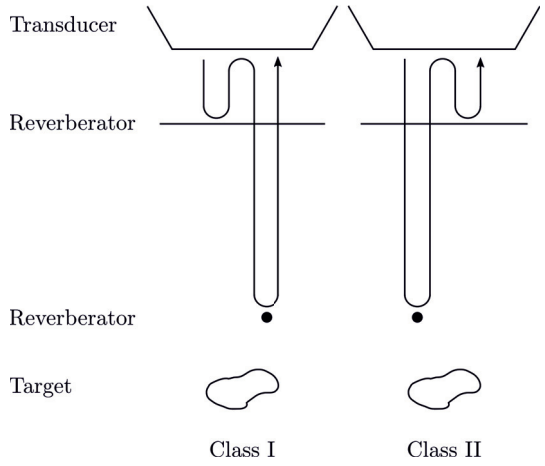


Figure B.2: Classification of reverberations according to [1]. Depicted is the order in which the reverberation hits the different reverberators if a beam is transmitted straight down.

of positions which are given in Table B.1. With these positions, overlapping reverberations in time are avoided in the field of interest and the imaging depth of 21 mm corresponds to the elevational focus of the transducer in water (which will be described in greater detail in Section B.2.3).

### B.2.2 Reverberations

Høilund-Kaupang *et al.* state in [1] that third order reverberations, with the transducer as second reverberator, always act in pairs and show confirming simulations for plane reverberators. Each of these pairs consists of one class I and one class II reverberation, which is illustrated in Fig. B.2. Class I hits the close reverberator first, is then reflected by the transducer surface and the distant reverberator before it returns to the transducer. For class II the order of hitting the reverberators is reversed.

Reflections will in most cases in medical ultrasound result in a reflected pulse with substantially lower pressure than the incoming wave. It is often assumed, that the reflected pulse, due to its low pressure, propagates linearly. Class I and II will thus have different content of nonlinear propagation effects, which only accumulate up to the first reflection [1].

Class I and II arrive at the transducer concurrently and are not separable in beam-

formed signals. With the chosen phantom setup and utilizing channel data recording before beamforming it is possible to show the existence of both reverberation classes:

The specular reflection on a plane will preserve the waveform, *i.e.,* a focused beam from the transducer will after reflection still have the same curvature towards the focal point, but propagates in the opposite direction. Dual specular reflection, *i.e.,* on a plane in depth $z_1$ and the transducer surface, will cause the wave to propagate in the original direction but as if the transducer was located at $-2z_1$. As illustrated in Fig. B.3, the same happens to the scattered, circular wave originating from the point scatterer in depth $z_3$. The first-order echo and the class I reverberation being received by the transducer will have the radius $r_{\mathrm{I}} = z_3$ (Fig. B.3a). However, they will arrive at different points in time. After dual specular reflection, as is the case for the class II reverberation, the wave will resemble a circular shape with radius $r_{\mathrm{II}} = z_3 + 2z_1$ (Fig. B.3b). Thus, the sum of class I and II consists of a superposition of two circular waves with radius $r_{\mathrm{I}}$ and $r_{\mathrm{II}}$ where the centers of both waves arrive concurrently (Fig. B.3c). If channel data is recorded this information is preserved.

Utilizing different transmit and receive apertures it is possible to split the reverberation pair and receive either class I or class II. Fig. B.4 illustrates the approach: To isolate class I, an oblique beam is transmitted such that the point target is located outside of its main lobe and little first order echo is reflected. The location of the point target is chosen such that the second order reverberation hits it, and a class I reverberation is generated. The receive aperture is centered around the lateral position of the point target. For isolation of class II, the transmit beam is directed at the point target. The second order reverberation misses the point and only class II is generated. The receive aperture is placed at the same location as before. The two classes were not separable in an experiment if the same transmit and receive aperture would be applied. In a simulation it is possible to alter the medium during propagation and remove one of the reverberators at suitable points in time, but this was not done here.

### B.2.3 Experiment

To create a phantom as described in B.2.2 in practice, a polypropylen film is utilized as planar reflector and a nylon wire as point scatterer. This was combined and immersed in a watertank. The transducer was mounted on a translation robot to be able to precisely control the radial, lateral and elevational position relative to the phantom. The distance between transducer and phantom was measured using the clinical user interface of the scanner.

A digital acquisition extension (DAQ, [5]) attached to a SonixMDP research scanner (both Ultrasonix Medical Corporation[2]) was utilized for recording the experimental data. The DAQ allows to record pre-beamformed channel data on all the 128 channels of the system. It was configured to record with 40 MHz sampling frequency and 12 Bit dynamic range. Time gain compensation (TGC) was disabled and a fixed amplification used instead.

As transducer a L9-4/38, a 128 element linear array with a center frequency of 5MHz and a 300 $\mu$m pitch was used. Its footprint is 6 mm x 38 mm with a fixed

[2]Richmond, BC, Canada, `http://www.ultrasonix.com`

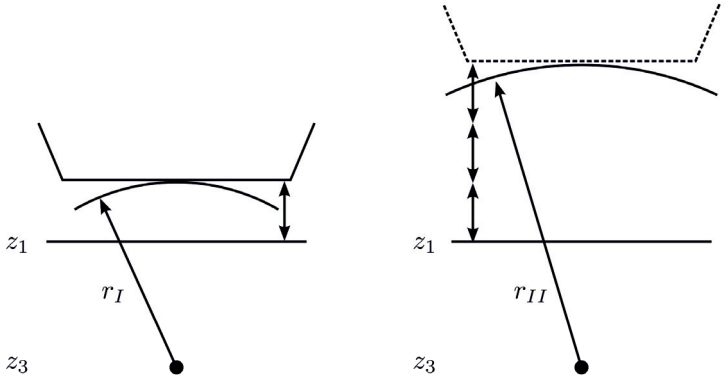


(a) Class I

(b) Class II

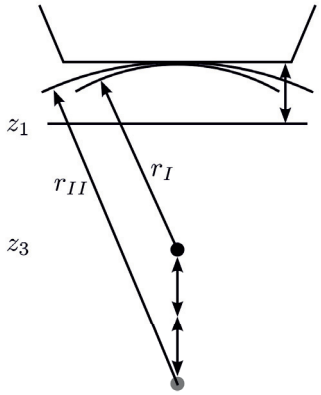


(c) Class I & II

Figure B.3: Radii of class I and II reverberations. A transducer (on top) receives the multiply reflected echoes (circular waves) of a plane reverberator in depth $z_1$ and a point target in $z_3$. The class II echo in (b) is reflected on the plane and transducer surface before receiving. Therefore a virtual transducer position of $-2z_1$ can be assumed. (c) visualizes the class I and II component arriving at the same time with different radii.

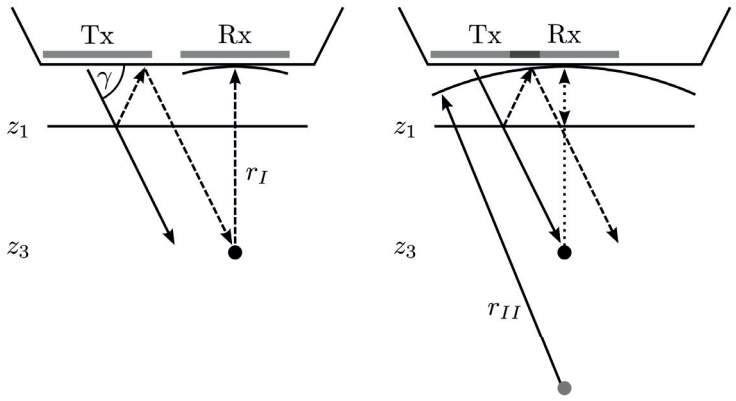


(a) Class I (b) Class II

Figure B.4: Isolation of class I and II in case of oblique transmit and separate receive aperture. Dashed line: path of class I reverberation, dotted line: path of class I reverberation.

elevation focus at 19 mm depth. The elevation focus of ultrasound transducers is normally designed for transmit in tissue with an average sound velocity of 1540 m/s. According to McKeighen [6], the radius of curvature (ROC) of the elevation lens can be determined with the following equation:

$$ROC = F\frac{c_m - c_l}{c_l} \tag{B.1}$$

Where F is the desired focal depth, and $c_m$, $c_l$ the sound velocities in the medium and the lens, respectively. Assuming 1000 m/s for $c_l$, the ROC can be computed. Re-inserting it and solving the equation for F using $c_m = 1490$m/s yields an elevational focus of about 21 mm for propagation in water. The (electronic) azimuth focus was also set to 21 mm.

The transmit aperture consisted of 24 elements, which corresponds to a f-number $F_\# = 2.9$. The element excitation was a rectangular, three half-cycle pulse at 5 MHz center frequency with an amplitude of 47 V. All 128 channels were recorded on receive, however only 64 around the center of the aperture were used for analysis.

One B-Mode frame of 128 lines for straight and another one for oblique transmit was acquired for each of the reverberator position combinations given in Tab. B.1.

### B.2.4 Simulation

Most of the ultrasound artifacts can be computed analytically, numerically with application of the spatial impulse response (*f.ex.,* Field II), or with forward simulations (*f.ex.,* Abersim). Often an assumption of linear propagation is required. Multiple

scattering, reflections and reverberations require simulation tools that handle both (nonlinear) forward and back propagation simultaneously. Such simulation programs integrate a set of model equations in time. Their approach to spatial differentiation is different. Examples of such simulation programs are a finite difference based method of Pinton *et al.* [7], a finite element method (FEM) of Wojcik *et al.* [8], and a spectral element method (SEM) code by Høilund-Kaupang and Angelsen [1]. The latter is used for the simulations presented in this article.

The model equations are the second order accurate equations of acoustics accounting for nonlinear elasticity of the medium and frequency dependent absorption. Finite and spectral element methods are both based on weak formulations of these differential equations. The differences between the two methods are the order of the trial functions used for approximation. Whereas finite element methods use low order polynomials, spectral element methods use higher order (orthogonal) Legendre polynomials. Spectral elements are also used in studies for (linear) seismological wave propagation [9]. The integration scheme used in the SEM code is the leap frog scheme. This integration scheme is also implemented in simulation tools for linear acoustic wave propagation [10, 11]. The code used in this article is verified with analytic results for the absorption model and nonlinear propagation in a plane wave situation. Two-dimensional propagation is compared with the results from a forward propagation simulation tool, Abersim [1, 12–14]

The polynomial order used in this article is 16, and the sampling frequency in time is 100 MHz. The lateral simulation domain size is adjusted to the transmit and receive aperture and is 21.8 mm (66 transducer elements) for the straight transmit and 25.8 mm (82 transducer elements) wide for the oblique transmit case.

The transmit parameters are chosen according to the experimental setup. The active transmit aperture has the same size as 24 elements on the transducer, however no transducer elements, kerf between elements or effective element size are simulated. Also the focusing delay is not quantized in transducer elements, but computed for each simulation node. The beam is focused at 21 mm depth. The transmit pulse is defined as pressure pulse on the surface of the transducer. A gaussian pulse with 50% bandwidth and 500 kPa amplitude is chosen. The transducer is modeled as a totally reflecting surface.

Table B.2 lists the material parameters for the different components of the simulation phantom. Each material is defined through its speed of sound $c$, its density $\rho$, the nonlinearity parameter $\beta_n$ and an attenuation $\alpha f^\beta$. Linear propagation is assumed within the plane and the point.

After computing the result on all nodes, artificial transducer element signals were generated by averaging the node signals over the pitch of 300 $\mu$m.

### B.2.5 Analysis

The channel data from the experiment and the artificial channel data is analysed with the same code.

To measure the radius of the received wave, the coherence factor is utilized. The coherence factor (CF) was presented as metric for focusing quality by Mallart and

Table B.2: Material parameters for the different components of the simulation phantom.

| Material | Part | $c$ [m/s] | $\rho$ [kg/m$^3$] | $\beta_n$ | $\alpha$ [dB/cm/MHz] | $\beta$ |
|---|---|---|---|---|---|---|
| Polypropylen | Plane | 2740 | 880 | 0 | 1.02 | 1 |
| Nylon | Point | 2600 | 1120 | 0 | 0.58 | 1 |
| Water (20°C) | Medium | 1482 | 998 | 3.48 | $2.17 \cdot 10^{-3}$ | 2 |

Fink [15]. It has since been used as a measure for image quality and in adaptive beamforming [16, 17]. Let $x_m[n]$ be the $n$-th sample in time of the $m$-th channel signal of a dataset acquired with a linear array. The CF for a number of $M$ channels is then defined as:

$$\mathrm{CF}[n] = \frac{\left|\sum_{m=0}^{M-1} x_m[n]\right|^2}{M \sum_{m=0}^{M-1} |x_m[n]|^2} \tag{B.2}$$

The coherent sum in the numerator is divided by the incoherent sum in the denominator and scaled for the number of channels. While (destructive) interference is possible in the coherent sum it is not possible in the incoherent sum. Thus, the numerator will always be less or equal the denominator and the CF is between 0 and 1.

If $x$ is a signal with proper focus (and steering) delays towards a focus point (depth $z_f$, steering angle $\gamma$) applied, a higher CF will indicate more accurate focusing. For the case of a wave originating from a point scatterer, the curvature of the wave fits to the applied focus delays. In this way, the CF can be utilized to determine the propagation distance of a wave from a point scatterer to the transducer.

To determine the radii of the incoming reverberation, the recorded channel data will subsequently be corrected for a range of focusing delays with foci $(z_f, 0)$ such that a matrix $\mathrm{CF}[z_f, n]$ of coherence factors can be computed. An sub-aperture of 26 channels in the center of the aperture will be excluded from the computation. The CF is thus computed on two sub-apertures with 18 channels each, laterally symmetric on both sides of the beam axis (see Fig. B.6d). This avoids computation on areas where echoes overlap, which in turn may impair the position and amplitude of the CF maxima along depth (see Section B.4).

Finally, to separate the different echoes and reverberations from each other, windows in time are applied and a weighted average is computed over the window length. For a window $k = [n_1, n_2]$ we get a vector of coherence factors for different focus points:

$$\mathrm{CF}_k[z_f] = \sum_{n=n_1}^{n_2} \mathrm{CF}[z_f, n] w[n - n_1] \tag{B.3}$$

where $w[l]$ is a weighting function. A Hann window (1.2 $\mu$s long), is used throughout this article.

For straight transmit, $\mathrm{CF}_k$ of the window around the sum of the reverberation pair should exhibit two maxima, one at $r_\mathrm{I}$ for class I and another at $r_\mathrm{II}$ for class II.

For oblique transmit, based on the amplitude of the echoes, the two transmit lines are identified where the point target is hit centrally, one each for class I and II respectively. Then, the same analysis as above is carried out. In the results, $CF_k$ should just show one of the two maxima which are present for the straight transmit.

For the simulation data an assessment of the nonlinear signal content will also be carried out. First, class I and class II signals are obtained from the oblique transmit case. These signals are beamformed with focus of the expected radius and then filtered in a fundamental and harmonic band, each with 50% bandwidth. The maximum amplitudes of these bands are compared.

For the experiments, the data showed no measurable increase in harmonic signal, not only in the reverberation signals but also first order echoes, thus the analysis was not conducted. This is attributed to the low bandwidth of the transducer and the low maximum transmit voltage of the Ultrasonix scanner.

## B.3 Results

Both simulations and experiments were carried out on the same combinations of positions of the two reverberators. The combinations are given in Tab. B.1. The results section is divided in the straight and the oblique transmit setting.

### B.3.1 Straight transmit

As described above, pre beamformed channel data was either acquired or computed. Fig. B.5 displays the whole datasets for two geometries. In panel (a) and (b) the plane and the point are located at 8 mm and 13 mm depth, respectively. The different signals are labelled in white for convenience. The first signal (label 0) from the top consists of the edge waves of the transmit pulse and additional noise for the experimental case. Subsequently, the first order echoes of the plane (1) and point (2) are received. The experimental case also features unexpected horizontal lines at the positions of the amplitude maxima of these echoes. The fourth signal (3) is the first reverberation which has travelled two times between transducer and plane (plane-transducer-plane). In 21 mm depth (simulation) and 21.8 mm depth (experiment) the class I and II reverberation can be observed (4). These two reverberations in the experiment consist of a weak (3a, 4a) and a strong echo (3b, 4b) resembling each other. The last visible reverberation (5) has travelled two times between transducer and point (point-transducer-point).

For panel (c) and (d) of Fig. B.5, which present another geometry with the plane and the point in 15 mm and 6 mm, respectively, the signals from top to bottom are: Transmit signal (0), First order point echo (1), third order point-transducer-point (2), first order plane echo (3), class I and II reverberation (4) and the plane-point-plane reverberation (5). The two last mentioned echoes overlap for the experimental result while they are clearly separated in the simulation.

Fig. B.6 displays an enlarged plot of the class I/II reverberation for both experimental and simulation results. Dotted lines mark the expected radii, while dashed and

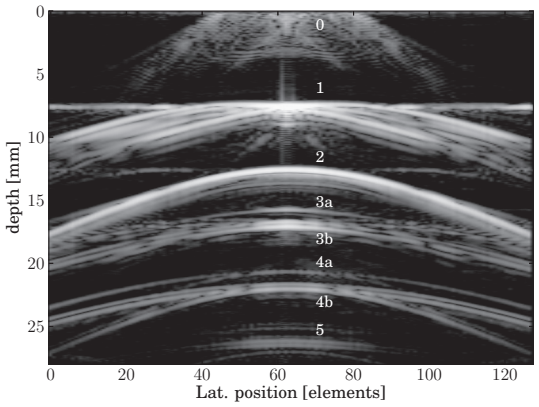


(a) plane: 8 mm, point: 13 mm (Experiment)

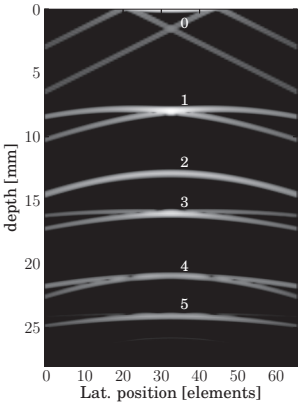


(b) plane: 8 mm, point: 13 mm (Simulation)

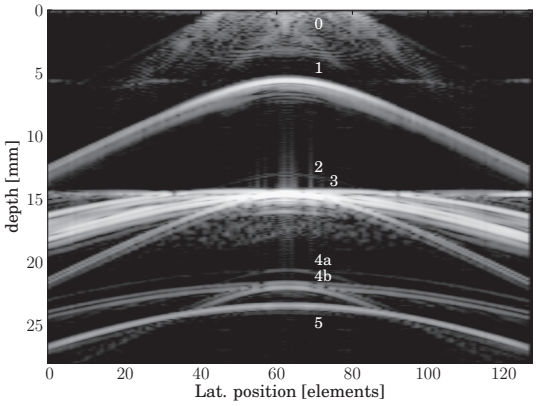


(c) plane: 15 mm, point: 6 mm (Experiment)

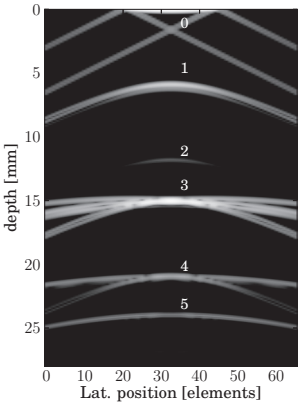


(d) plane: 15 mm, point: 6 mm (Simulation)

Figure B.5: Channel data, converted to analytic value for display. Left column experimental data, right column simulation data. Aspect ratio maintained, lateral position in (virtual) transducer elements with a pitch of 0.3 mm, the images are visualized with a dynamic range of 60 dB. Visible signals in (a) and (b) from top to bottom with their respective labels (white numbers in the images): 0: Transmit pulse, 1: first order echo plane, 2: first order echo point, 3: plane-transducer-plane, 4: class I and II, 5: point-transducer-point. (c), (d): 0: Transmit signal, 1: first order point, 2: point-transducer-point (weak in the experiment), 3: first order plane, 4: class I and II, 5: plane-point-plane.

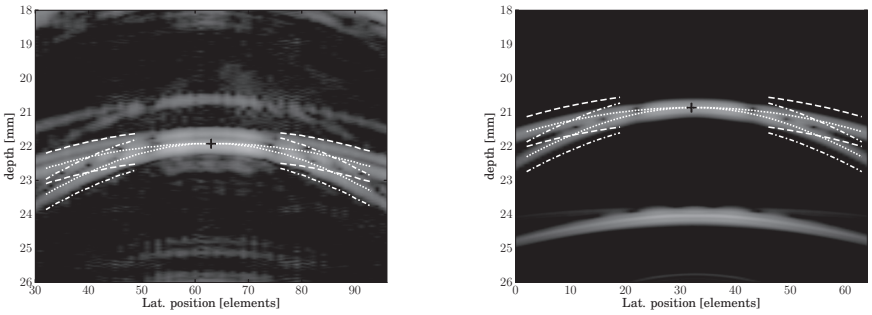


(a) Depth plane: 8 mm, point: 13 mm

(b) Depth plane: 8 mm, point: 13 mm

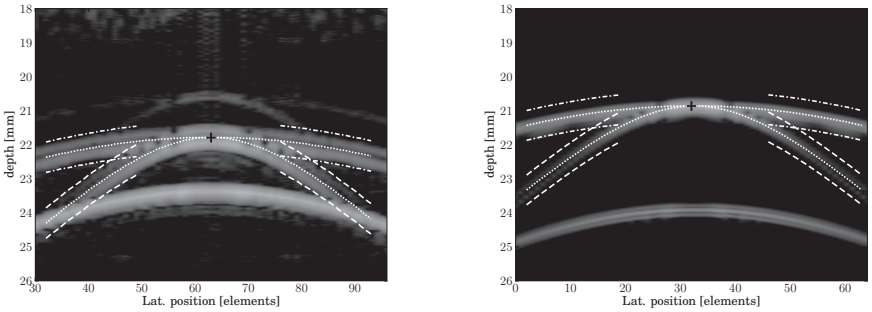


(c) Depth plane: 15 mm, point: 6 mm

(d) Depth plane: 15 mm, point: 6 mm

Figure B.6: Class I and II reverberations with computation windows (class I dash-dotted line, class II dashed line) and applied focus delays for expected radii (dotted lines). Lateral beam axis center marked with cross. Left column experimental data, right column simulation data. Aspect ratio not maintained.

dash-dotted lines show the computation window for the coherence factor in both length and width. Note the different arrival time of the reverberations in the simulation and experiment.

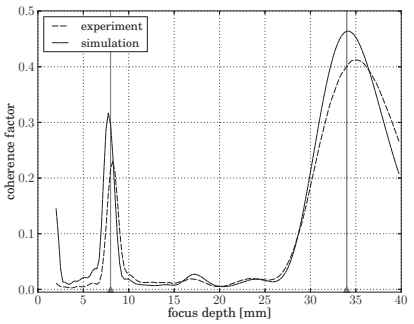


(a) Depth plane: 13 mm, point: 8 mm

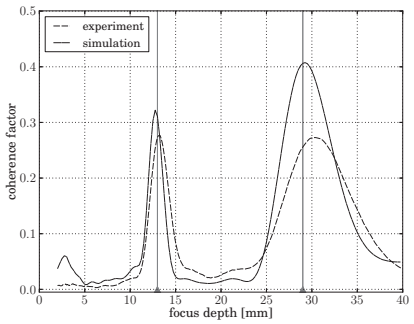


(b) Depth plane: 8 mm, point: 13 mm

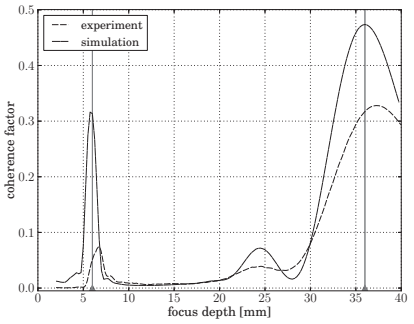


(c) Depth plane: 15 mm, point: 6 mm

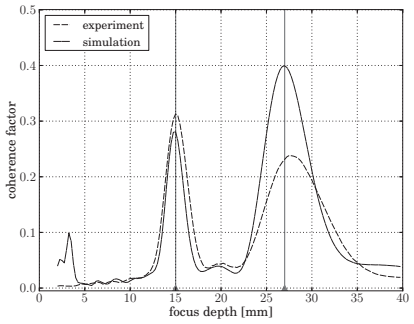


(d) Depth plane: 6 mm, point: 15 mm

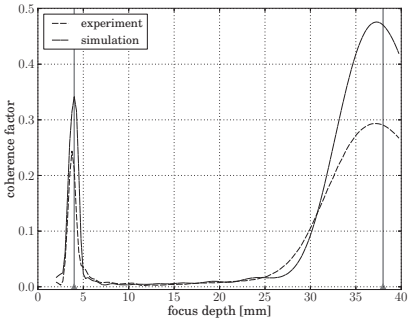


(e) Depth plane: 17 mm, point: 4 mm

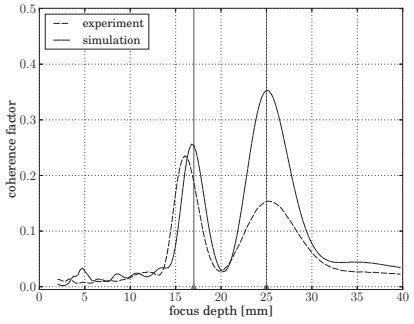


(f) Depth plane: 4 mm, point: 17 mm

Figure B.7: Coherence factor vs. applied beamforming focus depth for both simulation (solid line) and experiment (dashed line) of *straight* transmit. The expected position of the maxima is marked with gray vertical lines and triangles on the x-axis.

The computed coherence factor for the different geometries is depicted in Fig. B.7. Despite the plot in (e) all simulation results match very well with the expected radii. The experimental results show some variations. The first maximum of the coherence factor of the experiment (15 mm plane) in panel (c) is with 0.7 comparably lower as for the first maxima in the other experiments which range between 0.2 and 0.3. There are differences between the expected and the determined position of the second maximum for five of six geometries.

### B.3.2 Oblique transmit

Figure B.8 displays the coherence factor results for the oblique transmit experiment and simulation. The result for the straight transmit is given as a reference. While the coherence factor has a maximum for both expected radii in straight transmit, it has, as expected, only one maximum for the oblique transmit. The position of plane relative to the position of the point determines if the class I or class II wave has the smaller radius. This is reflected in the measurements of geometries with swapped reverberator position where also the class featuring the first maximum is swapped. For example in panel (a), class I is attributed the maximum around 35 mm while in panel (b) it is attributed the maximum at 8 mm.

Also for the oblique transmit case the simulation and experiment data matches well with the expected radii. An exception to this is panel B.8e where the class II reverberation in the simulation has two maxima, one as expected at 4 mm, and another at 29 mm.

### B.3.3 Harmonic propagation

The second harmonic content of the reverberations for the oblique transmit case is assessed for the simulation data. The results are given in Tab. B.3. For all geometries class II shows between 6 and 11 dB more harmonic signal than class I. The difference is increasing for increasing distance between the two reverberators.

Table B.3: Amplitude of the class I and II reverberations in the second harmonic band of the simulations, relative to the fundamental band in dB. Positions of plane and point given in mm.

| Position plane [mm] | 8 | 13 | 6 | 15 | 4 | 17 |
|---|---|---|---|---|---|---|
| Position point [mm] | 13 | 8 | 15 | 6 | 17 | 4 |
| Class I [dB] | -23 | -26 | -23 | -25 | -24 | -29 |
| Class II [dB] | -17 | -20 | -16 | -19 | -16 | -18 |
| Class I vs Class II [dB] | -6 | -6 | -7 | -6 | -8 | -11 |

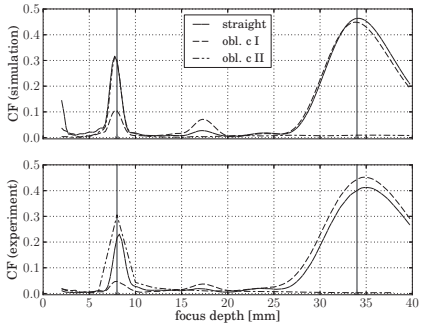


(a) Depth plane: 13 mm, point: 8 mm

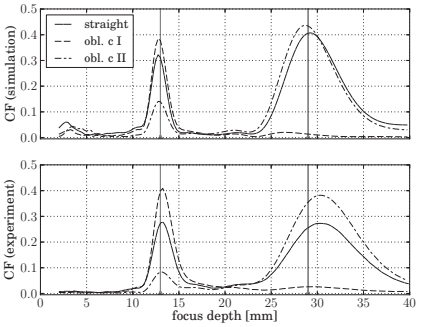


(b) Depth plane: 8 mm, point: 13 mm

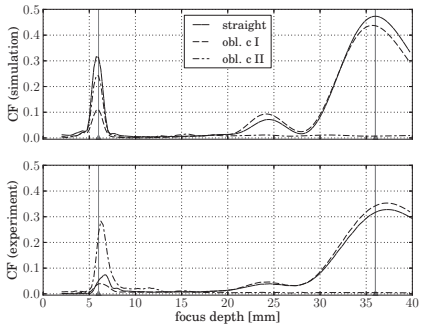


(c) Depth plane: 15 mm, point: 6 mm

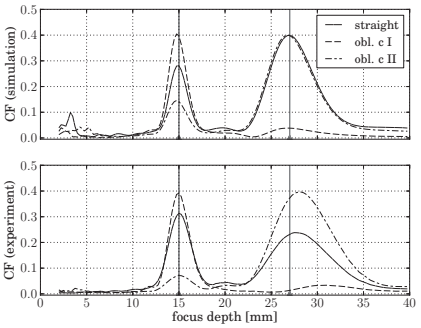


(d) Depth plane: 6 mm, point: 15 mm

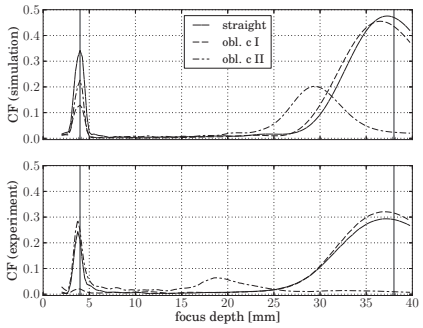


(e) Depth plane: 17 mm, point: 4 mm

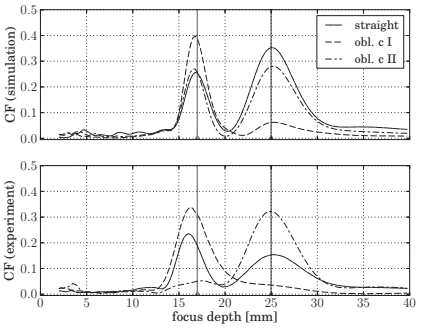


(f) Depth plane: 4 mm, point: 17 mm

Figure B.8: CF vs. beamforming focus depth for *straight* (solid) and *oblique* transmit analyzed for class I (dashed) and class II (dash-dotted) reverberations. Each panel has two subplots displaying simulation results in the upper and experimental results in the lower one. The expected position of the maxima is marked with gray vertical lines and triangles on the x-axis.

## B.4 Discussion

There are deviations in the arrival time of the different echoes between experiment and simulation. The distance between the transducer and the first target was measured with the scanner in the clinical modus, but the data was recorded with the DAQ which is externally triggered. So a constant delay of all echoes might be attributed to the different trigger and recording modalities. Looking at the first order echoes there are smaller deviations of up to half a millimeter, corresponding to about 0.7 $\mu$s, while the distances between the plane and point echoes are precisely as expected.

Most reverberations consist of a weak echo which arrives within a $\pm 0.5$ mm margin around where they are expected, however the main echo is delayed. For example in Fig. B.6a and B.6b the reverberation is expected to arrive at 21 mm. The echo of the plane target (1), point target(2), the weak reverberation echo (4a), and the main reverberation echo (4b) are observed at 7.6 mm, 12.6 mm, 20.6 mm and 21.8 mm, respectively. Using the best matching radius of the point echo as a reference for the accurate position relative to the transducer, from Fig. B.7b a radius of 13.2 mm would result in a general offset of 0.6 mm. So the true position of the plane and point target are at $7.6 + 0.6 = 8.2$ mm and 13.2 mm, respectively. Thus the reverberation should be observed at 21.4 mm. The weak echo is then 0.2 mm too early, but the reverberation main echo is then at 22.4 mm, so there is a 1 mm difference which is 1.3 $\mu$s in time or 6.7$\lambda$with respect to the imaging pulse.

A hypothesis to explain this delay is that the weak echo occurs when the returning pulse hits the transducer lens, while the main echo is caused by the interface between matching layers and the piezo-crystal: With the known probe focus of 19 mm in tissue the lens, again assuming 1000 m/s as sound velocity, is at its thickest point at least 2.74$\lambda$, including an assumed 0.1 mm carrier. Together with two additional matching layers of 0.25$\lambda$ each, two ways, would result in a delay of 6.5$\lambda$which is in the order of the observed delay.

The reverberation, which overlaps with the class I/II reverberation in Fig. B.6c, labelled with '5', is an exception to this since it is the reverberation which has the point as second and the plane as second and third reflector and arrives therefore as and where expected.

In the experimental channel data in the depth of strong echoes a horizontal line can be seen. This is thought to be an artifact of cross talk in the receive electronics.

The amplitude of reverberations is decreasing faster in terms of visible number of reflections in the experiments than in the simulation. Since the transducer is modeled as a totally reflecting hard wall this is expected.

Looking at the coherence factor plots in Fig. B.7 and B.8, the expected radii of the class I and II reverberation can be observed in both simulation and experiment and for both the straight and the oblique transmit setting. The experimental CF is lower than the simulation CF which is attributed to noise in the recording and ringing in the transducer (as can be seen on the transmit pulse and the strong echoes).

The position of the CF maxima in the simulation results for the straight transmit (Fig. B.7) are located where they are expected from theory, with minor deviations. Each curve shows two maxima, one each for the class I and II. The experimental data

also supports that, however there are two things to comment.

First, the low CF maximum at 7 mm depth in Fig. B.7c is much lower than its simulation counterpart. This is caused by the overlapping reverberations which were described above (see Fig. B.6c). This illustrates also why the CF is computed on the two lateral areas, but not on the central part where the reverberations overlap.

Second, in four of six experiments the second maximum deviates from the expected radius (experiments with plane in 8, 13, 15, 6 mm depth) with between 0.8 and 1 mm. This also is attributed to the propagation delay for reverberations which are reflected from the transducer surface. The experiment with plane in 4 mm depth should probably included here as the transducer might have been misaligned with the phantom, resulting in lower radii both for the first and second maximum.

In both simulation and experiment with the plane in 17 mm (Fig. B.7e) the radius for second maximum is lower than expected with unknown cause.

For the oblique transmit setting the results show that class I and II can be separated from each other. One plot will be further commented.

In Fig. B.8e, the simulation with a plane in 17 mm depth, the analysis which is supposed to isolate the class II reverberation has a second maximum at 29 mm depth. Analysis of the sound field over time showed, that this is a weak (-40dB), but coherent reverberation where the first order echo is caused by the second edge wave of the transmit pulse which hits the point target. In addition the class I reverberation is even further off the expected radius. Analyzing the full sound field revealed that the reverberation arrives synchronous with an edge wave reverberation which might explain the deviation.

The harmonic content in the class II component was as expected higher than in the class I component (B.3). A large distance between the reverberators also implies a larger difference in harmonic content between class I and II. This is also expected since a large distance is achieved when the reverberators are placed closer to the transducer and the target. The harmonic content of class I is for all cases at least 6dB below its class II counterpart. However, this cannot be directly transferred to expected suppression of the two components in THI since the receive beam is not applied as it would in a normal imaging situation. This would affect the total amplitude of each component. Nevertheless, it shows that THI will not work equally well on the different parts of a reverberation pair and will be less for suppression of the class II component.

## B.5 Conclusion

These simulation and experimental results support the theory presented in [1] which predicts the existence of a reciprocal pair of reverberations. This is true as long as the transmit and receive beam is the same. If the beams deviate from each other, the pair may be splitted as was shown for the oblique transmit setting. The reverberation simulations were in good agreement with the water tank experiments which is also a validation of the applied simulation tool. The approximation to represent the transducer in simulations with a totally reflecting plane is working well regarding to reproduce the same type of reverberations but fails to reproduce the precise arrival

times.

## Acknowledgement

Tonni Franke Johansen, Svein-Erik Måsøy and Thor Andreas Tangen are acknowledged for fruitful discussions and practical support during this work.

## Bibliography

[1] H. Høilund-Kaupang, "Models and methods for investigation of reverberations in nonlinear ultrasound imaging," Ph.D. dissertation, Norges teknisk-naturvitenskapelige universitet, 2011. [Online]. Available: http://ntnu.diva-portal.org/smash/record.jsf?pid=diva2:479070

[2] M. Averkiou, D. Roundhill, and J. Powers, "A new imaging technique based on the nonlinear properties of tissues," in *Proc IEEE Ultrason Symp*, vol. 2, Oct. 1997, pp. 1561 –1566 vol.2.

[3] B. Ward, A. C. Baker, and V. F. Humphrey, "Nonlinear propagation applied to the improvement of resolution in diagnostic medical ultrasound," *J Acoust Soc Am*, vol. 101, no. 1, pp. 143–154, 1997.

[4] S. Choudhry, B. Gorman, J. W. Charboneau, D. J. Tradup, R. J. Beck, J. M. Kofler, and D. S. Groth, "Comparison of tissue harmonic imaging with conventional US in abdominal disease," *Radiographics*, vol. 20, no. 4, pp. 1127–1135, Jul. 2000.

[5] C. C. Cheung, A. C. Yu, N. Salimi, B. Y. Yiu, I. K. Tsang, B. Kerby, R. Z. Azar, and K. Dickie, "Multi-channel pre-beamformed data acquisition system for research on advanced ultrasound imaging methods," *IEEE Trans Ultrason Ferroelectr Freq Control*, vol. 59, no. 2, pp. 243–253, Feb. 2012.

[6] R. E. McKeighen, "Design guidelines for medical ultrasonic arrays," *Proceedings of SPIE*, vol. 3341, no. 1, pp. 2–18, May 1998. [Online]. Available: http://spiedigitallibrary.org/proceedings/resource/2/psisdg/3341/1/2_1

[7] G. Pinton, J. Dahl, S. Rosenzweig, and G. Trahey, "A heterogeneous nonlinear attenuating full- wave model of ultrasound," *IEEE Trans Ultrason Ferroelectr Freq Control*, vol. 56, no. 3, pp. 474 –488, Mar. 2009.

[8] G. Wojcik, J. Mould, S. Ayter, and L. Carcione, "A study of second harmonic generation by focused medical transducer pulses," in *Proc IEEE Ultrason Symp*, vol. 2, 1998, pp. 1583 –1588 vol.2.

[9] D. Komatitsch and J. Tromp, "Introduction to the spectral element method for three-dimensional seismic wave propagation," *Geophysical Journal International*, vol. 139, no. 3, p. 806–822, 1999.

[10] X. Yuan, D. Borup, J. Wiskin, M. Berggren, and S. Johnson, "Simulation of acoustic wave propagation in dispersive media with relaxation losses by using FDTD method with PML absorbing boundary condition," *IEEE Trans Ultrason Ferroelectr Freq Control*, vol. 46, no. 1, pp. 14 –23, Jan. 1999.

[11] M. Tabei, T. D. Mast, and R. C. Waag, "A k-space method for coupled first-order acoustic propagation equations," *The Journal of the Acoustical Society of America*, vol. 111, no. 1, pp. 53–63, 2002.

[12] T. Varslot and G. Taraldsen, "Computer simulation of forward wave propagation in soft tissue," *IEEE Trans Ultrason Ferroelectr Freq Control*, vol. 52, no. 9, pp. 1473 –1482, Sep. 2005.

[13] T. Varslot and S.-E. Måsøy, "Forward propagation of acoustic pressure pulses in 3D soft biological tissue," *Modeling, Identification and Control*, vol. 27, no. 3, pp. 181–200, 2006.

[14] M. Frijlink, H. Kaupang, T. Varslot, and S.-E. Masoy, "Abersim: A simulation program for 3D nonlinear acoustic wave propagation for arbitrary pulses and arbitrary transducer geometries," in *Proc IEEE Ultrason Symp*, Nov. 2008, pp. 1282 –1285.

[15] R. Mallart and M. Fink, "Adaptive focusing in scattering media through sound-speed inhomogeneities: The van cittert zernike approach and focusing criterion," *The Journal of the Acoustical Society of America*, vol. 96, no. 6, pp. 3721–3732, 1994.

[16] K. W. Hollman, K. W. Rigby, and M. O'Donnell, "Coherence factor of speckle from a multi-row probe," in *Proc IEEE Ultrason Symp*, vol. 2. IEEE, 1999, pp. 1257–1260 vol.2.

[17] C. I. Nilsen and S. Holm, "Wiener beamforming and the coherence factor in ultrasound imaging," *IEEE Trans Ultrason Ferroelectr Freq Control*, vol. 57, no. 6, pp. 1329–1346, Jun. 2010.

Paper C

# Methods for Reverberation Suppression Utilizing Dual Frequency Band Imaging

Jochen M. Rau[1], Thor Andreas Tangen[2], Svein-Erik Måsøy[1], Rune Hansen[1,3] and Bjørn Angelsen[1]
[1]Department of Circulation and Medical Imaging, NTNU, Trondheim, Norway,
[2]Department of Engineering Cybernetics, NTNU, Trondheim, Norway,
[3]SINTEF Society and Health, Trondheim Norway

**Abstract**

Reverberations impair the contrast resolution of diagnostic ultrasound images. Tissue harmonic imaging is a common method to reduce these artifacts but does not remove all reverberations.

Dual frequency band imaging (DBI), utilizing a low frequency pulse which manipulates propagation of the high frequency imaging pulse, has been proposed earlier for reverberation suppression.

This article adds two different methods for reverberation suppression with DBI, the delay corrected subtraction (DCS) and the first order content weighting (FOCW) method. Both methods utilize the propagation delay of the imaging pulse of two transmissions with alternating manipulation pressure to extract information about its depth of first scattering. FOCW further utilizes this information to estimate the content of first order scattering in the received signal.

Initial evaluation is presented where both methods are applied to simulated and *in vivo* data. Both methods yield visual and measurable substantial improvement in image contrast. Comparing DCS with FOCW, DCS produces sharper images and retains more details while FOCW achieves best suppression levels and thus highest image contrast. The measured improvement in contrast ranges from 8 to 27 dB for DCS and from 4 dB up to the dynamic range for FOCW.

This article is submitted to the Journal of the Acoustical Society of America

## C.1 Introduction

Reverberations are a known artifact in medical ultrasound imaging [1–3]. They occur if the transmitted pressure pulse is reflected more than once before it is received by the transducer. The reflection may happen between tissue layers or tissue layers and the transducer or an arbitrary combination of both. The length of the propagation path of the reverberation determines the image depth where it occurs together with the first order echo from that depth. Reverberations may be perceived in different ways. They may occur as any kind of noise ranging from discrete replica of proximal structures or bright tails to haze- or cloud-like artifacts covering parts of the image, usually stronger after strong reflectors and decaying in hypoechoic regions.

Today, Tissue Harmonic Imaging (THI) is a common method for reverberation suppression in clinical practice. THI utilizes the nonlinear propagation of sound in tissue [4–6]. Nonlinear propagation is an accumulative pressure dependent phenomenon which is more pronounced for higher amplitudes. A common assumption in diagnostic imaging is therefore that the pressure drops after the first reflection to levels where linear propagation can be assumed [7]. As the pulse propagates into the tissue more and more energy is transferred from the fundamental to the harmonic imaging bands. Thus the harmonic imaging signal is weak close to the transducer and increases with depth, competing with absorption which is greater for higher frequencies. This yields a reduction in reverberations if the first reflection happens close to the transducer, as these reflections will in their further propagation not accumulate more harmonic energy, and thus be filtered out [7–9]. However, reverberations with the first reflection close to the imaging target exhibit nearly the same level of harmonic signal content as the signal from the target itself and will therefore still be present in the final image [10]. THI is widely used within cardiac and abdominal imaging, but there remain applications where its clinical impact is less significant, *e.g.,* in carotid artery imaging [11].

Recently, novel methods for reverberation suppression have been presented. These are short-lag spatial coherence imaging [12], a method utilizing acoustic radiation force impulse (ARFI) imaging [13], and an application of dual frequency band imaging (DBI) [14–16]. However, none of these methods has reached clinical practice, yet.

Dual frequency band imaging (DBI) is as THI based on the nonlinear propagation of sound waves in tissue. However, while THI utilizes the self-distortion of the travelling wave, in DBI nonlinear propagation is systematically generated by a manipulation pulse which is sent synchronously to the imaging pulse. The imaging pulse together with the manipulation pulse will be called a pulse complex. Such a pulse complex, consisting of a high frequency (HF) imaging pulse and a low frequency (LF) manipulation pulse, is displayed in Fig. C.1. For the application which is presented in this article, the frequency relation HF:LF is about 10:1.

DBI was, as harmonic imaging [17], originally developed as method for contrast agent imaging [18–20] and is also known under the name Radial Modulation Imaging [19] or SURF imaging [21]. Further applications have been developed since, one being reverberation suppression. Common to most of the DBI applications is a multi-transmit scheme consisting of several pulse complexes per line in the final image.

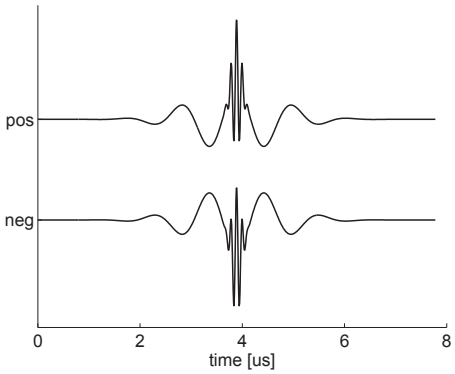


Figure C.1: DBI pulse complexes consisting of a low frequency manipulation pulse and a high frequency imaging pulse with $f_{\mathrm{HF}}/f_{\mathrm{LF}} = 10$. Upper panel positive, lower panel negative manipulation.

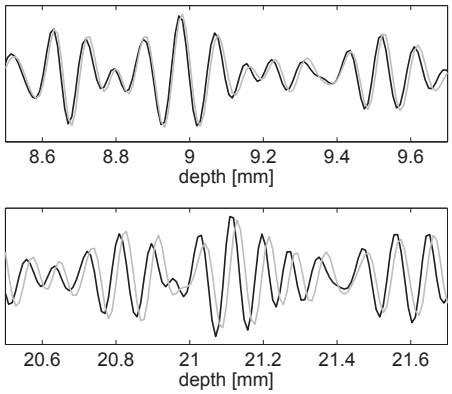


Figure C.2: Simulated DBI RF signals for a shallow (9 mm) and a deep (21 mm) location. Positively (black) and negatively (gray) manipulated imaging signal. Note the delay increase.

Often, two complexes with inverse manipulation, as depicted in Fig. C.1, are utilized.

In this article two novel methods for reverberation suppression with dual frequency band imaging are presented together with an initial evaluation.

## C.2 Theory

A thorough derivation and discussion of the nonlinear phenomena occurring in DBI, as nonlinear propagation, scattering, and artifacts, is given in [15, 22]. In DBI reverberation suppression the desired effect of the manipulation wave is a manipulation of the propagation velocity $c$ (Eq. 9 in [22]):

$$c = c_0\sqrt{1 + 2\beta_{\mathrm{n}}\kappa p - 2\beta_{\mathrm{n}}^2(\kappa p)^2} \approx c_0(1 + \beta_{\mathrm{n}}\kappa p)\,. \tag{C.1}$$

Where $c_0$, $\beta_{\mathrm{n}}$, $\kappa$, $p$ are the propagation velocity without manipulation, the nonlinearity parameter, the bulk compressibility of the medium, and the manipulation pressure experienced by the imaging pulse, respectively. The approximation is a first order Taylor expansion assuming $\kappa p \ll 1$, which is valid for diagnostic ultrasound imaging. After the first reflection, the manipulation pressure drops and the further propagation is, as in THI, assumed to be linear. Thus, $\beta_{\mathrm{n}}\kappa p$ can be neglected ($c = c_0$).

The manipulation pressure varies both over the imaging pulse duration and spatially within the medium insonified by the beam. This will cause frequency shifts, pulse distortion and nonlinear aberration [22]. These effects are neglected in the presented algorithms and a constant $p$ is assumed over the imaging pulse both in space and time. It may, however, vary with depth. To approach an almost constant pressure in practice, a transmit setup with a plane wave manipulation pulse and a large

frequency ratio, *e.g.*, 10:1, can be utilized.

The remaining effect is a change of the propagation velocity of the imaging pulse. In the chosen pulsing scheme one complex is sent with the imaging pulse on a manipulation pressure maximum and another complex with an inverted manipulation, the imaging pulse is thus in a pressure trough. This results in the received, beamformed, signals $y_+(t)$ and $y_-(t)$, respectively. The signal without manipulation is denoted $y_0(t)$ and is required to derivate the theory, but not acquired in practice. For convenience, in the article the signals are represented in their narrow band, complex notation $\boldsymbol{y}(t)$ with

$$y(t) = \Re\{\boldsymbol{y}(t)\} = \Re\left\{\tilde{\boldsymbol{y}}(t)\mathrm{e}^{\mathrm{i}\omega_\mathrm{c}t}\right\}\,, \tag{C.2}$$

where $\tilde{\boldsymbol{y}}$ is the complex envelope. The amplitude and phase of the complex envelopes follow gaussian random distributions due to the random ensemble of scatterers in an imaging scene. The signal contains a phasor component around the pulse center frequency $f_\mathrm{c} = \omega_\mathrm{c}/2\pi$. For brevity, throughout this article $\omega$ will be used instead of $\omega_\mathrm{c}$, even though all signal descriptions are narrow band approximations.

The net difference in propagation velocity between the two imaging pulses yields a propagation delay which accumulates with depth. An example is displayed in Fig. C.2, where a section of the received signal for both transmits is displayed for two locations, one close and one distant to the transducer. The close one exhibits a small propagation delay, the distant one a larger delay. Integrating Eq. (C.1) along the propagation path yields the one-sided (between a pulse with and without manipulation) propagation delay $\tau$ which might be approximated as:

$$\tau_\mathrm{r}(z) \approx -\frac{1}{c_0}\int_0^z \beta_\mathrm{n}(s)\kappa(s)p(s)\mathrm{d}s\,. \tag{C.3}$$

Where $\beta_\mathrm{n}$, $\kappa$ and $p$ are material dependent variables along the propagation direction of increasing $s$. Still, $\kappa p \ll 1$ is assumed. The delay increase which can be achieved in a typical setting in tissue is about 0.5 ns per mm (using $c_0 = 1540\,\mathrm{m/s}$, $\kappa = 400 \cdot 10^{-12}\,\mathrm{Pa}^{-1}$, $\beta_\mathrm{n} = 3.9$, $p = 0.5\,\mathrm{MPa}$). The two-sided propagation delay between $y_+$ and $y_-$ is then $2\tau_\mathrm{r}$ and thus increases typically with about 1 ns per mm propagation depth.

Using the delay accumulation of 0.5 ns/mm, assuming a maximum imaging depth of 200 $\lambda$, $c = 1540\,\mathrm{m/s}$ and inserting $\lambda = c/f_\mathrm{c} = cT$, a maximum accumulated delay can be computed:

$$\tau_\mathrm{max} = 0.5\frac{\mathrm{ns}}{\mathrm{mm}} \cdot 200\lambda \approx 0.15T\,. \tag{C.4}$$

Thus, the total accumulated delay will not be greater than 0.15 times the wavelength of the imaging pulse for the chosen parameters.

In an imaging situation where reverberations occur, the estimated time delay from a received signal at a certain depth will differ from the theoretical propagation delay of that depth due to overlapping reverberations, which carry the delay corresponding to their respective depth of first reflection. The delay of the sum will be between the first order delay $\tau_\mathrm{f}$ and the delay of the reverberation $\tau_\mathrm{r}$. To show that, we assume

that the manipulated signal consists of two components, a first order component $\boldsymbol{s}$ and a reverberation component $\boldsymbol{r}$:

$$\begin{aligned}\boldsymbol{y}_+(t) = \tilde{\boldsymbol{y}}_+(t)\mathrm{e}^{\mathrm{i}\omega(t+\tau_\mathrm{y})} &\approx \boldsymbol{s}_+(t) + \boldsymbol{r}_+(t) \\ &= \tilde{\boldsymbol{s}}(t+\tau_\mathrm{f})\mathrm{e}^{\mathrm{i}\omega(t+\tau_\mathrm{f})} + \tilde{\boldsymbol{r}}(t+\tau_\mathrm{r})\mathrm{e}^{\mathrm{i}\omega(t+\tau_\mathrm{r})}\,.\end{aligned} \tag{C.5}$$

where the positively manipulated signal is taken as an example. In general all $\tau$ vary with propagation depth but this time dependence is omitted in the formula and in the following for brevity. In the previous equation $\tilde{\boldsymbol{s}}$ and $\tilde{\boldsymbol{r}}$ are complex modulation envelopes which are assumed not to change with manipulation, $t$ time and $\tau$ propagation delays.

To determine $\tau_y$, the manipulated signal is correlated with the signal without manipulation $y_0$ using Eq. (C.5):

$$\mathrm{E}\left\{\boldsymbol{y}_+(t)\boldsymbol{y}_0^*(t)\right\} = \mathrm{E}\left\{\left[\tilde{\boldsymbol{s}}(t+\tau_\mathrm{f})\mathrm{e}^{\mathrm{i}\omega\tau_\mathrm{f}} + \tilde{\boldsymbol{r}}(t+\tau_\mathrm{r})\mathrm{e}^{\mathrm{i}\omega\tau_\mathrm{r}}\right]\left[\tilde{\boldsymbol{s}}(t) + \tilde{\boldsymbol{r}}(t)\right]^*\right\}\,, \tag{C.6}$$

where E is the ensemble mean. Considering $\tilde{\boldsymbol{s}}$ and $\tilde{\boldsymbol{r}}$ uncorrelated, this becomes:

$$\begin{aligned}\mathrm{E}\left\{\boldsymbol{y}_+(t)\boldsymbol{y}_0^*(t)\right\} &= \mathrm{E}\left\{\tilde{\boldsymbol{s}}(t+\tau_\mathrm{f})\tilde{\boldsymbol{s}}^*(t)\right\}\mathrm{e}^{\mathrm{i}\omega\tau_\mathrm{f}} + \mathrm{E}\left\{\tilde{\boldsymbol{r}}(t+\tau_\mathrm{r})\tilde{\boldsymbol{r}}^*(t)\right\}\mathrm{e}^{\mathrm{i}\omega\tau_\mathrm{r}} \\ &= \mathrm{R}_{\tilde{\boldsymbol{s}}}\left(t,\tau_\mathrm{f}\right)\mathrm{e}^{\mathrm{i}\omega\tau_\mathrm{f}} + \mathrm{R}_{\tilde{\boldsymbol{r}}}\left(t,\tau_\mathrm{r}\right)\mathrm{e}^{\mathrm{i}\omega\tau_\mathrm{r}}\end{aligned} \tag{C.7}$$

with $\mathrm{R}\left(t,\tau\right)$ being the ensemble auto correlation function which is expected to vary slowly with $\tau$ for both, $\tilde{\boldsymbol{s}}$ and $\tilde{\boldsymbol{r}}$ since $\tau < 0.15T$, as shown in Eq. (C.4). It is therefore assumed that $\mathrm{R}\left(t,\tau\right) \approx \mathrm{R}\left(t,0\right)$. The angle of the correlation function equals the difference in the angle of the $\boldsymbol{y}_+$ and the $\boldsymbol{y}_0$ signal and thus $\omega\tau_\mathrm{y}$:

$$\omega\tau_\mathrm{y} = \angle\mathrm{E}\left\{\boldsymbol{y}_+(t)\boldsymbol{y}_0^*(t)\right\} = \arctan\left(\frac{\mathrm{R}_{\tilde{\boldsymbol{s}}}\left(t,0\right)\sin\omega\tau_\mathrm{f} + \mathrm{R}_{\tilde{\boldsymbol{r}}}\left(t,0\right)\sin\omega\tau_\mathrm{r}}{\mathrm{R}_{\tilde{\boldsymbol{s}}}\left(t,0\right)\cos\omega\tau_\mathrm{f} + \mathrm{R}_{\tilde{\boldsymbol{r}}}\left(t,0\right)\cos\omega\tau_\mathrm{r}}\right) \tag{C.8}$$

Assuming further $\sin\omega\tau \approx \omega\tau$, $\cos\omega\tau \approx 1$, $\arctan\varphi \approx \varphi$ which are valid approximations for small angles $\omega\tau \ll 1, \varphi \ll 1$. Inserting as well the autocorrelation function for zero delay yields:

$$\omega\tau_\mathrm{y} = \angle\mathrm{E}\left\{\boldsymbol{y}_+(t)\boldsymbol{y}_0^*(t)\right\} \approx \omega\frac{\left|\tilde{\boldsymbol{s}}(t)\right|^2\tau_\mathrm{f} + \left|\tilde{\boldsymbol{r}}(t)\right|^2\tau_\mathrm{r}}{\left|\tilde{\boldsymbol{s}}(t)\right|^2 + \left|\tilde{\boldsymbol{r}}(t)\right|^2} \tag{C.9}$$

The angle is thus proportional with $\omega$ and expresses a fixed delay. The trigonometric approximations are evaluated in total in Fig. C.3, where the error between the right hand side of Eq. (C.8) and Eq. (C.9) is compared. In the upper panel a fixed ratio of 0.5 between $\tau_\mathrm{r}$ and $\tau_\mathrm{f}$ is kept, while $\left|\tilde{\boldsymbol{s}}(t)\right|^2 / \left|\tilde{\boldsymbol{r}}(t)\right|^2$ is inserted for different values ranging from -80 dB to 80 dB. In that case the error is below 1% in any case. In the lower panel, for a fixed $\left|\tilde{\boldsymbol{s}}(t)\right|^2 / \left|\tilde{\boldsymbol{r}}(t)\right|^2 = -15\,\mathrm{dB}$ the $\tau_\mathrm{r}/\tau_\mathrm{f}$ ratio is varied from 0 to 1. The maximum error, with up to 15% error at $0.15T$, is observed if $\tau_\mathrm{r} = 0$, while already with $\tau_\mathrm{r} = 0.25\tau_\mathrm{f}$ it is below 5%.

The derivation of $\tau_\mathrm{y}$ is also valid for more than one reverberation component since $\boldsymbol{r}$ might represent a sum of reverberations.

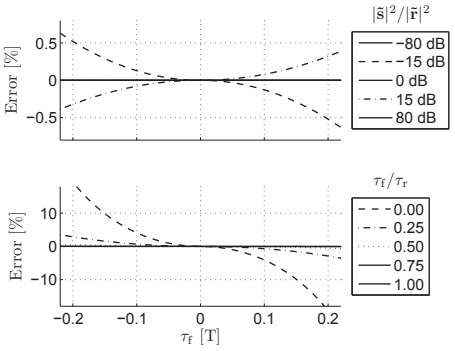


Figure C.3: Error analysis of Eq. (C.9). Upper panel: Error in percent of the estimate compared to the analytical solution for varying amplitudes of the signal and reverberation component, $\tau_\mathrm{r}/\tau_\mathrm{f} = 0.5$. Lower panel: For the $-15\,\mathrm{dB}$ case, varying $\tau_\mathrm{r}/\tau_\mathrm{f}$.

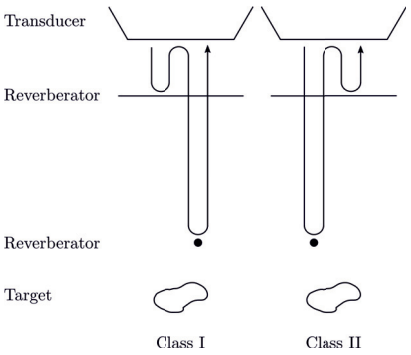


Figure C.4: Classification of reverberations according to [10]. Depicted is the order in which the reverberation hits the different reverberators if a beam is transmitted straight down.

Høilund-Kaupang *et al.* [10] presented a classification scheme for reverberations in medical ultrasound. The scheme is most suited for third order reverberations with the transducer as second reverberator. The term 'third order' means they have been reflected three times before being received by the transducer. The classification states that reverberations always occur in pairs which follows from reciprocity since the propagation path in a quasistationary medium can be inverted. Fig. C.4 displays a class I reverberation where the first reflection occurs close to the transducer and a class II reverberation where the first reflection occurs close to the target, the two having inverse propagation paths. As noted above, THI will attenuate class I reverberations stronger than class II reverberations. Høilund-Kaupang *et al.* show further that in case of equal transmit and receive beams the reverberation signal from class I and class II is equal for linear propagation. For nonlinear propagation the signals will differ.

For signals containing third order reverberations, the delay accumulation is evaluated in more depth: Let $\boldsymbol{y}_+(t)$ and $\boldsymbol{y}_-(t)$ be the received signal after beamforming with positive and negative manipulation, respectively. As in Eq. (C.5) they consist of one first order component and one reverberation component. It is now assumed that the reverberation component consists of third order scattering with the transducer as second reverberator, only. In this case, given a scatterer at depth $z_1$, another scatterer at $z_3 = z - z_1$ is required to cause a reverberation pair which can be observed at $z$. The reverberation component $\boldsymbol{r}(t)$ consists of a superposition of all reverberation pairs with one of the scatterers within $(0, z/2)$. This can be described as (with $z = c_0 t/2$):

$$\boldsymbol{r}_\pm(t) \approx \int_0^{z/2} \left[\boldsymbol{r}_\mathrm{I}(t, z_1)\mathrm{e}^{\pm \mathrm{i}\omega\tau_\mathrm{f}(z_1)} + \boldsymbol{r}_\mathrm{II}(t, z_1)\mathrm{e}^{\pm \mathrm{i}\omega\tau_\mathrm{f}(z-z_1)}\right] \mathrm{d}z_1, \tag{C.10}$$

where $\boldsymbol{r}_{\mathrm{I}}$ and $\boldsymbol{r}_{\mathrm{II}}$ are the reverberation components of class I and class II, respectively. They carry their respective first order delays which corresponds to their depth of first scattering, which is $z_1$ and $z - z_1$.

If the same transmit and receive beam is applied, which implies $\boldsymbol{r}_{\mathrm{I}} = \boldsymbol{r}_{\mathrm{II}}$ [10], and assuming a linear delay accumulation with depth, *i.e.,* $\tau_{\mathrm{f}}(z) = \alpha z$, this can, analog to Eqs. (C.8) and (C.9), be utilized to estimate a reverberation delay $\tau_{\mathrm{r}}$ to:

$$\tau_{\mathrm{r}}(z) \approx \frac{\alpha z \left| \int_0^{z/2} \tilde{\boldsymbol{r}}_{\mathrm{I}}(t, z_1)\, \mathrm{d}z_1 \right|^2}{2 \left| \int_0^{z/2} \tilde{\boldsymbol{r}}_{\mathrm{I}}(t, z_1)\, \mathrm{d}z_1 \right|^2} = \frac{\alpha z}{2} = \tau_{\mathrm{f}}(z/2) \tag{C.11}$$

In other words if a signal is recorded with the same transmit and receive beam, and a linear delay accumulation is achieved, the delay of the reverberation component at a certain depth will be equal to the first order delay at half that depth.

## C.3 Method

In this section the applied methods and algorithms will be presented. First, delay estimation is introduced, followed by two methods for reverberation suppression and a description of the simulation and experimental setup.

### C.3.1 Delay estimation

To estimate the time delay $\hat{\tau}_{\mathrm{y}}$ between the two received signals $y_+$ and $y_-$ the algorithm presented by Standal *et al.* [23] is used. The algorithm utilizes a cross-correlation technique to estimates phase differences. Together with a parametric delay model and an estimation of the instantaneous frequency, the delays are found through minimization, *i.e.,* with minimum least squares.

As described in the previous section, the estimated signal delay $\hat{\tau}_{\mathrm{y}}$ will hardly equal $\tau_{\mathrm{f}}$ in *in vivo* imaging since reverberations and possibly other artifacts will impair the estimate. Both methods below require an estimate of the first order delay $\hat{\tau}_{\mathrm{f}}$. In the following section, we will assume to have a reliable estimate for the first order delay $\tau_{\mathrm{f}}$.

### C.3.2 Delay corrected subtraction (DCS)

The delay corrected subtraction (DCS) method is based on the DBI subtraction method, an approach where the two signals with alternating manipulation are filtered around the imaging band and then subtracted [14]:

$$\begin{aligned} \boldsymbol{y}_{\mathrm{i}}(t) &= \boldsymbol{y}_+(t) - \boldsymbol{y}_-(t) \\ &= \tilde{\boldsymbol{s}}(t)\mathrm{e}^{\mathrm{i}\omega t}\left[\mathrm{e}^{\mathrm{i}\omega\tau_{\mathrm{f}}} - \mathrm{e}^{-\mathrm{i}\omega\tau_{\mathrm{f}}}\right] + \tilde{\boldsymbol{r}}(t)\mathrm{e}^{\mathrm{i}\omega t}\left[\mathrm{e}^{\mathrm{i}\omega\tau_{\mathrm{r}}} - \mathrm{e}^{-\mathrm{i}\omega\tau_{\mathrm{r}}}\right] \\ &= 2\mathrm{i}\mathrm{e}^{\mathrm{i}\omega t}\left[\tilde{\boldsymbol{s}}(t)\sin\omega\tau_{\mathrm{f}} + \tilde{\boldsymbol{r}}(t)\sin\omega\tau_{\mathrm{r}}\right] \end{aligned} \tag{C.12}$$

where $y_\mathrm{i}$ is the imaging signal. Since $\tau_\mathrm{f} > \tau_\mathrm{r}$, and, $\omega\tau_\mathrm{f}$ is small, compared to a conventional image the reverberation component is attenuated. This works well for class I reverberations, but class II reverberations with $\tau_\mathrm{r} \approx \tau_\mathrm{f}$ will not be considerably attenuated.

Examining Eq. (C.12), correcting for a suitable delay $\hat{\tau}_\mathrm{r} \approx \tau_\mathrm{r}$ prior to subtraction will cause the reverberation component to vanish and the imaging signal consists of first order signal, only:

$$\begin{aligned} \boldsymbol{y}_i(t) &= \boldsymbol{y}_+(t)\mathrm{e}^{-\mathrm{i}\omega\hat{\tau}_\mathrm{r}} - \boldsymbol{y}_-(t)\mathrm{e}^{\mathrm{i}\omega\hat{\tau}_\mathrm{r}} \\ &= \tilde{\boldsymbol{s}}(t)\mathrm{e}^{\mathrm{i}\omega t}\left[\mathrm{e}^{\mathrm{i}\omega(\tau_\mathrm{f}-\hat{\tau}_\mathrm{r})} - \mathrm{e}^{-\mathrm{i}\omega(\tau_\mathrm{f}-\hat{\tau}_\mathrm{r})}\right] + \tilde{\boldsymbol{r}}(t)\mathrm{e}^{\mathrm{i}\omega t}\left[\mathrm{e}^{\mathrm{i}\omega(\tau_\mathrm{r}-\hat{\tau}_\mathrm{r})} - \mathrm{e}^{-\mathrm{i}\omega(\tau_\mathrm{r}-\hat{\tau}_\mathrm{r})}\right] \\ &= 2\mathrm{i}\mathrm{e}^{\mathrm{i}\omega t}\tilde{\boldsymbol{s}}(t)\sin\omega\left(\tau_\mathrm{f} - \hat{\tau}_\mathrm{r}\right) \end{aligned} \tag{C.13}$$

Two ways to determine $\hat{\tau}_\mathrm{r}$ are presented here. First, Näsholm *et al.* introduced correction for a fixed, depth independent $\hat{\tau}_\mathrm{r}$ if the user suspects that reverberations could originate from a certain structure [16].

The second way is to apply a depth dependent $\hat{\tau}_\mathrm{r}(z)$, $z = c_0 t/2$. In this case, one can utilize Eq. (C.11), which shows that the propagation delay of a reverberation component observed at one depth will be equal to the first order delay which is observed at half that depth. This under the additional assumptions of equal transmit and receive beams, equal nonlinear distortion of both the class I and the class II component and a linear propagation accumulation with depth. If these assumptions hold, the first order delay of half the depth is a good estimate for the propagation delay of the reverberation component:

$$\hat{\tau}_\mathrm{r}(z) = \hat{\tau}_\mathrm{f}(z/2) \approx \tau_\mathrm{r}(z) \tag{C.14}$$

With a good first order delay estimate $\hat{\tau}_\mathrm{f} \approx \tau_\mathrm{f}$, $\tau_\mathrm{r}(z) = \tau_\mathrm{f}(z/2)$, and using the assumption of linear delay accumulation $\tau_\mathrm{f}(z) = \alpha z$, insertion into Eq. (C.13) yields:

$$\boldsymbol{y}_\mathrm{i}(t) = 2\mathrm{i}\mathrm{e}^{\mathrm{i}\omega t}\tilde{\boldsymbol{s}}(t)\sin\omega\tau_\mathrm{f}(z)/2 \tag{C.15}$$

In other words, if the assumptions are valid, the reverberation component is totally removed from the imaging signal for all depths. This is illustrated in Fig. C.5, which displays reverberations of both classes prior to and after correction. Class I exhibits less delay than class II prior to correction since it has experienced less manipulation during propagation. For equal amplitudes the correction delay is the mean of the class I and II delays. Applying the correction, it becomes evident that the class I component of the positively manipulated signal cancels with the class II component of the negatively manipulated signal and vice versa.

### C.3.3 First order content weighting (FOCW)

The DCS method is dependent on equal pulse forms of the two imaging pulses to yield high attenuation. If nonlinear propagation effects distort the pulses differently for different manipulations or if beamforming or nonlinear self distortion makes the reverberation signal different for class I and II, attenuation will be impaired.

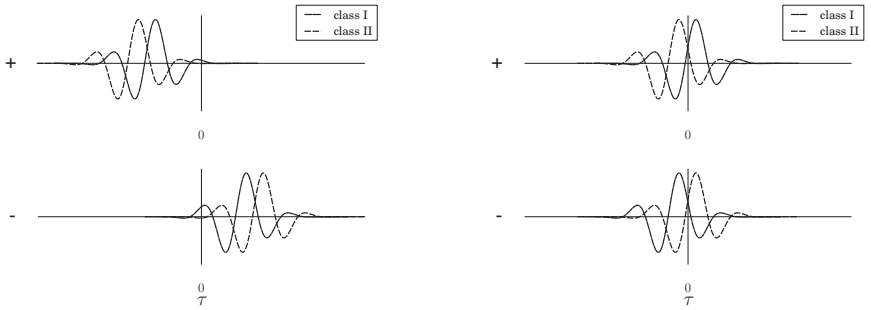


(a) Before delay correction

(b) After delay correction

Figure C.5: Illustration of signals of class I (solid line) and class II (dashed line) reverberations before and after delay correction for the DCS method. Upper line positive manipulation, lower line negative manipulation. The delays are magnified for better illustration.

At the same time, the different propagation delays in the signal are the information which is utilized for attenuating the reverberations. This information is not dependent on the imaging signal and can be applied to just one of the imaging signals to circumvent lower attenuation due to distorted pulses.

Therefore, instead of delay correcting and subtracting $y_+$ and $y_-$, either $y_+$ or $y_-$ is corrected for two different correction delays $\tau_{c1}, \tau_{c2}$ and then subtracted:

$$\boldsymbol{y}_{i+}(t) = \boldsymbol{y}_+(t)\mathrm{e}^{-\mathrm{i}\omega\tau_{c1}} - \boldsymbol{y}_+(t)\mathrm{e}^{-\mathrm{i}\omega\tau_{c2}}\,. \tag{C.16}$$

Using the local delay $\tau_{c1} = \hat{\tau}_y(z)$ and the estimated reverberation delay $\tau_{c2} = \hat{\tau}_r$ yields an imaging signal which will be strongly attenuated if $\tau_r \approx \hat{\tau}_y$:

$$\boldsymbol{y}_{i+}(t) = \boldsymbol{y}_+(t)\mathrm{e}^{-\mathrm{i}\omega\hat{\tau}_y} - \boldsymbol{y}_+(t)\mathrm{e}^{-\mathrm{i}\omega\hat{\tau}_r}\,. \tag{C.17}$$

For example, in a hypoechoic region like a cavity or a blood vessel, the signal will consist of reverberations only. The local delay is thus equal to the reverberation delay and the reverberation component will be suppressed (requires $\tau_r = \hat{\tau}_r$). In regions with first order scattering the delays will differ and the signal is maintained.

Rearranging Eq. (C.17) and applying trigonometric addition theorems yields

$$\begin{aligned}\boldsymbol{y}_{i+}(t) &= \boldsymbol{y}_+(t)\left[\mathrm{e}^{-\mathrm{i}\omega\hat{\tau}_y} - \mathrm{e}^{-\mathrm{i}\omega\hat{\tau}_r}\right] \\ &= 2\sin\left(\frac{\omega\hat{\tau}_y - \omega\hat{\tau}_r}{2}\right)\boldsymbol{y}_+(t)\mathrm{e}^{-\frac{1}{2}\mathrm{i}(\pi+\omega\hat{\tau}_y+\omega\hat{\tau}_r)}\,.\end{aligned} \tag{C.18}$$

Thus, the signal amplitude is weighted with a sine function dependent on $\hat{\tau}_y$ and $\hat{\tau}_r$. Eq. (C.18) can further be rewritten with a delay dependent real weighting function $w(t)$

and a phase shift $\varphi$:

$$\boldsymbol{y}_{\mathrm{i}}(t) = w(t)\boldsymbol{y}_{+}(t)\mathrm{e}^{-\mathrm{i}\varphi}\,. \tag{C.19}$$

This opens for use of other weighting functions as, *e.g.*, $w(t) = \hat{\tau}_{\mathrm{y}} - \hat{\tau}_{\mathrm{r}}$, which do not exhibit a nonlinear dependence on their arguments. The delay $\tau$ will increase with depth as described above. In this case the value of both presented functions for $w(t)$ will increase with depth, which can be shown if $\tau_{\mathrm{y}} = \tau_{\mathrm{f}}$ and $\tau_{\mathrm{r}}(z) = \tau_{\mathrm{f}}(z/2)$ is inserted. This is generally not desired as it introduces an additional gain to the signal.

This gain can be avoided if

$$w(t) = \frac{\hat{\tau}_{\mathrm{y}} - \hat{\tau}_{\mathrm{r}}}{\hat{\tau}_{\mathrm{f}} - \hat{\tau}_{\mathrm{r}}} \tag{C.20}$$

is chosen as the weighting function, introducing a normalization to the expected delay range. Thus the value should stay in the range between 0 and 1 and is only dependent on the ratio between the maximum achievable delay difference and the delay estimated from the signal.

From Eq. (C.5) we can derive the local signal-to-reverberation-ratio (SRR) to:

$$\mathrm{SRR}(t) = \left|\frac{\tilde{\boldsymbol{s}}(t)}{\tilde{\boldsymbol{r}}(t)}\mathrm{e}^{\mathrm{i}\omega(\tau_{\mathrm{f}}-\tau_{\mathrm{r}})}\right|^2 = \frac{|\tilde{\boldsymbol{s}}(t)|^2}{|\tilde{\boldsymbol{r}}(t)|^2} \tag{C.21}$$

Inserting Eq. (C.9) into Eq. (C.20) and assuming correct estimates yields (time/depth dependence omitted):

$$w = \frac{\frac{|\tilde{\boldsymbol{s}}|^2\tau_{\mathrm{f}}+|\tilde{\boldsymbol{r}}|^2\tau_{\mathrm{r}}}{|\tilde{\boldsymbol{s}}|^2+|\tilde{\boldsymbol{r}}|^2} - \frac{\tau_{\mathrm{r}}\left(|\tilde{\boldsymbol{s}}|^2+|\tilde{\boldsymbol{r}}|^2\right)}{|\tilde{\boldsymbol{s}}|^2+|\tilde{\boldsymbol{r}}|^2}}{\tau_{\mathrm{f}} - \tau_{\mathrm{r}}} = \frac{|\tilde{\boldsymbol{s}}|^2}{|\tilde{\boldsymbol{s}}|^2 + |\tilde{\boldsymbol{r}}|^2} = \frac{1}{1+\mathrm{SRR}^{-1}} \tag{C.22}$$

In other words, the weighting function Eq. (C.20) is a measure of first order signal content in the received signal, and a function of the local SRR. Weighting the $y_{+}$ signal with it will attenuate the parts of the signal where reverberations dominate the signal. The amplitude of the imaging signal will equal the amplitude of the first order signal.

In the following initial evaluation of the methods, $\hat{\tau}_{\mathrm{r}} = \hat{\tau}_{\mathrm{f}}(z/2)$ will be used for FOCW.

### C.3.4 Evaluation

To demonstrate the performance of the proposed methods, a number of evaluation examples are presented. The examples consist of three simulated single imaging lines and experimental *in vivo* images.

#### Simulations

The simulations are performed with a spectrum element method (SEM) code by Høilund-Kaupang and Angelsen [10]. It handles both (nonlinear) forward and back

propagation simultaneously and accounts for multiple scattering, reflections and reverberations. The program integrates a set of model equations in time. The second order accurate acoustic equations are utilized in this code as model equations. They account for nonlinear elasticity of the medium and frequency dependent absorption. The code used in this article is verified against analytic results for the absorption model and nonlinear propagation in a plane wave situation. Two-dimensional propagation is compared with the results from a forward propagation simulation tool, Abersim [10, 24–26]. All simulations were carried out in two dimensions.

The polynomial order used in this article is 16, and the sampling frequency in time is 167 MHz. The lateral simulation domain size is 21.8 mm which corresponds to 66 transducer elements. The simulated transducer has a 300 $\mu$m pitch, 8 MHz center frequency on the HF array, 0.9 MHz on the LF array. The active transmit aperture has the same size as 24 elements, however no transducer elements, kerf between elements or effective element sizes are simulated. The focusing delay is not quantized in transducer elements. The transmit pulse is defined as pressure pulse on the surface of the transducer. A gaussian pulse with 50% bandwidth and 500 kPa amplitude is chosen, both for the HF and the LF pulse. The transducer is modelled as a totally reflecting surface. After computing the result on all nodes, artificial transducer element signals were generated by averaging the node signals over the transducer pitch. Two types of receive beamforming are carried out on the simulated data. First, dynamic focus on receive with maximum, 64 element wide, aperture ($H_\mathrm{r}$ dyn). Second, beamforming is carried out with the same aperture and focus as on transmit ($H_\mathrm{t} = H_\mathrm{r}$) to fulfill the requirements of the DCS method.

Three different image lines are simulated. The first simulation, line I, represents an *in vitro* water tank setup with a planar reflector at 8 mm depth, a point scatterer at 13 mm and a point scatterer as imaging target at 21 mm depth. The plane is simulated as a film made of polypropylen with 50 $\mu$m thickness, the point scatterers made of nylon with 200 $\mu$m diameter. The applied material parameters are given in Tab. C.1. Each material is defined through its speed of sound $c$, its density $\rho$, the nonlinearity parameter $\beta_\mathrm{n}$ and an attenuation $\alpha f^\beta$. Linear propagation is assumed within the planar reflector and the point. Water, plane and points are modelled to consist of homogeneous material with no further scatterers.

This phantom will create distinct reverberations, amongst others at 16, 18 and 21 mm (see Tab. C.2 for full list with propagation paths). One of the reverberations will overlap with the first order echo from 21 mm.

For the second line, line II, propagation through a homogeneous scattering medium is simulated. The material properties are chosen to be similar to muscle tissue (see Tab. C.1). To create scattering, 24 small circular scatterers of 20 $\mu$m diameter each are placed at random locations in each resolution cell. The material of these scatterers is based on the background material. The speed of sound of each scatterer is constant and randomly chosen with a uniform random distribution. The mean sound velocity variance is 5%.

In the homogeneous phantom a low level of reverberations is expected. Thus, the first order delay estimation can be validated and the gain factor observed.

The third *in vitro* phantom is supposed to create a more realistic imaging situation.

Table C.1: Material parameters for the different components of the simulation phantom.

| Material | line | $c$ [m/s] | $\rho$ [kg/m$^3$] | $\beta_\mathrm{n}$ | $\alpha$ [dB/cm/MHz] | $\beta$ |
|---|---|---|---|---|---|---|
| Polypropylen | I | 2740 | 880 | 0 | 1.02 | 1 |
| Nylon | I | 2600 | 1120 | 0 | 0.58 | 1 |
| Water | I | 1482 | 998 | 3.48 | $2 \cdot 10^{-3}$ | 2 |
| Muscle | II, III | 1550 | 1060 | 3.9 | 0.52 | 1.1 |
| Fat | III | 1478 | 928 | 5.8 | 0.9 | 3 |
| Blood | III | 1584 | 1060 | 4 | 1.2 | 0.12 |
| Connective tissue | III | 1613 | 1120 | 5 | 0.68 | 1.1 |

A geometry, which is inspired by the anatomy of the human carotid artery, was created and is depicted in Fig. C.6. It consists of different tissue types muscle, fat, connective tissue and blood filled cavities (see Tab. C.1 for material parameter details). The simulated line, line III, is marked in the image and crosses three cavities. The mean sound velocity variance of the scatterers is 5% for fat and connective tissue while it is 2.5% for muscle. No scatterers were inserted in the blood filled cavities.

For all lines, two simulations were conducted with alternating manipulation. The imaging pulse is thus placed either on a pressure peak or in a pressure trough. The imaging pulse is focused on transmit at 21 mm depth, the manipulation wave is unfocused.

### *In vivo* data

The *in vivo* data is acquired with an Ultrasonix SonixRP[1] research scanner, which was modified and extended for DBI imaging. A dual frequency linear array with a 300 $\mu$m pitch on the 8 MHz imaging array and a 0.8 MHz manipulation array is utilized. 128 lines are acquired for each frame with two transmits per line with alternating manipulation. As in the simulations, the imaging transmit wave is focused while the manipulation wave is unfocused. On receive, dynamic focusing is applied. It was not possible to store pre-beamformed data. The images were acquired within a clinical study on patients recruited from the vascular surgery day clinic at St. Olavs University Hospital, Trondheim, Norway. The study was approved by the local ethics committee and all patients provided signed informed consent. The results will be published separately.

### First order delay estimation

To work properly, both DCS and FOCW require a decent $\hat{\tau}_\mathrm{f}$ estimate. For the simulation, there are two possibilities to acquire such an estimate. First, if not only the transducer signal, but also the sound field along the beam axis is exported during

[1] Ultrasonix, Vancouver, Canada, `http://www.ultrasonix.com`

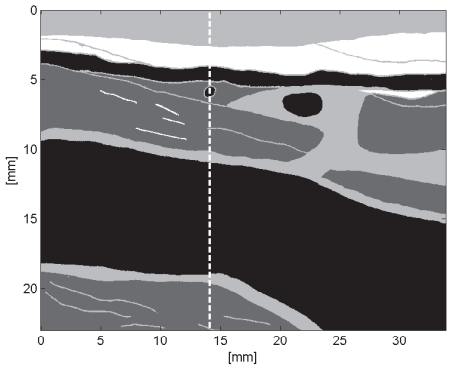


Figure C.6: Material map of the carotid artery mimicking phantom. Blood, muscle, connective tissue and fat are indicated by black, dark gray, light gray and white, respectively. The beam center is marked with the dashed line.

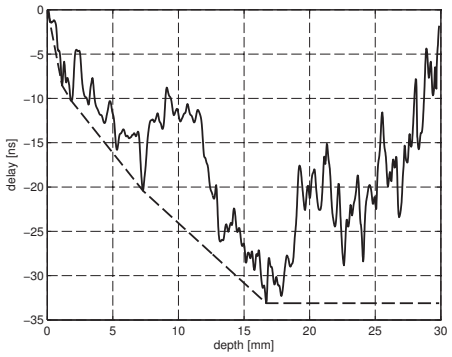


Figure C.7: First order delay estimation on a line of the *in vivo* dataset in Fig. C.11a at 33 mm lateral distance. Signal delay $\hat{\tau}_{\mathrm{y}}$ (solid black) and the first order estimate $\hat{\tau}_{\mathrm{f}}$ (dashed black). The carotid artery is located between 7 and 13 mm depth.

the simulation, the first order delay of the pulse can be determined while it propagates through the medium. This avoids that reverberations impair the estimate. To estimate the delay, a window around the imaging pulse of positive manipulation is cross-correlated with its negatively manipulated counter part. The raw estimate is smoothed with a median filter over 20 samples. This estimate will be termed $\hat{\tau}_{\mathrm{ff}}$.

The second method is also applicable to the *in vivo* data. First, one estimates the delay of the receive line $\hat{\tau}_{\mathrm{y}}$. In most imaging situations, $\hat{\tau}_{\mathrm{y}}$ will be impaired by reverberations. However, for strong first order scatterers the delay will approach $\tau_{\mathrm{f}}$. This can be utilized to estimate the first order delay $\hat{\tau}_{\mathrm{f}}$ for each depth from $\hat{\tau}_{\mathrm{y}}$. It is also possible to incorporate information from other image lines in space or different frames in time. Fig. C.7 displays $\hat{\tau}_{\mathrm{y}}$ and the derived $\hat{\tau}_{\mathrm{f}}$ for the second method. In this case, $\hat{\tau}_{\mathrm{f}}$ is found by interpolating linearly between a local minimum and the next local minimum that both is less than the first one and the interpolation line does not cross $\hat{\tau}_{\mathrm{y}}$. The presented $\hat{\tau}_{\mathrm{y}}$ is part of the *in vivo* dataset of the first patient presented in this article. The corresponding delay image is given in Fig. C.11a where the line is located at 33 mm lateral distance. It should be noted that the rough and no longer increasing delay development after 17 mm depth is due to low signal amplitude, as can be seen in the fundamental image in Fig. C.10a.

For all simulations $\hat{\tau}_{\mathrm{f}} = \hat{\tau}_{\mathrm{ff}}$ is used to demonstrate the potential of the methods if a good $\hat{\tau}_{\mathrm{f}}$ estimate can be found. In the *in vivo* case, $\hat{\tau}_{\mathrm{f}}$ is deduced from the echo data as described for the second method in the previous paragraphs.

Table C.2: Propagation path of the discrete reverberations in Fig. C.9a and C.9b. Abbreviations: T – transducer, R1 planar reverberator in 8 mm depth, R2 point scatterer in 13 mm depth. Reverberations with more than two reflections at R2 omitted.

| Depth [mm] | Propagation path |
|---|---|
| 16 | T - R1 - T - R1 - T |
| 18 | T - R2 - R1 - R2 - T |
| 21 | T - R1 - T - R2 - T |
| 21 | T - R2 - T - R1 - T |
| 24 | T - R1 - T - R1 - T - R1 - T |
| 26 | T - R2 - R1 - R2 - T - R1 - T |
| 26 | T - R2 - T - R2 - T |
| 29 | T - R1 - T - R1 - T - R2 - T |

## C.4 Results

### C.4.1 Simulations

The different estimated delays of the three simulated imaging lines are displayed in Fig. C.8. For all panels, the first order delay estimate $\hat{\tau}_{\mathrm{ff}}$ is given (solid black line), which is acquired from the sound field at the respective depth. In case of weak and homogeneous scattering, for the chosen transmit setup, $\hat{\tau}_{\mathrm{ff}}$ is smooth and close to linear, like in panel (b). The delay of the receive lines $\hat{\tau}_{\mathrm{y}}$ is close to equal to $\hat{\tau}_{\mathrm{ff}}$. For dynamic (dotted line) and fixed focus (solid gray) beamforming $\hat{\tau}_{\mathrm{y}}$ is similar for all three lines. The estimated reverberation delay $\hat{\tau}_{\mathrm{r}}$ is also given as the dash-dotted line.

Panel (a) shows the delay lines for the water tank setup. The setup contains a few, but strong scatterers and reflectors. While $\hat{\tau}_{\mathrm{ff}}$ is quite smooth with some dips, $\hat{\tau}_{\mathrm{y}}$ seems very rough and close to random. However, at the locations of the first two reverberators at 8 and 13 mm depth it is equal to $\hat{\tau}_{\mathrm{ff}}$.

Panel (c) is the delay plot corresponding to the carotid imitation phantom. $\hat{\tau}_{\mathrm{ff}}$ is rather linear here as well, while $\hat{\tau}_{\mathrm{y}}$ varies mainly between $\hat{\tau}_{\mathrm{r}}$ and $\hat{\tau}_{\mathrm{ff}}$, as expected. The changes in the material on the beam axis are visualized as colored bar, with the same color coding as in Fig. C.6.

The image lines after beamforming, reverberation suppression and log-compression are displayed in Fig. C.9. For each panel, the corresponding line is displayed for conventional fundamental (Fund), DBI subtraction (SUB) and DBI FOCW processing. The panels are arranged according to the simulation setup in rows, and the beamforming in columns. DCS and SUB are gain compensated with a factor of $1/(2\sin\omega\tau_{\mathrm{f}}/2)$. All panels are visualized with 60 dB dynamic range.

The first row contains the data of the water tank phantom. The image lines are normalized to each other at 13 mm depth. In addition to the first order echos at 8, 13 and 21 mm depth, reverberations at 16, 18, 21, 24, 26 and 29 mm can be observed, while 21 mm depth is the only depth with overlapping reverberation and first order echo. The propagation paths to the reverberations are given in Tab. C.2. The maximum

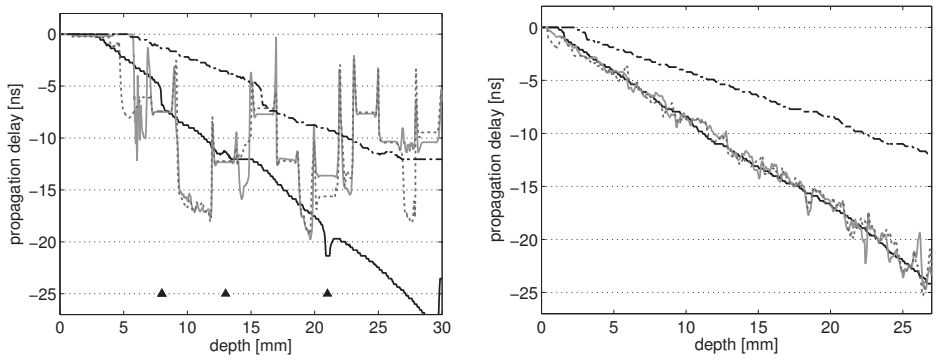


(a) Plane-point in water. Location of reverberators marked by triangles.

(b) Homogeneous scattering

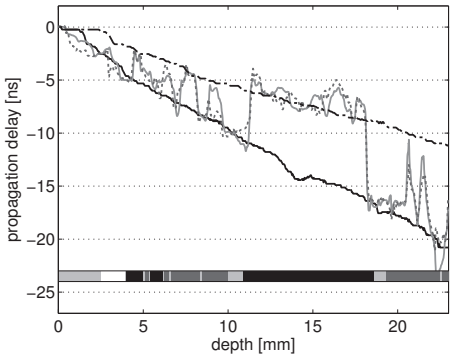


(c) Carotid imitation

Figure C.8: Estimated delays of the simulated lines. The first order delay estimate $\hat{\tau}_{\mathrm{ff}}$ (solid black line) is deduced from the sound field. The signal delay $\hat{\tau}_{\mathrm{y}}$ is estimated for the case of same transmit and receive field (solid gray line) and the dynamic focus on receive case (dotted line). The dash-dotted line is the correction delay $\tau_{\mathrm{r}}$. For the carotid imitation, also the material is given in the bar below with lines indicating the start and end of each cavity, colors and material according to Fig. C.6

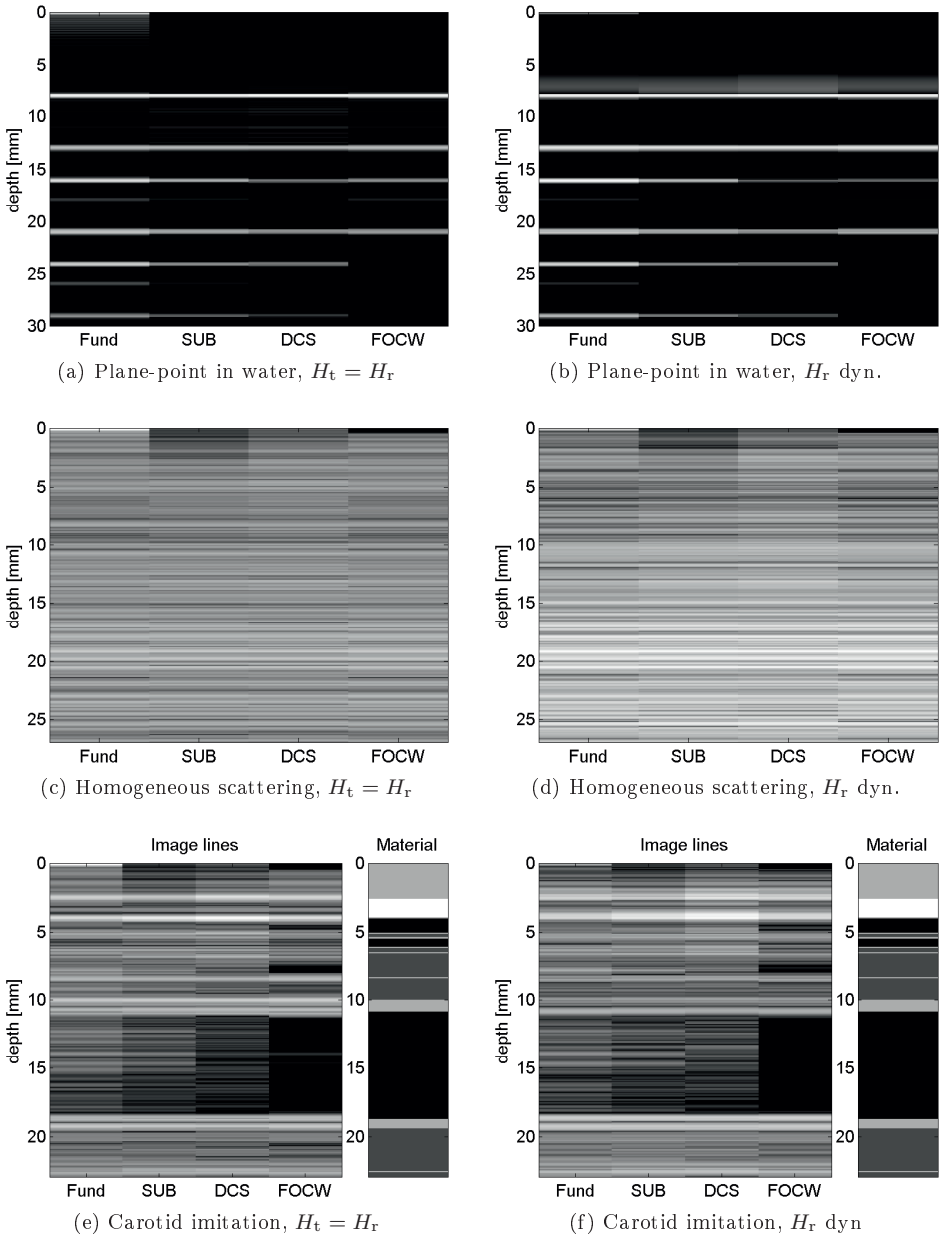


(a) Plane-point in water, $H_t = H_r$

(b) Plane-point in water, $H_r$ dyn.

(c) Homogeneous scattering, $H_t = H_r$

(d) Homogeneous scattering, $H_r$ dyn.

(e) Carotid imitation, $H_t = H_r$

(f) Carotid imitation, $H_r$ dyn

Figure C.9: Simulation lines (one in each row) processed for different algorithms: Fundamental imaging (Fund), DBI subtraction imaging (SUB), DBI delay corrected subtraction (DCS) and first order content weighting (FOCW). Left column $H_t = H_r$, right column dynamic focus on receive. All lines processed with 60 dB dynamic range. For the carotid imitation line, material distribution on the center line is given, colors and material according to Fig. C.6

Table C.3: Echo amplitude for the different echoes in Fig. C.9a and C.9b relative to the corresponding fundamental echo amplitude.

| | SUB | | DCS | | FOCW | |
|---|---|---|---|---|---|---|
| Depth | $H_t = H_r$ | $H_r$ dyn. | $H_t = H_r$ | $H_r$ dyn. | $H_t = H_r$ | $H_r$ dyn. |
| 16 | -10 | -11 | -22 | -25 | -17 | -27 |
| 18 | -7 | -6 | -12 | -12 | -5 | -4 |
| 21 | -7 | -6 | -11 | -8 | -9 | -5 |
| 24 | -14 | -14 | -20 | -19 | -80 | -80 |
| 26 | -12 | -12 | -27 | -27 | -80 | -42 |
| 29 | -12 | -12 | -19 | -20 | -80 | -80 |

Table C.4: Mean amplitude in the artery region of the carotid mimicking phantom relative to the maximum echo at the back wall. All values in dB. Values in parentheses is relative to the corresponding fundamental value in the same row.

| Beamforming | fundamental | SUB | DCS | FOCW |
|---|---|---|---|---|
| $H_t = H_r$ | -27 (0) | -33 (-7) | -40 (-13) | -58 (-31) |
| $H_r$ dyn. | -28 (0) | -34 (-6) | -36 (-8) | -64 (-37) |

amplitude at the different echo depths relative to the fundamental echo at the same depth is given in Tab. C.3. The DCS method attenuates reverberations stronger than the SUB method. Except for the reverberation in 18 mm depth and the echo in 21 mm, the FOCW method is more effective than the DCS method. The DCS method yields the sharpest edges compared with both other methods. The dynamic receive beam ($H_r$ dyn.) reduces the two minor reverberations in the fundamental line but has little effect in the other lines.

The results of the homogeneous scattering line show similar brightness at focus for all methods. The SUB method exhibits a dark near field, which, in a minor degree, also is true for the DCS method. There is a general increase in contrast if the dynamic receive beam is applied.

The image line of the carotid imitation yields similar results. The lines are normalized to 19 mm depth, which is the back wall of the 'artery'. Tab. C.4 contains the average amplitudes over a region of interest between 13 and 18 mm depth within the artery region. The methods in order of increasing attenuation is fundamental imaging, SUB, DCS and FOCW. If the same transmit and receive beam is utilized for acquisition, higher reverberation attenuation is achieved for the SUB and the DCS method, while dynamic focus on receive yields a higher attenuation for FOCW. Note that the color coding of the material is no indication how the image line should look like – despite the black sections.

### C.4.2 *In vivo* data

Two *in vivo* datasets are presented for fundamental, DCS and FOCW imaging. At the time of image acquisition, patient 1 and 2 were 82 and 67 years old, respectively. Both patients are men.

Patient 1 has a prominent plaque which due to absorption casts a shadow down the image as depicted in the fundamental image in Fig. C.10a. The lumen of the artery is filled with noise on both sides of the plaque. It is hard to delineate the plaque contour. In the DCS image in Fig. C.10c the plaque border is clearer but the plaque is filled with speckle. Some of the noise in the artery lumen is removed and a tissue structure in the upper left becomes darker. In the FOCW image, Fig. C.10e, the lumen is clear, the plaque is reduced to non contiguous areas. A black vertical line artifact in the upper left is visible.

Patient 2 has little plaque in the carotid artery, which is depicted in Fig. C.10b. The proximal half of the lumen is filled with reverberations, partly being clear replica of the tissue layers close to the transducer. The DCS image (Fig. C.10d) removes the distinct reverberations leaving some weak reverberations behind. The visual appearence of the DCS and the FOCW image (compare Fig. C.10f) is similar. The FOCW image has a little more contrast. Weak echoes at the artery back wall (left and central) and structures within the dark tail artifact are removed.

Fig. C.11 depicts $\hat{\tau}_{\mathrm{y}}$ as grayscale image. It is not as sharp as the ultrasound images, but resembles the same geometry. A dark stripe with low delay is seen in the left of both images, while it is more prominent in patient 1. The estimate of patient 1 in the distal, central region is random noise. The dark tail artifact in the image of patient 2 is also visible as a tail with low propagation delay.

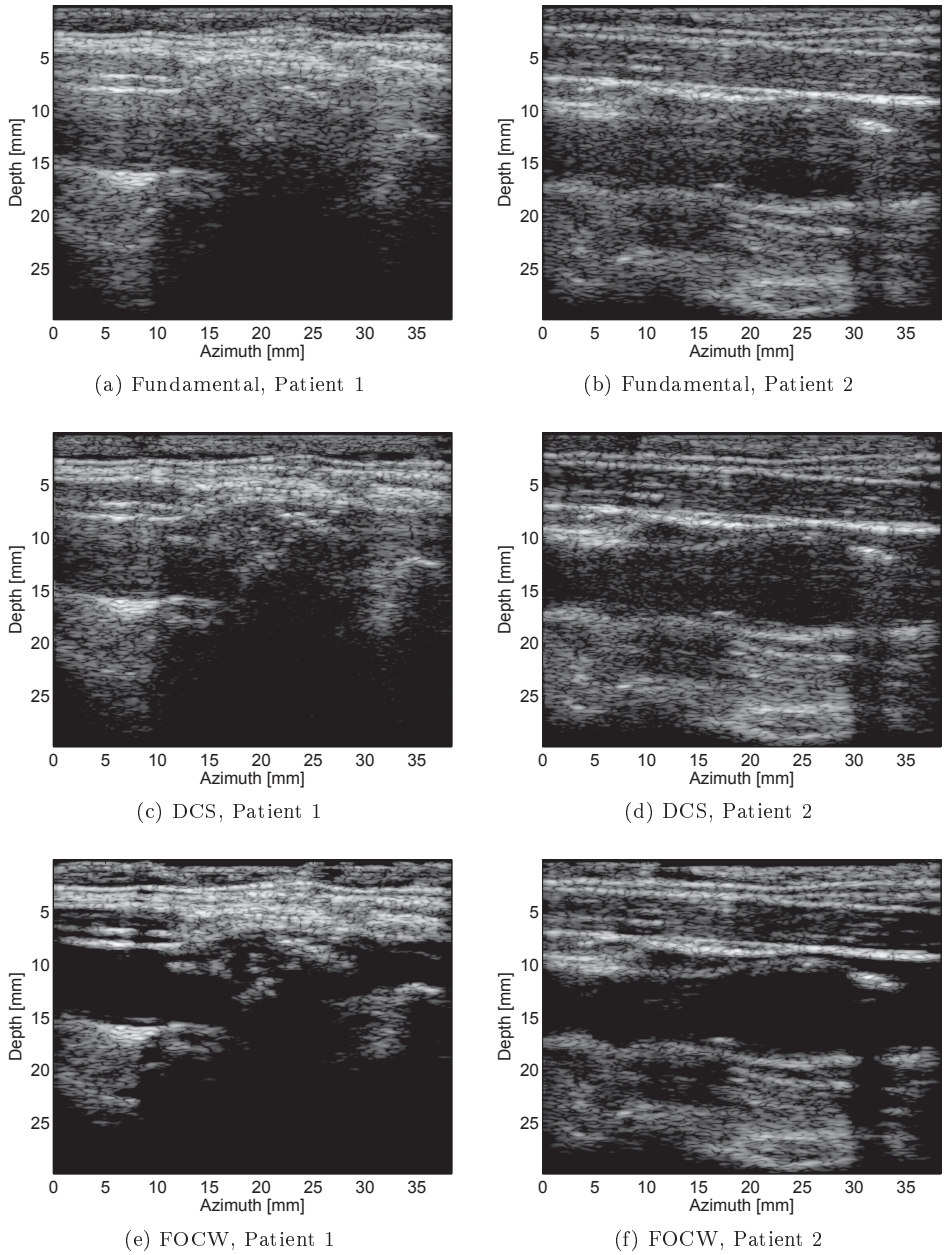


(a) Fundamental, Patient 1

(b) Fundamental, Patient 2

(c) DCS, Patient 1

(d) DCS, Patient 2

(e) FOCW, Patient 1

(f) FOCW, Patient 2

Figure C.10: *In vivo* images of two patients, processed as fundamental, DCS and FOCW images processed equally for both patients. Dynamic range 60 dB.

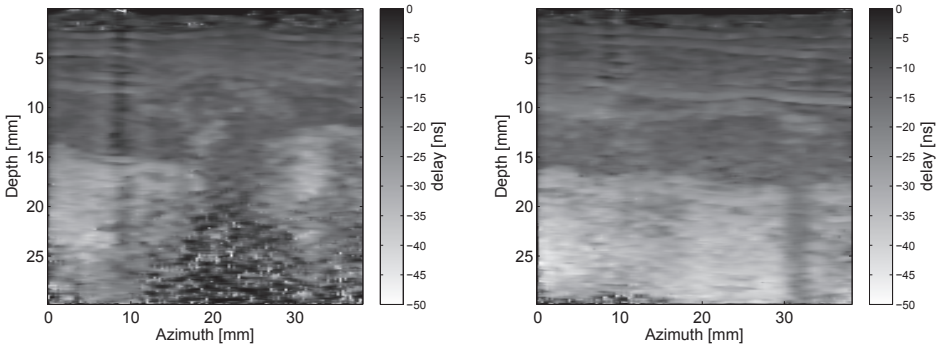


(a) Patient 1 (b) Patient 2

Figure C.11: Estimated delays for the two patients.

## C.5 Discussion

Delay estimates play a key role in the two novel algorithms presented in this article. Most important for both algorithms is the estimation of a correct first order delay, $\hat{\tau}_\mathrm{f}$, which for echo data builds on a good signal delay estimate $\hat{\tau}_\mathrm{y}$. In the case of carotid artery imaging it is possible to use strong scatterers at some depths to obtain a good estimate of $\tau_\mathrm{f}$ as could be shown in simulation here (Fig. C.8c). Judging from the results of the algorithms on the *in vivo* images this also seems to work well there. To find $\hat{\tau}_\mathrm{f}$ will not be as easy in a situation where the imaging scene does not contain strong scatterers in different depths. However, it may be questioned how much reverberations and multiple scattering is observed in that case. Another option might be to estimate the delay development in a homogeneous phantom and use it as an a priori estimate.

Another aspect on delay estimates is that it is difficult to estimate an instant or local delay. Delay estimates always work on a certain window and the window length might introduce averaging effects. This will directly affect the FOCW method, where $\hat{\tau}_\mathrm{y}$ is utilized in the weighting function.

The applied algorithms work on homogeneous and heterogeneous simulation data as well as *in vivo* data. However, the estimate of the water tank experiment is very rough between the scatterers and estimating $\tau_\mathrm{f}$ from the echo data is not possible without knowledge of the imaged geometry. This is due to the low signal between the scatterers which consists of numerical noise, only. The delay estimate in the lower central part of the *in vivo* delay image in Fig. C.11a is noise as well since most of the acoustic signal is absorbed by the plaque and the electronic noise disturbs the delay estimate.

DSC cancels one reverberation with another. In (simplified) theory this should totally remove class I/II reverberation pairs. The derivation of the DCS method makes several assumptions, which will be discussed in the following paragraphs.

First, a linear delay accumulation, which is achievable with suitable beamforming (Fig. C.8b).

Second, equal transmit and receive beams, which is achievable but might not be desirable in all cases. This seems to be a trade-off between reverberation noise suppression on one side and spatial resolution, signal to noise ratio and maximum penetration depth on the other side. Even though the initial results presented here show that DCS in general performs better with an equal transmit and receive beam (Tab. C.3, Tab. C.4, Fig. C.9) it still achieves a substantial improvement with a dynamic receive beam.

DCS will work well if, as a third assumption, the reverberations mainly consist of third order reverberations with the transducer as second reverberator. From both simulations and the *in vivo* examples here this seems to be a valid assumption, but might be challenging if a very strong deep reflector is insonified as for example a tissue-bone interface. In that case reverberations take the form of mirrored replica of tissue structures which is an indication that they are scattered solely between the hard surface and the surrounding tissue.

The fourth assumption is linear propagation and no different nonlinear distortion on the imaging pulse of the reverberation pairs to achieve the same pulse form of class I and II reverberations. This assumption may become difficult to fulfill if a certain penetration depth requires a certain transmit pressure and causes nonlinear self-distortion. The manipulation pulse will cause additional deformation and distortion.

Since DCS cancels the reverberations, the first order signal should appear close to unchanged with all texture and its own speckle pattern.

The FOCW algorithm makes less demands on similar pulses for both inversely manipulated pulses and matching reverberation pairs. Thus it should be more robust also when it comes to different transmit and receive beams. However, the simulation results here are ambiguous (Tab. C.3, Tab. C.4) and should be investigated further.

The FOCW algorithm yields appealing images since it combines the sharpness of the weighted fundamental image with the dynamic range of the weighting function. The spatial resolution of the weighting function will be limited by the window length of the delay estimation.

FOCW will not reveal the speckle pattern of the first order signal, since the reverberation signal is not removed but only weighted to the signal level. Thus, combining FOCW and speckle tracking will most certainly fail. However, tracking of bigger objects, *f.ex.,* vessel or heart wall tracking might be improved. FOCW improves the delineation of objects with a scattering border, even though this border might be covered by noise (compare Fig. C.10a, Fig. C.10e).

While this article uses $\hat{\tau}_\mathrm{r} = \hat{\tau}_\mathrm{f}(z/2)$, $\hat{\tau}_\mathrm{r}$ can be adjusted to to define a certain required first order signal content or the level of suppression.

Comparing DCS and FOCW it also becomes evident that DCS maintains more details and sharper edges, while FOCW yields higher contrast and stronger suppression. Common for both methods it that the two-pulse scheme decreases the frame rate by 50 percent compared to fundamental imaging.

In the following paragraphs some comments to the example lines and images are made. The subtraction method is presented together with DCS and FOCW for com-

parison. It is outperformed by DCS in all presented quantitative measures as well as by visual inspection in the simulation imaging lines, especially for the case of equal transmit and receive beam. The theoretical gain compensation works well for the DCS method, while it still leaves a dark nearfield for the SUB method.

Examining the performance of the three methods in the plane-point and the heterogeneous simulation around the focal spot reveals that the performance of the SUB method is nearly independent of the receive beam setup. The DCS method yields, as expected, higher suppression for the case of equal transmit and receive beam. The reverberations at 16 mm and 29 mm are attenuated stronger for the dynamic receive case in the plane-point simulation. The results for FOCW is mixed. In the plane-point simulation, it performs better in more cases for equal beams, while for the heterogeneous simulation it yields better results for the dynamic receive case.

For the *in vivo* images, a stripe artifact is observed on the left side of the images (Fig. C.10c, C.10e) and also in the delay image (Fig. C.11a). This is due to a malfunctioning element on the low frequency array of the applied transducer. It is compensated for in the processing, which works well for patient 2 and DCS in patient 1 but becomes visible in FOCW in patient 1.

FOCW removes structures in the shadow of the strong reflecting structure (30–32 mm, probably a calcification) in the artery wall in Fig. C.10f. Without knowing the ground truth it is not possible to make a definitive judgement if those echoes should be there or not. For the same reason, the unknown anatomical structure of the imaging scene, it is impossible as well to tell if Fig. C.10c or C.10e is more realistic in terms of contour and speckle texture of the plaque. This should be investigated in further simulation studies.

In general, FOCW does not suppress first order signal, according to Eq. (C.22). However, the estimation window of $\hat{\tau}_\mathrm{y}$ smooths the estimate and might lead to undesired suppression, even though it has not been observed yet.

## C.6 Conclusion

Two different methods for DBI reverberation suppression have been presented together with initial examples of their performance on both simulation and *in vivo* data. The delay corrected subtraction method is conservative with regard to image details and ideally should reveal speckle noise of the first order signal. The first order content weighting method utilizes a first order echo estimate to attenuate regions with a low signal to reverberation ratio. It yields high attenuation and should from theory be less susceptible to pulse form distortion than DCS. Both methods require a stable delay estimate. The methods should be evaluated further in *in silico*, *in vitro* and *in vivo* studies to assess suppression levels, preservation of details and clinical value. A real-time implementation should be pursued.

## Acknowledgement

Torbjørn Dahl, Department of Surgery, section of vascular surgery, St. Olavs Hospital, Trondheim, Norway, is acknowledged for acquisition of the *in vivo* images used in this article. Øyvind Krøvel-Velle Standal, Halvard Kaupang and Tonni F. Johansen are acknowledged for valuable discussions and support.

## Bibliography

[1] G. Kossoff, "Basic physics and imaging characteristics of ultrasound," *World J Surg*, vol. 24, no. 2, pp. 134–142, 2000.

[2] M. K. Feldman, S. Katyal, and M. S. Blackwood, "US artifacts," *Radiographics*, vol. 29, no. 4, pp. 1179–1189, Jul. 2009.

[3] J. A. Baker, M. S. Soo, and E. L. Rosen, "Artifacts and pitfalls in sonographic imaging of the breast," *AJR Am J Roentgenol*, vol. 176, no. 5, pp. 1261–1266, May 2001.

[4] M. Averkiou, D. Roundhill, and J. Powers, "A new imaging technique based on the nonlinear properties of tissues," in *Proc IEEE Ultrason Symp*, vol. 2, Oct. 1997, pp. 1561 –1566 vol.2.

[5] B. Ward, A. C. Baker, and V. F. Humphrey, "Nonlinear propagation applied to the improvement of resolution in diagnostic medical ultrasound," *J Acoust Soc Am*, vol. 101, no. 1, pp. 143–154, 1997.

[6] S. Choudhry, B. Gorman, J. W. Charboneau, D. J. Tradup, R. J. Beck, J. M. Kofler, and D. S. Groth, "Comparison of tissue harmonic imaging with conventional US in abdominal disease," *Radiographics*, vol. 20, no. 4, pp. 1127–1135, Jul. 2000.

[7] F. A. Duck, "Nonlinear acoustics in diagnostic ultrasound," *Ultrasound Med Biol*, vol. 28, no. 1, pp. 1–18, Jan. 2002.

[8] M. Averkiou, "Tissue harmonic imaging," in *Proc IEEE Ultrason Symp*, vol. 2, Oct. 2000, pp. 1563 –1572 vol.2.

[9] J. D. Thomas and D. N. Rubin, "Tissue harmonic imaging: Why does it work?" *J Am Soc Echocardiogr*, vol. 11, no. 8, pp. 803–808, Aug. 1998.

[10] H. Høilund-Kaupang, "Models and methods for investigation of reverberations in nonlinear ultrasound imaging," Ph.D. dissertation, Norges teknisk-naturvitenskapelige universitet, 2011. [Online]. Available: http://ntnu.diva-portal.org/smash/record.jsf?pid=diva2:479070

[11] C. Yen, H. Chang, S. Huang, Y. Huang, and C. Jeng, "Combination of tissue harmonic sonography, real-time spatial compound sonography and adaptive image processing technique for the detection of carotid plaques and intima-medial thickness," *Eur J Radiol*, vol. 71, no. 1, pp. 11–16, Jul. 2009.

[12] M. A. Lediju, G. E. Trahey, B. C. Byram, and J. J. Dahl, "Short-lag spatial coherence of backscattered echoes: imaging characteristics," *IEEE Trans Ultrason Ferroelectr Freq Control*, vol. 58, no. 7, pp. 1377–1388, Jul. 2011.

[13] R. H. Behler, M. R. Scola, and C. M. Gallippi, "Reverberation artifact rejection and masking in arterial ARFI imaging," in *Proc IEEE Ultrason Symp.* IEEE, Sep. 2009, pp. 2367–2370.

[14] S. P. Näsholm, R. Hansen, S. Måsøy, T. Johansen, and B. A. Angelsen, "Transmit beams adapted to reverberation noise suppression using dual-frequency SURF imaging," *IEEE Trans Ultrason Ferroelectr Freq Control*, vol. 56, no. 10, pp. 2124–2133, Oct. 2009.

[15] R. Hansen, S. Måsøy, T. F. Johansen, and B. A. Angelsen, "Utilizing dual frequency band transmit pulse complexes in medical ultrasound imaging," *J Acoust Soc Am*, vol. 127, no. 1, p. 579, 2010.

[16] S. P. Näsholm, R. Hansen, and B. A. Angelsen, "Post-processing enhancement of reverberation-noise suppression in dual-frequency SURF imaging," *IEEE Trans Ultrason Ferroelectr Freq Control*, vol. 58, no. 2, pp. 338–348, Feb. 2011.

[17] B. B. Goldberg, J.-B. Liu, and F. Forsberg, "Ultrasound contrast agents: A review," *Ultrasound Med Biol*, vol. 20, no. 4, pp. 319–333, 1994.

[18] C. X. Deng, F. L. Lizzi, A. Kalisz, A. Rosado, R. H. Silverman, and D. J. Coleman, "Study of ultrasonic contrast agents using a dual-frequency band technique," *Ultrasound Med Biol*, vol. 26, no. 5, pp. 819–831, Jun. 2000.

[19] A. Bouakaz, M. Versluis, J. Borsboom, and N. de Jong, "Radial modulation of microbubbles for ultrasound contrast imaging," *IEEE Trans Ultrason Ferroelectr Freq Control*, vol. 54, no. 11, pp. 2283 –2290, Nov. 2007.

[20] S. E. Måsøy, Ø. Standal, P. Näsholm, T. F. Johansen, B. Angelsen, and R. Hansen, "SURF imaging: In vivo demonstration of an ultrasound contrast agent detection technique," *IEEE Trans Ultrason Ferroelectr Freq Control*, vol. 55, no. 5, pp. 1112–1121, May 2008.

[21] R. Hansen and B. A. Angelsen, "SURF imaging for contrast agent detection," *IEEE Trans Ultrason Ferroelectr Freq Control*, vol. 56, no. 2, pp. 280–290, Feb. 2009.

[22] R. Hansen, S. Måsøy, T. A. Tangen, and B. A. Angelsen, "Nonlinear propagation delay and pulse distortion resulting from dual frequency band transmit pulse complexes," *J Acoust Soc Am*, vol. 129, no. 2, p. 1117, 2011.

[23] Ø. Standal, T. Tangen, and B. Angelsen, "P2D-4 a phase based approach for estimation and tracking of locally variable delays," in *Proc IEEE Ultrason Symp*, 2007, pp. 1583–1585.

[24] T. Varslot and G. Taraldsen, "Computer simulation of forward wave propagation in soft tissue," *IEEE Trans Ultrason Ferroelectr Freq Control*, vol. 52, no. 9, pp. 1473 –1482, Sep. 2005.

[25] T. Varslot and S.-E. Måsøy, "Forward propagation of acoustic pressure pulses in 3D soft biological tissue," *Modeling, Identification and Control*, vol. 27, no. 3, pp. 181–200, 2006.

[26] M. Frijlink, H. Kaupang, T. Varslot, and S.-E. Masoy, "Abersim: A simulation program for 3D nonlinear acoustic wave propagation for arbitrary pulses and arbitrary transducer geometries," in *Proc IEEE Ultrason Symp*, Nov. 2008, pp. 1282 –1285.

Paper D

# Image Contrast in Carotid Artery Images for Fundamental, Harmonic and Dual Band Imaging

Jochen M. Rau[1], Torbjørn Dahl[1,4] Rune Hansen[1,3], Thor Andreas Tangen[2], Øyvind Krøvel-Velle Standal[1], Tonni F. Johansen[1], Bjørn Angelsen[1] and Svein-Erik Måsøy[1]

[1]Department of Circulation and Medical Imaging, NTNU, Trondheim, Norway,
[2]Department of Engineering Cybernetics, NTNU, Trondheim, Norway,
[3]SINTEF Society and Health, Trondheim Norway
[4]Department of Surgery, Section of Vascular Surgery, St. Olavs Hospital, Trondheim, Norway

**Abstract**

Ultrasound image contrast in carotid artery imaging is impaired by clutter. Harmonic imaging (HI) and dual frequency band imaging (DBI) with overlapping pulses are supposed to show less clutter than fundamental imaging (FI). This study compares image contrast provided by these methods as a measure for clutter suppression. A group of 22 patients was examined. The median image contrast improvement of HI recordings compared with their corresponding fundamental image is 3 dB while it is 13 dB for DBI. In addition, a sub-group of recordings with well corresponding image planes between the different methods, including 76 recordings from 19 patients, was analyzed separately. Here the median improvement was 3.5 dB for HI and 15 dB for DBI. Thus both methods improve image contrast compared to FI with DBI being superior.

This paper is being prepared for submission to Ultrasonics

## D.1 Introduction

Stroke and other cerebrovascular diseases are the number two causes of death worldwide [1]. Stroke is also a leading cause of morbidity. Carotid artery disease is a well-established risk factor for ischemic stroke [2, 3].

Atherosclerosis is a disease thought to begin shortly after birth. Through the years, plaques can grow slowly with various morphologic aspects and properties [4]. The plaque composition (fibrotic, lipidic, or calcified), its shape, and the stage of development are important factors for determining the risk of plaque rupture [5, 6]. Although atherosclerosis may affect the intracranial vessels themselves, 88% of patients with amaurosis fugax or hemispheric transient ischemic attacks (TIA's) have atherosclerotic disease in the carotid bifurcation [7].

Today, the evaluation of atherosclerosis in the carotid artery is mainly performed with ultrasound. The evaluation often comprises one ore more of the following examinations: a subjective analysis based on image findings to assess the general level of atherosclerosis in a patient, measuring the IMT for quantitative assessment, or to evaluate specific plaques for the possibility of surgical removal of the plaque.

In this context achieving the best image quality possible is crucial. However the basic assumptions which ultrasound imaging is built upon are not always true, and in case they are violated, image quality is deteriorated. One of these assumptions is the Borne approximation which states that the transmitted ultrasound pulse is only reflected once from tissue structures inside the body before it is received by the transducer. In reality, ultrasound waves are scattered or reflected several times between structures and the transducer and are a major source of clutter. This is termed higher order scattering, multiple scattering or reverberations.

This unwanted scattering adds to the image as noise and deteriorate contrast resolution in the image. Reverberations are very common in carotid artery imaging, and particularly in the bifurcation where the most significant plaques are found. Obscuring reverberations could be fatal if the gathered images are used to assess if a plaque is stable or is at risk to rupture, *f.ex.,* with an echolucency assessment [8].

The number of imaging methods which can be applied to suppress reverberation clutter is limited. Well known and often used in clinical practice is harmonic imaging, applied in amongst others cardiac and abdominal imaging. However it is not that frequently used in carotid artery imaging. More recently dual frequency band imaging (DBI) [9–11], acoustic radiation force impulse (ARFI) imaging [12] and short-lag spatial coherence imaging [13] were proposed as methods for suppressing reverberation clutter but are not yet present in clinical practice.

The goal of this study is to compare the image contrast of two methods, harmonic and dual frequency band imaging in carotid artery imaging in a clinical setting. Image contrast of each method compared to a corresponding fundamental image is used as a measure for the methods' performance to suppress reverberation clutter. The study was approved by the local ethics committee and the patients recruited for this study provided signed informed consent.

## D.2 Materials and Methods

### D.2.1 Imaging methods

In this study three imaging methods were applied: Fundamental imaging, harmonic imaging, and dual frequency band imaging.

Fundamental imaging (FI) is built on the assumption that there are no reverberations present and all received signal originates from first order scattering. FI is widely used in clinical practice for carotid artery imaging and is in this study used as a baseline method for the comparison of the image contrast of the other methods.

In harmonic imaging (HI) an ultrasound beam is transmitted into the tissue and, due to the nonlinear properties of tissue, higher harmonic frequencies build up accumulatively during propagation. The receive signal is filtered for the harmonic content or isolated in subtraction methods using pulse inversion imaging. It is less susceptible to reverberation clutter as the harmonic beam is low close to the ultrasound probe surface, thereby reducing the impact of multiple reflections between tissue structures and the ultrasound probe occurring close to the probe surface. HI has been shown to reduce reverberation clutter in a range of clinical applications such as cardiac [14, 15], liver [16–18], abdominal [16, 17, 19], obstetrics [17, 18, 20], small parts [18], and carotid imaging [21].

Often spatial compounding (cross-beam) is combined with FI as well as HI. In spatial compounding several images are taken at different angles and then superimposed. This enhances border delineation and reduces speckle variations.

In dual frequency band imaging (DBI), dual frequency band ultrasound pulse complexes are transmitted into the tissue. The pulse complex consists of a low-frequency (LF) manipulation pulse and a high-frequency (HF) imaging pulse overlapping in time and space, where the purpose of the LF pulse is to manipulate both propagation and scattering of the HF imaging pulse in tissue [9, 10, 22–26]. This can be utilized to reduce the impact of reverberation clutter [10, 11].

### D.2.2 Patients and ultrasound recordings

Twenty four patients have been recruited consecutively from the vascular surgery day clinic at five different days of planned examinations. Two were excluded from the analysis due to technical problems with the recordings, otherwise no exclusion criteria has been used. Of the remaining 22 patients, 10 were women and 12 men. Age parameters were calculated using 21 patients as this parameter was not recorded for 1 patient. The minimum, median and maximum age was 24, 68, and 82 years respectively. In 18 of the 21 patients, the minimum, median and maximum age was 62, 70, and 82 years respectively. The three remaining were aged 24, 28, and 45 years, which was unusual for this population.

Harmonic imaging was performed on state-of-the-art scanners. The first 13 patients were imaged with a a GE Vivid E9 scanner (GE Vingmed Ultrasound, Horten, Norway). However, this scanner became unavailable during the study, so a a GE Logiq E9 scanner (GE Health Care, Milwaukee, USA) had to be used for the remaining pa-

Table D.1: Scanner, probe setup and HI recording modes for the different patients in the study. Patient 6 and 7 were not included in the final analysis due to technical problems with the recordings.

| Patient | DBI probe | GE scanner | GE probe | HI modes |
|---|---|---|---|---|
| 1–5 | Viglen | Vivid E9 | 11L | HI |
| 6,7 | – | – | – | – |
| 8–13 | Vora | Vivid E9 | 9L | HI |
| 14–18 | Vora | Logiq E9 | M6-15 | HI+HIC |
| 19–24 | Vora | Logiq E9 | 9L | HI+HIC |

tients, instead. Different linear array probes were used for different patients. On the GE Vivid E9 scanner both a 9L and a 11L probe were used, and for the GE Logiq E9 scanner, both a 9L and a ML6-15 probe were used. The combination of scanner and probe is given in Tab. D.1 for each patient.

Two reasons render utilizing the same scanner with the same probe for HI and DBI impossible. First, the scanner and its software have to be modified for the system to be able to do DBI. Second, the current prototype dual frequency probes have limited bandwidth on each of the bands which does not allow for doing HI and DBI with the same probe.

Therefore, for dual frequency band imaging a modified Ultrasonix Sonix RP (Ultrasonix, Vancouver, Canada) scanner was used, which further on in the article will be denoted as the *DBI scanner*. The DBI scanner was used together with two different DBI linear array probes: A 0.9/6.5 MHz (LF/HF) probe and a 0.8/8.0 MHz named Viglen and Vora respectively. The reason for using two different probes was that a probe development project was completed with an improved DBI probe designed specifically for carotid artery imaging. This probe (Vora) was then introduced in the study. The Viglen probe was originally designed for shallow abdominal imaging, but has also been used in carotid artery imaging.

Fundamental imaging was performed on the respective scanners to have a system related baseline. This way, even if different systems are used, comparable contrast measurements can be acquired for both, the DBI and the HI platform.

The DBI scanner does not allow for compounding nor other means for speckle reduction, so these features were also disabled in the GE scanners for better comparison. However in the second half of the study in addition to HI also HI with spatial compounding (HIC) was assessed on the GE scanners in 20 recordings on 11 patients to investigate if the image contrast is affected by spatial compounding. One single transmit focus was used on all scanners.

Table D.1 presents an overview on which patients the different probes and scanners were used.

The scanning of the patients was performed by an experienced vascular surgeon (Torbjørn Dahl, MD, PhD, Head of Section), at The Department of Surgery, Section

of Vascular Surgery, St. Olavs University Hospital, Trondheim, Norway. For the study, two recordings were made at the carotid bifurcation on both sides of the patient. First, a recording of 2 seconds was performed in the FI mode. The mode was then switched to HI, while the probe was held still, and a recording of 2 seconds was stored. The total time of these two recordings was approximately 6-7 seconds. In addition HIC was recorded for patient 14-24 which took the same amount of time as the HI recording. Then using the DBI scanner, the surgeon placed the DBI probe at the same location aiming to achieve the same image plane as in the HI recording, which was displayed on the E9 scanner. Approximately 2-3 seconds were recorded. The whole procedure took approximately 4 minutes in total and was performed after conventional diagnosis.

### D.2.3 Data analysis

As the images are in similar but not in the exact same planes between the separate recordings with the two platforms (GE scanners vs DBI scanner), it was visually assessed if the images were well aligned and comparable or not. The data analysis was carried out both on the sub-group of images which corresponded well between the two platforms later on termed as *corresponding recordings*, and on all the images separately.

Suppression of reverberations should lead to an increase in local image contrast as hypoechoic areas are covered by distinct or distributed reverberations. In carotid artery imaging, the lumen of the blood vessel should appear hypoechoic based on the weak scattering from blood compared to tissue. The artery wall is usually a quite strong reflector with a high level of first order signal compared to reverberations, which are of a higher order. As reverberation clutter is decaying in the radial direction within the lumen, the proximal wall should yield a lower ratio between first-order signal and reverberations than the distal wall.

The analysis was based on this rationale: In the fundamental image a location within the lumen was chosen with an emphasis on visible reverberations. At this location a circular region of interest (ROI) was placed. The diameter of the ROI was adjusted such that it covered the lumen with a small margin to visible structures as the intima or plaque. Then, an elliptical ROI of the same size in the horizontal axis and 1 mm in height was placed inside the distal wall below the circular ROI. As this ROI is sometimes sensitive to speckle variations it was moved around with a small displacement to find the location with strongest signal (*cf.* Fig. D.1 for an example of placed ROIs). The ratio of the mean of the signal within the two ROIs is considered to be the local image contrast.

Quantification of contrast improvement within an image on the GE scanners was performed using a Q-analysis tool available on the scanners. This was first done on both the E9 fundamental and harmonic images consecutively. It was not possible to place the ROI in the exact same location between the images, and this was done by visual inspection.

All DBI images were re-processed after the clinical recordings using in-house software written for Matlab (Mathworks, Natick, U.S.A.). This was possible since the Ultrasonix Sonix RP platform is equipped with a research module allowing the stor-

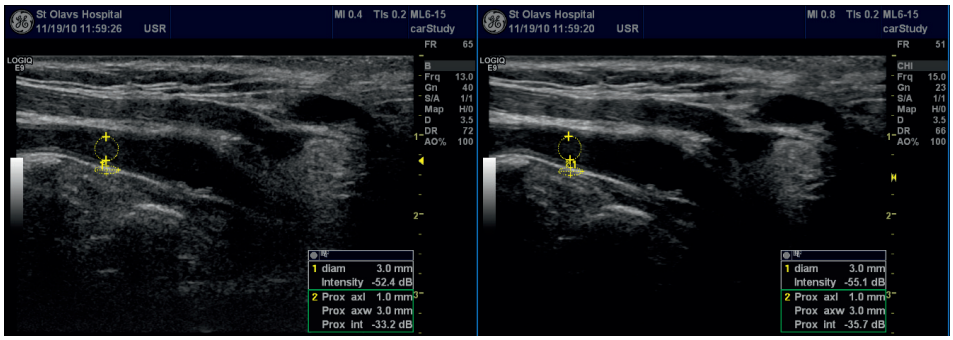


(a) Logiq E9, ML6-15. Left pane FI, right pane HI

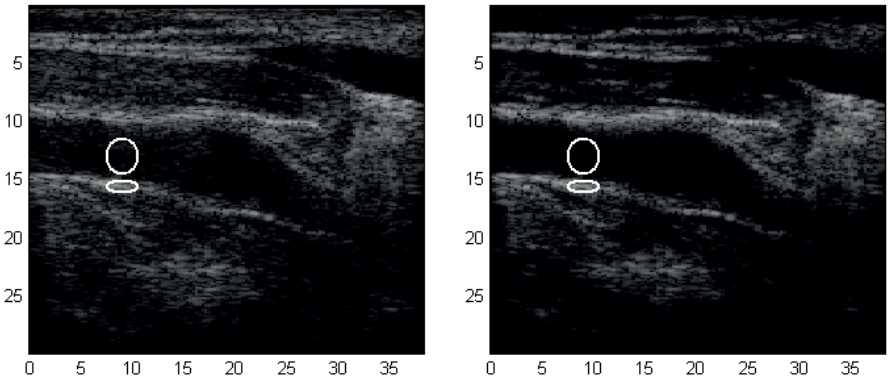


(b) DBI, Vora. Left pane FI, right pane DBI

Figure D.1: Patient 18, example with visible ROIs

age of unprocessed beamformed RF data. For the DBI scanner, the conventional fundamental BMode image and the corresponding DBI image are both processed from the same recording, allowing for comparison of image contrast improvement in the exact same location of the same recording at the same point in time. Also the ROIs are placed on the exact same position. This allows for a true comparison of image contrast improvement between FI and DBI on this scanner.

For a DBI recording that corresponded well with one of the GE fundamental and harmonic images, the ROIs were placed first in the GE images and then on the same locations in the DBI images by visual comparison. The same ROI size and geometric shapes were used for DBI as for HI and FI recordings on the GE scanners.

In the in-house software the mean value of signal intensity inside the ROI was calculated in the linear regime, that is prior to log compression, and then the average intensity was transformed to decibels as

$$\overline{I}_{\mathrm{ROI,dB}} = 10 * \log_{10}\left[\overline{I}_{\mathrm{ROI}}\right] \ , \tag{D.1}$$

where $\overline{I}$ denotes average intensity. To the author's knowledge, this is also what is done in the Q-analysis software on the GE scanners.

The intensity within the ROI in the lumen $\overline{I}_{lumen,dB}$ and within the ROI in the distal wall $\overline{I}_{wall,dB}$ define the local image contrast to:

$$C = \overline{I}_{\text{wall, dB}} - \overline{I}_{\text{lumen, dB}} \tag{D.2}$$

The resulting contrast improvement of the different methods is plotted as a scatter-plot with the FI contrast as the abscissa (cf. Fig. D.2 ). The improvement or contrast increase is hereby defined as

$$C_I = C_X - C_{FI} \tag{D.3}$$

where $C_I$ is the image contrast increase, $C_{FI}$ the contrast in the fundamental image and $C_X$ the contrast measured in the corresponding image for one of the methods HI, HIC and DBI. In case of multiple observations on the same position the symbol changes according to the legend in the plot. Beyond giving a visual impression of the observations, a potential dependence of the improvement on the FI contrast should become visible in this plot. In other words, it should be possible to see if images with low contrast are improved differently than images with high contrast. The median of the recordings with the different methods is plotted as a dashed line over the whole FI range.

For the recordings where direct comparison is considered feasible, the contrast increase with the DBI method is plotted against the contrast increase in the corresponding HI recording (cf. Fig. D.2 right pane). In such a plot it is possible to assess if data which improves well in HI improves differently with DBI. A line marking equal improvement by both methods is provided for reference.

Box-Whisker plots are used to represent the distribution of the observations without assuming a certain random distribution (as *e. g.* the normal distribution). The whiskers span from the minimum to the maximum value, while the box spans from the end of the lower quartile to the beginning of the upper quartile. The bar marks the median of the data. The data is grouped by method and/or scanner (*cf.* Fig. D.3 ).

Finally an analysis of the achieved FI contrast of the different platforms is carried out. This is done to assess and compare if both platforms yield the same FI contrast. Here, the E9 scanners are grouped together.

To evaluate the statistical significance two different types of tests are used. In order to test if the median values are significantly different from zero, a two-sided Wilcoxon signed rank test is used with the 0-hypothesis "The median contrast improvement for the method is zero". This hypothesis will be considered as rejected if the p-value is below 0.05. The same test is used to assess the difference in the median values for the corresponding recordings (which is a paired dataset) with the 0-hypothesis: "The median contrast improvement for the two compared methods is equal". For all recordings a Wilcoxon rank sum test is used to assess the difference between the median of the two methods. The Wilcoxon tests are favored over standard t-tests as they do not make any assumptions on the statistical distribution.

Table D.2: Overview over the number of recordings taken for the different imaging methods and the number of patients included.

| | | E9 scanner | | | DBI scanner | |
|---|---|---|---|---|---|---|
| | # patients | FI | HI | HIC | FI | DBI |
| all recordings | 22 | 41 | 41 | 20 | 61 | 61 |
| corresponding recordings | 19 | 38 | 38 | – | 38 | 38 |

Table D.3: Overview over statistical properties of the local contrast data from the *corresponding recordings*. All values in decibels.

| | HI vs FI | | | DBI vs FI | | |
|---|---|---|---|---|---|---|
| | FI | HI | contrast increase | FI | DBI | contrast increase |
| min | -1 | 8 | -2 | 2 | 9 | 6 |
| **median** | **18.0** | **19.5** | **3.5** | **14.0** | **27.0** | **15.0** |
| max | 31 | 36 | 11 | 36 | 43 | 26 |
| n | 38 | 38 | 38 | 38 | 38 | 38 |

## D.3 Results

A total of 122 recordings, thereof 61 (FI, DBI) on the DBI scanner and 61 (FI, HI, HIC) on the GE scanners were captured from 22 patients. The *corresponding recordings* comprised 38 recordings from each platform, that is a total of 76 recordings from 19 patients (*cf.* Tab. D.2 ). As described in the previous section, the local image contrast was determined and compared.

The presentation of the results is divided in three parts, the results from the recordings with corresponding image planes, the results from all recordings and a section containing example images.

### D.3.1 Results from corresponding recordings

Table D.3 summarizes the results for the corresponding recordings. An increase in local contrast can be observed for both DBI and HI in most patients. For HI, the image contrast is sometimes lower than the contrast in the corresponding fundamental image, while DBI increases the contrast with a minimum of 6 dB over all the corresponding recordings. The median value of contrast improvement for DBI is 15.0 dB while HI yields 3.5 dB.

The individual observations are shown graphically in the left and middle pane of Fig. D.2 displaying contrast and contrast improvement compared to FI contrast. From this figure it can be seen that in four recordings, HI performs worse than FI. DBI contrast is above FI contrast in all cases. No clear dependence of the improvement on

the FI contrast can be observed for HI or DBI.

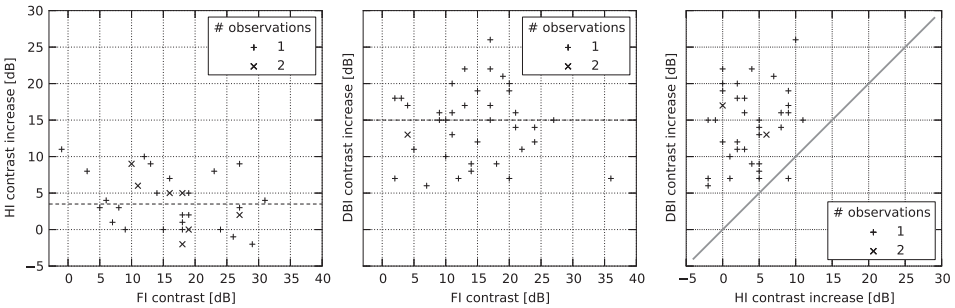


Figure D.2: Left and middle pane: Contrast improvement of HI (left) and DBI (middle) plotted vs. the respective FI contrast of the *corresponding recordings*. The median is plotted as horizontal dashed line. Right pane: DBI contrast improvement plotted against the HI improvement from the *corresponding recordings*. The gray line displays equal improvement of the two methods. For all panes: If a specific value is observed more than once, the value is given a different marker, and the number of observations provided in the legend

To test for statistical significance a number of hypothesis tests were conducted as described in the previous section above. Both methods proved to yield a median contrast increase which is significantly different from zero (DBI $p<0.001$; HI $p<0.001$). Also, the median difference between the two methods was significantly different ($p<0.001$).

In the right pane of Fig. D.2 HI and DBI improvement of the *corresponding recordings* are plotted against each other. The contrast increase of DBI was higher than the one for HI in 37 of the 38 recordings. The wide scattering indicates that the improvement of HI and DBI is not correlated with each other, i.e. high contrast increase in HI does not yield high contrast in DBI and vice versa.

In the left pane of Fig. D.3 a box whisker plot is presented for the corresponding recordings to show the distribution of observations. Half of the HI recordings show contrast improvements between 0 and 6dB. Correspondingly, half of the DBI recordings show contrast improvements between 6 and 18dB.

### D.3.2 Results from all recordings

The results from *all recordings* are summarized in Tab. D.4 and show only small changes compared to the result from the *corresponding recordings*. The median contrast improvement is 3.0 dB, 3.5 dB and 13 dB for HI, HIC and DBI respectively. This is is 0.5 and 2 dB lower compared to the *corresponding recordings* for HI and DBI respectively. The difference in median contrast of HI and HIC is 0.5 dB in favor for HIC.

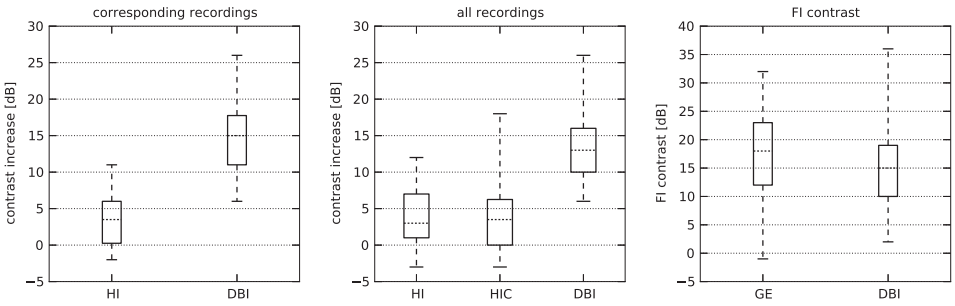


Figure D.3: Contrast improvement for DBI and HI in the *corresponding recordings* (left), DBI, HI and HIC in *all recordings* (middle). In the right pane the fundamental contrast for the two platforms in the study is depicted. The whiskers span from minimum to maximum, the box begins at the lower quartile and ends at the upper one, the line indicates the median.

Table D.4: Overview over statistical properties of the local contrast data from **all recordings**. All values in decibels.

| | HI vs FI | | | HIC vs FI | | | DBI vs FI | | |
|---|---|---|---|---|---|---|---|---|---|
| | FI | HI | contrast increase | FI | HIC | contrast increase | FI | DBI | contrast increase |
| min | -1 | 8 | -3 | -1 | 7 | -3 | 2 | 9 | 6 |
| **median** | **18** | **21** | **3.0** | **16** | **21** | **3.5** | **15** | **27** | **13.0** |
| max | 32 | 40 | 12 | 32 | 37 | 18 | 36 | 48 | 26 |
| n | 41 | 41 | 41 | 20 | 20 | 20 | 61 | 61 | 61 |

The individual observations are depicted in Fig. D.4 HI, HIC and DBI are in the left, middle and right plot of the figure respectively. The median value is given as horizontal line in each of the plots.

In the middle plot of Fig. D.3 the distribution of observations for HI, HIC and DBI is visualized for *all recordings*. Half of the observations for HI, HIC and DBI show 1 dB to 7 dB, 0 dB to 6.25 dB and 10 to 16 dB contrast increase respectively.

The statistical significance was tested. The median value of the contrast increase for all three methods is statistically significant different from 0 (Wilcoxon signed rank test; DBI: $p<0.001$, HI: $p<0.001$, HIC: $p=0.001$). The statistical significance of the median difference between the different methods was tested with a Wilcoxon rank sum test also rejecting the 0-hypothesis of equal medians for HI vs DBI ($p<0.001$) and HIC vs DBI ($p<0.001$) but not for HI vs HIC ($p=0.84$).

In the right plot in Fig. D.3 a comparison of local fundamental image contrast is presented in order to show the difference between the scanners used in this study. The

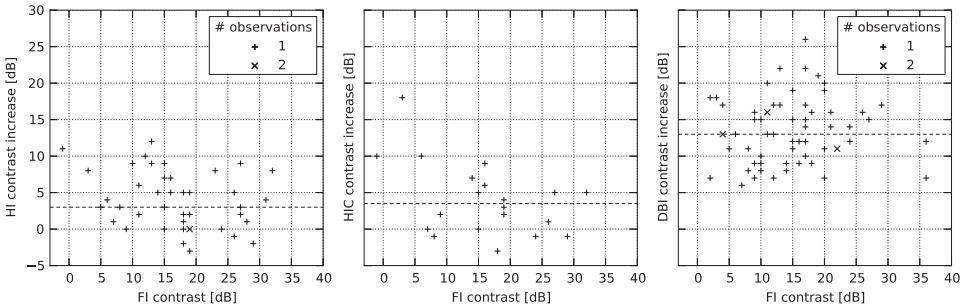


Figure D.4: Contrast increase for HI (left), HIC (middle) and DBI plotted vs. the respective FI contrast of *all recordings*. The median is plotted as dashed horizontal line. For all panes: If a specific value is observed more than once, the value is given a different marker, and the number of observations provided in the legend.

GE scanners yield a median FI contrast of 18 dB while the contrast for DBI scanner is 15 dB. Half of the observations lie within 12 dB to 23 dB for the GE scanners and 10 dB to 19 dB for the DBI scanner. Performing a Wilcoxon rank sum test to compare the median values yields a p=0.10 which is after the criteria in the methods section considered not to be statistically significant.

### D.3.3 Image examples

In this section, some image examples are presented. The fundamental and DBI images displayed have been processed to show the same gain and dynamic range, making them directly comparable. This was not possible using the GE scanners, and the images presented from these scanners have been manually gained approximately equal by visual inspection. This may lead to differences in visualization of reverberations in the images, which may be interpreted as significant. The quantification analysis is independent on gain settings on all scanners, and is therefore more accurate.

Figures D.5 and D.6 present the FI and HI as well as FI and DBI image for patient 9. This was a 66 year old woman and the scans are taken at the right side of the patient in the carotid bifurcation. The patient presented almost no plaque formation, and no plaque formation that was deemed clinically significant. As may be observed from Fig. D.5 there is little or no improvement of image quality comparing FI and HI for this patient, and this is also confirmed by a local contrast improvement measurement of 2 dB for this case.

Comparing the fundamental and DBI image from the DBI scanner, a strong increase in contrast is observed. The quantified contrast improvement between the images was here 18 dB. Notice the improvement in the image at the bifurcation, and the wall separating the internal and external carotid is clearly visible in the DBI image. This structure is not displayed well on the E9 scanner.

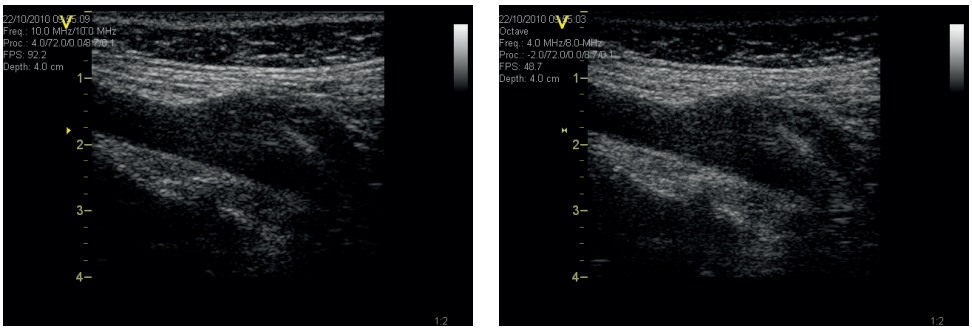

(a) (b)

Figure D.5: Patient 9, Vivid E9, 9L probe. Left pane FI, right pane HI. Woman aged 66 years.

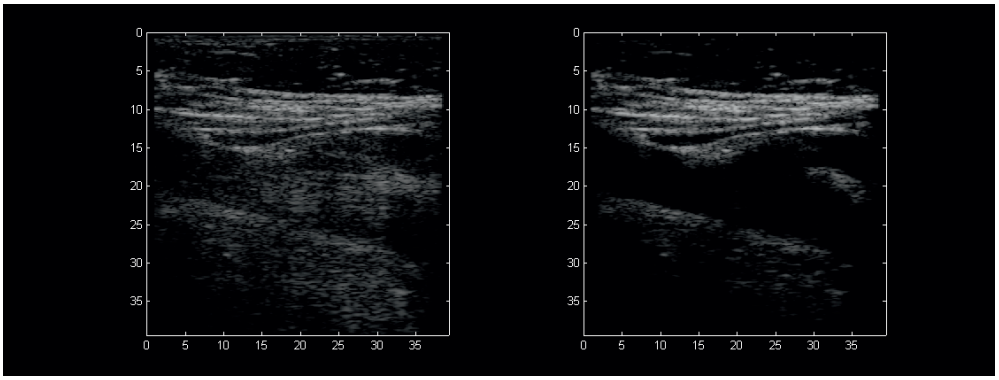


Figure D.6: Patient 9, DBI, Vora probe. Left pane FI, right pane DBI. Woman aged 66 years. Both x and y axis in mm.

In Figs. D.7 and D.8 images from patient 13 are presented. This was a man aged 76 years old with a clinically significant plaque in the left side carotid bifurcation. The plaque was diagnosed with PW Doppler to be an 80% stenosis, and thus qualified for surgery. Here, the improvement in image contrast between FI and HI on the GE scanner was 6 dB. Comparing the fundamental and DBI image on the DBI scanner, the contrast improvement was 13 dB.

Although this plaque is readily visible on both scanners due to its large size and location, the expected hypoechoic regions are significantly enhanced in the DBI image. From the quantification analysis there is a 7 dB difference between DBI and HI for this particular case, and the images appear quite different. This may be observed by the clear definition of the proximal carotid artery wall in the DBI image. The enhancement is not only visible in the carotid artery but also in hypo-echoic structures in the body wall proximal to the carotid artery.

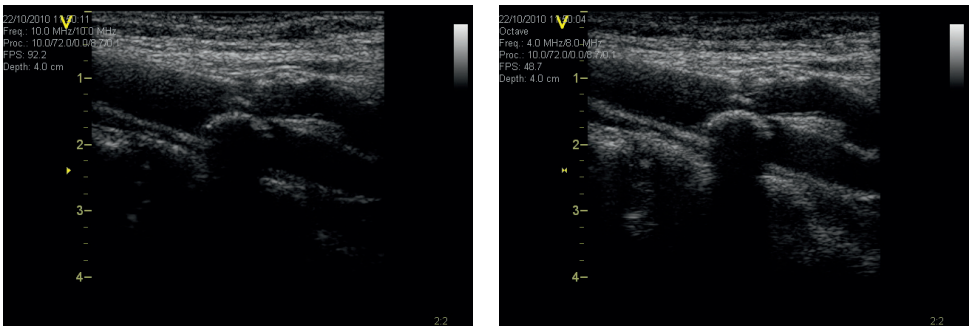

(a) (b)

Figure D.7: Patient 13, Vivid E9, 9L probe. Left pane FI, right pane HI. Man aged 76 years.

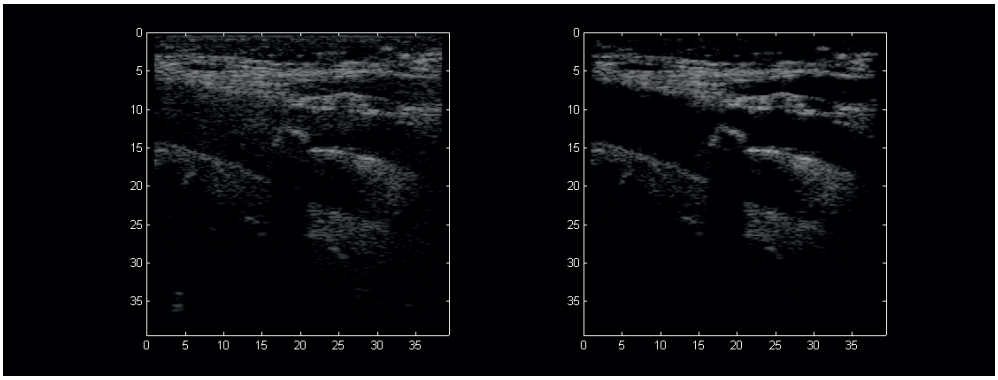


Figure D.8: Patient 13, DBI, Vora probe. Left pane FI, right pane DBI. Man aged 76 years. Both x and y axis in mm.

The DBI image also shows improved image contrast after the distal wall of the carotid, and a reverberation in the lower left corner (located at 35 mm depth) present in the fundamental image is removed in the DBI image.

In Fig. D.9 an image recorded in harmonic mode is compared with an image recorded with harmonic spatial compounding using the Logiq E9 scanner. This was a man aged 82 years with some plaque formation. The HIC image appears more smooth and exhibits less speckle compared to the harmonic image. Border delineation appears more clear and at the same time image details are visualized better. For this case there was a 3 dB improvement of local image contrast in the HIC image compared to the HI. There was no difference between FI and HI for this case.

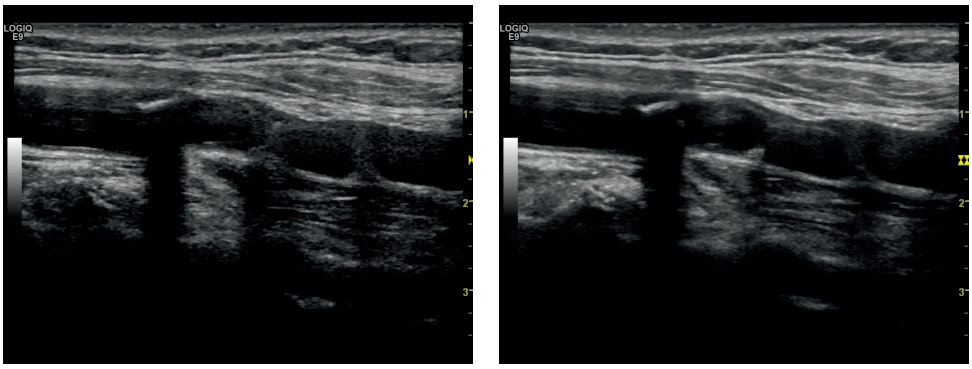

(a) (b)

Figure D.9: Patient 14, Logiq E9, ML6-15 probe. Left pane HI, right pane HIC. Man aged 82 years.

## D.4 Discussion

The results in this work suggest that DBI is capable of showing a significantly higher improvement of image contrast and thus better clutter and reverberation rejection in a clinical setting than HI is. The median image contrast improvement of DBI is 11.5 dB higher than the one for HI in 38 recordings from 19 patients of good correspondence in image location between the different scanners used. Comparing all recordings this difference is still 10.0 dB. This represents an improvement in image contrast of 3.8 and 3.2 times respectively.

Carotid artery imaging is an especially difficult case where harmonic imaging has shown some or little improvement [21]. In cardiac imaging the body wall is thin compared to the size of the ventricle. This is not the case for carotid artery imaging where the body wall is relatively thick. That is, the object to image is approximately of the same size or smaller than the body wall lying in front of it. Harmonic imaging faces a challenge here as reverberations which originate close to the transducer are suppressed the most (where no harmonic content is built up yet) while the ones which originate close to the object are marginally reduced (as they show nearly as much harmonic content as the echo from the object itself).

Comparing FI to HI is in this study performed by comparing local image contrast in a single location in two different recordings taken at two different times. Ideally, the comparison should have been made from recordings taken intermittently, fundamental and harmonic imaging in each second frame, as this would ensure imaging at approximately identical image planes. The authors did not have the possibility of making such recordings with the GE scanners used in this study. The difference in time between the two recordings was in the order of 2-3 seconds, the time it took to refill the image buffer after storing the first recording. This should at least minimize possible motion of the probe between the recordings. It was observed that in some

cases, the harmonic image plane had shifted somewhat compared to the fundamental one, which is evidence of motion of the probe between the recordings. This will impair the analysis as reverberations depend on the location of the probe.

For the FI and DBI comparison, as described earlier, the images are processed from the same data set. Also it was possible to place equally sized ROIs in the exact same location in both images making the comparison valid for all recordings.

Three different ultrasound scanners were used in this study, the DBI scanner (modified Ultrasonix Sonix RP scanner) was used for comparing FI and DBI, while a GE Vivid E9 and a GE Logiq E9 was used for comparing FI, HI and HIC imaging. The Ultrasonix RP scanner may due to its technical specifications be classified as a low-mid range scanner. It has 32 receive channels and 10 bit A/D-converters. The GE scanners may both be classified as high-end or premium scanners. Such scanners typically have between 128 and 256 receive channels and 12 or more bit A/D converters. This allows for much improved dynamic receive focusing, lower pitch probes with improved near-field focusing, and the A/D-converters will have a 4 times improved dynamic range. Thus the GE scanners should have a much better spatial resolution and dynamic range in the recorded images, and comparing spatial resolution in the images this is indeed the case. Particularly the ML6-15 probe, where the M indicates a subdivision of elements in the elevation direction of the probe, showed the best spatial image resolution.

There was too little data to compare the probes individually with statistical significant results. Therefore the results from the different probes used were grouped together on a scanner basis.

As the methods' contrast improvement is measured with the respective FI contrast as a reference, a bias in FI contrast would directly add to the method's performance. For equal performance of both HI (or HIC) and DBI this would favor the scanner with less FI contrast. The FI image contrast on the DBI scanner with the DBI probes is 3dB lower than the one on the GE scanners *cf.* Fig. D.3. The difference is not statistically significant, but there is a trend which may be explained by the rationale given above. Even if 3dB of the contrast increase of DBI would be attributed to the lower FI contrast it still would show a substantial 7dB higher increase than HI. Considering this, the authors think it is valid to compare the scanners and their image contrast in the way the study does. An additional aspect is that if the image contrast in the different scanners is comparable also the reverberation content in the images is not dependent on the scanners either.

In this study, harmonic imaging with spatial compounding did not have a significant effect on local image contrast compared to HI alone. In a study by Yen *et al.* [21], this feature showed improved image quality compared combined with HI to only using HI. Also, in a study by Kern *et al.* [27] it was shown that spatial compounding provided better characterization of carotid artery plaques compared to standard fundamental imaging. Note that both of these studies determined image improvement using a visual scoring of the images by observers, and did not quantify *e.g.* local image contrast as done here. The important effects of spatial compounding are speckle reduction, improved edge visualization (due to reduced effects of angular dependent scattering), and improved signal-to-noise ratio (SNR). All this will make the image appear better

to the user, but as demonstrated in this study, spatial compounding does not improve local image contrast quantitatively. This is contradictory to the visual scoring in [27], but a quantitative evaluation of image contrast should be more reliable.

From Fig. D.4, middle pane, it may be observed that one recording showed 18 dB local image contrast improvement comparing HIC to HI. Inspection of the images from this recording shows a shift in image location which might have impaired the image contrast comparison for this recording. The data is still included in the analysis.

The presented images show that DBI is less susceptible to reverberations with the first reflector at a distal location. In Fig. D.8 in the lower left corner a reverberation is visible in the FI image which stems from a structure within the distal wall of the carotid. This is generally not possible with harmonic imaging as this method suppress mainly reverberations originating close to the probe surface [14, 15, 17, 18]. This is also clearly shown in Fig. D.7 right pane, where a strong reverberation is observed on the left side on the image distal to the distal wall.

## D.5 Conclusions

Methods which are able to suppress reverberations well may potentially impact various analysis methods of carotid artery plaques based on ultrasound BMode image parameters, as *e.g.* echolucency of the plaque, intima-media measurements in the proximal carotid artery wall, clinical evaluation of plaque morphology, and strain analysis.

In this work, local image contrast in carotid artery imaging has been compared between harmonic imaging and dual frequency band imaging as a measure how capable the methods are to suppress reverberation clutter. The results from a study based on data from 22 patients suggest that both methods reduce the impact of reverberation clutter with DBI yielding 10 to 11.5 dB more image contrast than HI.

The impact of spatial compounding on the performance of HI regarding local image contrast was minor and statistically insignificant. However HIC yields better border delineation, less speckle and more appealing images.

Relating the results of this work to the clinical impact of HI, this may implicate that DBI will improve the clinical value of ultrasound in various applications, which has to be adressed in further research.

## Bibliography

[1] WHO, "Fact sheet 310, the top ten causes of death 2008," May 2011.

[2] T. Thom, N. Haase, W. Rosamond, V. J. Howard, J. Rumsfeld, T. Manolio, Z. Zheng, K. Flegal, C. O'Donnell, S. Kittner, D. Lloyd-Jones, J. Goff, David C, Y. Hong, R. Adams, G. Friday, K. Furie, P. Gorelick, B. Kissela, J. Marler, J. Meigs, V. Roger, S. Sidney, P. Sorlie, J. Steinberger, S. Wasserthiel-Smoller, M. Wilson, and P. Wolf, "Heart disease and stroke statistics–2006 update: a report from the american heart association statistics committee and stroke statis-

tics subcommittee," *Circulation*, vol. 113, no. 6, pp. e85–151, Feb. 2006, PMID: 16407573.

[3] M. L. Dyken, "Stroke risk factors," in *Prevention of stroke*, J. W. Norris and V. Hachinski, Eds. Springer-Verlag, 1991, pp. 83–102.

[4] M. J. Davies and N. Woolf, "Atherosclerosis: what is it and why does it occur?" *British Heart Journal*, vol. 69, no. 1 Suppl, pp. S3–S11, Jan. 1993, PMID: 8427761 PMCID: 1025252.

[5] E. Falk, "Why do plaques rupture?" *Circulation*, vol. 86, no. 6 Suppl, pp. III30–42, Dec. 1992, PMID: 1424049.

[6] E. Falk, P. K. Shah, and V. Fuster, "Coronary plaque disruption," *Circulation*, vol. 92, no. 3, pp. 657 –671, 1995.

[7] R. Eisenberg, W. Nemzek, W. Moore, and R. Mani, "Relationship of transient ischemic attacks and angiographically demonstrable lesions of carotid artery," *Stroke*, vol. 8, no. 4, pp. 483 –486, Jul. 1977.

[8] M. Græbe and H. Sillesen, "The significance of echolucent plaques: Past and future perspectives," in *Ultrasound and Carotid Bifurcation Atherosclerosis*, A. Nicolaides, K. W. Beach, E. Kyriacou, and C. S. Pattichis, Eds. Springer London, 2012, pp. 543–549.

[9] S. P. Näsholm, R. Hansen, S. Måsøy, T. Johansen, and B. A. Angelsen, "Transmit beams adapted to reverberation noise suppression using dual-frequency SURF imaging," *IEEE Trans Ultrason Ferroelectr Freq Control*, vol. 56, no. 10, pp. 2124–2133, Oct. 2009.

[10] R. Hansen, S. Måsøy, T. F. Johansen, and B. A. Angelsen, "Utilizing dual frequency band transmit pulse complexes in medical ultrasound imaging," *J Acoust Soc Am*, vol. 127, no. 1, p. 579, 2010.

[11] S. P. Näsholm, R. Hansen, and B. A. Angelsen, "Post-processing enhancement of reverberation-noise suppression in dual-frequency SURF imaging," *IEEE Trans Ultrason Ferroelectr Freq Control*, vol. 58, no. 2, pp. 338–348, Feb. 2011.

[12] R. H. Behler, M. R. Scola, and C. M. Gallippi, "Reverberation artifact rejection and masking in arterial ARFI imaging," in *Proc IEEE Ultrason Symp*. IEEE, Sep. 2009, pp. 2367–2370.

[13] M. A. Lediju, G. E. Trahey, B. C. Byram, and J. J. Dahl, "Short-lag spatial coherence of backscattered echoes: imaging characteristics," *IEEE Trans Ultrason Ferroelectr Freq Control*, vol. 58, no. 7, pp. 1377–1388, Jul. 2011.

[14] J. D. Thomas and D. N. Rubin, "Tissue harmonic imaging: Why does it work?" *J Am Soc Echocardiogr*, vol. 11, no. 8, pp. 803–808, Aug. 1998.

[15] S. P. Turner and M. J. Monaghan, "Tissue harmonic imaging for standard left ventricular measurements: Fundamentally flawed?" *Eur J Echocardiogr*, vol. 7, no. 1, pp. 9 –15, Jan. 2006.

[16] T. S. Desser, R. B. Jeffrey Jr., M. J. Lane, and P. W. Ralls, "Tissue harmonic imaging: Utility in abdominal and pelvic sonography," *J Clin Ultrasound*, vol. 27, no. 3, pp. 135–142, Mar. 1999.

[17] F. Tranquart, N. Grenier, V. Eder, and L. Pourcelot, "Clinical use of ultrasound tissue harmonic imaging," *Ultrasound Med Biol*, vol. 25, no. 6, pp. 889–894, Jul. 1999.

[18] S. J. Rosenthal, P. H. Jones, and L. H. Wetzel, "Phase inversion tissue harmonic sonographic imaging," *AJR Am J Roentgenol*, vol. 176, no. 6, pp. 1393 –1398, Jun. 2001.

[19] U. Bartram and K. Darge, "Harmonic versus conventional ultrasound imaging of the urinary tract in children," *Pediatr Radiol*, vol. 35, no. 7, pp. 655–660, Mar. 2005.

[20] D. Paladini, M. Vassallo, A. Tartaglione, C. Lapadula, and P. Martinelli, "The role of tissue harmonic imaging in fetal echocardiography," *Ultrasound Obstet Gynecol*, vol. 23, no. 2, pp. 159–164, Feb. 2004.

[21] C. Yen, H. Chang, S. Huang, Y. Huang, and C. Jeng, "Combination of tissue harmonic sonography, real-time spatial compound sonography and adaptive image processing technique for the detection of carotid plaques and intima-medial thickness," *Eur J Radiol*, vol. 71, no. 1, pp. 11–16, Jul. 2009.

[22] R. Hansen, S. Måsøy, T. A. Tangen, and B. A. Angelsen, "Nonlinear propagation delay and pulse distortion resulting from dual frequency band transmit pulse complexes," *J Acoust Soc Am*, vol. 129, no. 2, p. 1117, 2011.

[23] S. Måsøy, Ø. Standal, J. M. Deibele, S. P. Näsholm, B. Angelsen, T. F. Johansen, T. A. Tangen, and R. Hansen, "Nonlinear propagation acoustics of dual-frequency wide-band excitation pulses in a focused ultrasound system," *J Acoust Soc Am*, vol. 128, no. 5, p. 2695, 2010.

[24] R. Hansen and B. A. Angelsen, "SURF imaging for contrast agent detection," *IEEE Trans Ultrason Ferroelectr Freq Control*, vol. 56, no. 2, pp. 280–290, Feb. 2009.

[25] E. Chérin, J. Brown, S. Måsøy, H. Shariff, R. Karshafian, R. Williams, P. N. Burns, and F. S. Foster, "Radial modulation imaging of microbubble contrast agents at high frequency," *Ultrasound Med Biol*, vol. 34, no. 6, pp. 949–962, Jun. 2008.

[26] S. E. Måsøy, Ø. Standal, P. Näsholm, T. F. Johansen, B. Angelsen, and R. Hansen, "SURF imaging: In vivo demonstration of an ultrasound contrast agent detection technique," *IEEE Trans Ultrason Ferroelectr Freq Control*, vol. 55, no. 5, pp. 1112–1121, May 2008.

[27] R. Kern, K. Szabo, M. Hennerici, and S. Meairs, "Characterization of carotid artery plaques using real-time compound b-mode ultrasound," *Stroke*, vol. 35, no. 4, pp. 870 –875, Apr. 2004.